

Rochester Institute of Technology

RIT Digital Institutional Repository

Theses

8-3-2017

Enhanced Light Absorption and Electro-absorption Modulation Based on Graphene and Conductive Oxide

Kaifeng Shi
kxs9364@rit.edu

Follow this and additional works at: <https://repository.rit.edu/theses>

Recommended Citation

Shi, Kaifeng, "Enhanced Light Absorption and Electro-absorption Modulation Based on Graphene and Conductive Oxide" (2017). Thesis. Rochester Institute of Technology. Accessed from

This Dissertation is brought to you for free and open access by the RIT Libraries. For more information, please contact repository@rit.edu.

R.I.T

ENHANCED LIGHT ABSORPTION AND ELECTRO- ABSORPTION MODULATION BASED ON GRAPHENE AND CONDUCTIVE OXIDE

by

KAIFENG SHI

A dissertation submitted in partial fulfillment of the requirements
for the degree of Doctor of Philosophy in Microsystems Engineering

Microsystems Engineering
Kate Gleason College of Engineering

Rochester Institute of Technology
Rochester, New York
August 3, 2017

Enhanced Light Absorption and Electro-Absorption Modulation Based on Graphene and Conductive Oxide

By

Kaifeng Shi

Committee Approval:

We, the undersigned committee members, certify that we have advised and/or supervised the candidate on the work described in this dissertation. We further certify that we have reviewed the dissertation manuscript and approve it in partial fulfillment of the requirements of the degree of Doctor of Philosophy in Microsystems Engineering.

Dr. Stefan F. Preble Date
Associate Professor, Microsystems Engineering (Advisor)

Dr. Bruce W. Smith Date
Professor, Microsystems Engineering

Dr. Karl D. Hirschman Date
Professor, Electrical and Microelectronic Engineering

Dr. Jing Zhang Date
Assistant Professor, Electrical and Microelectronic Engineering

Dr. Parsian K. Mohseni Date
Assistant Professor, Microsystems Engineering

Certified by:

Dr. Bruce W. Smith Date
Director, Microsystems Engineering Program

ABSTRACT

Kate Gleason College of Engineering
Rochester Institute of Technology

Degree: Doctor of Philosophy **Program:** Microsystems Engineering

Name of Candidate: Kaifeng Shi

Name of Advisor: Stefan F. Preble

Title: Enhanced Light Absorption and Electro-Absorption Modulation Based on Graphene and Conductive Oxide

The development of integrated photonics is limited by bulky and inefficient photonic component compared to their electronic counterparts due to weak light-matter interactions. As the key devices that determine the performance of integrated photonic circuits, electro-optical (EO) modulators are inherently built on the basis of enhancing light-matter interactions. Current EO modulators often deploy conventional materials with poor EO properties, or ring resonator structure with narrow bandwidth and thermal instability, so their dimensions and performance have nearly reached their physical limits. Future integrated photonic interconnects require EO modulators to be ultra-compact, ultra-fast, cost-effective and able to work over a broad bandwidth. The key to achieving this goal is to identify an efficient and low-cost active material. Meanwhile, novel waveguides and platforms need to be explored to significantly enhance light-active medium interaction. As widely investigated novel materials, graphene and conductive oxide (COx) have shown remarkable EO properties. The objective of this dissertation is to realize enhanced light-matter interaction based on these two novel materials and waveguiding platforms, and further develop ultra-compact, ultra-fast EO modulators for future photonic integrated circuits. The first part of this dissertation covers the theory of EO modulation mechanisms, several types of EO materials including graphene and COx, as well as fabrication techniques. The second part demonstrates greatly enhanced light absorption based on mono-/multi-layer graphene. The third part proposes the theoretical study of nanoscale EA modulators based on ENZ-slot waveguide. The fourth part explores the field effect within a MOS-like structure, and verifies the ENZ behavior of COx. The fifth part experimentally demonstrates both plasmonic and dielectric configurations for ultra-compact and ultra-fast EA modulators. The final part summarizes the work presented in this dissertation and also discusses some future work for photonic applications.

ACKNOWLEDGMENTS

I felt so fortunate to be surrounded by many loving people and now it is my pleasure to thank all of them for their love, encouragement, support, and blessings.

I would like to express my sincerest gratitude to my advisor Professor Stefan F. Preble, for his valuable guidance and generous support throughout my entire graduate studies at RIT. His pioneering vision in the field of photonics, abundance of knowledge and hard-working spirit inspired and motivated me. Without his insightful suggestions and persistent help, this dissertation could not be completed.

I would like to express my deepest appreciation to Professor Bruce W. Smith, Professor Karl D. Hirschman, Professor Jing Zhang, Professor Parsian K. Mohseni and Professor Jayanti Venkataraman for serving as my dissertation committee, and for their generosity in sharing their invaluable opinions and all sorts of resources for the maximum good of my research.

The staff members in the Semiconductor & Microsystems Fabrication Laboratory (SMFL) and Cornell Nanoscale Science & Technology Facility (CNF) deserve my sincere thanks as well. In particular, I would like to thank Mr. Sean O'Brien, Ms. Patricia Meller, Mr. Aaron Windsor and Mr. Garry Bordonaro for their knowledge, willingness, and readiness to help me with device fabrication.

I want to express my gratitude to my former colleagues, Dr. Ruoxi Yang, Dr. Wangshi Zhao, Dr. Liang Cao, and all the current colleagues in integrated photonics group, especially Mr. Peichuan Yin and Mr. Zihao Wang, for their help with my research, and for offering me useful discussions.

Special thanks should be sent to my former advisor, late Professor Zhaolin Lu. He led me into the exciting field of nanoplasmonics and nanophotonics. His expertise in optical science greatly broadened my vision, and helped to establish my interest of study. None of this work would have been possible without his advice.

Finally, I would like to thank my family. Words cannot express how grateful I am to my mother-in-law, father-in-law, my mother, and father for all the sacrifices that they have made on my behalf. Their endless support was what sustained me thus far. I would also like to express my appreciation to my dearest wife, Ting, for her unlimited love, support, and understanding. She gave me encouragement whenever I needed and offered invaluable accompany all the time.

Table of Contents

1. Introduction	1
1.1 Motivation	1
1.2 Physical effects for electro-optical modulation	3
1.2.1 Pockels effect and Kerr effect	3
1.2.2 Franz-Keldysh effect	5
1.2.3 Quantum-confined Stark effect	6
1.2.4 Plasma dispersion effect	7
1.3 Materials for EO modulation	10
1.3.1 Dielectric crystals	10
1.3.2 Group IV materials	11
1.3.3 III-V semiconductors	12
1.3.4 Non-linear polymers	12
1.3.5 Graphene	13
1.3.6 Conductive oxide (CO _x)	15
1.3.7 Thin film materials	18
1.4 Fabrication techniques for graphene and conductive oxide	19
1.4.1 Graphene synthesis, transfer and characterization	19

1.4.2	Fabrication of conductive oxide.....	24
1.5	Numerical analysis methods.....	27
1.5.1	Transfer matrix method (TMM)	27
1.5.2	Finite-difference time-domain (FDTD) method	29
1.6	Dissertation overview.....	31
2.	Enhanced light absorption by graphene	34
2.1	Introduction	34
2.2	Enhanced polarized light absorption by monolayer graphene	35
2.2.1	Background.....	35
2.2.2	Numerical analysis	36
2.2.3	Experimental validation and discussion	38
2.2.4	Potential application in electro-optical modulation.....	43
2.3	Enhanced unpolarized light absorption by multilayer graphene	46
2.3.1	Background.....	46
2.3.2	Numerical analysis	46
2.3.3	Quantitative explanation.....	51
2.3.4	Potential application in photovoltaics.....	52
2.4	Conclusions	54

3.	ENZ-slot Waveguide Based on Conductive Oxide	55
3.1	Background	55
3.2	ENZ material and slot waveguide	58
3.3	Nanoscale EA modulators based on COx-slot waveguide	60
3.4	Laser beam steering by COx-slot waveguide	63
3.5	Conclusions	66
4.	Field-effect EA Modulators Based on Conductive Oxide.....	68
4.1	Background	68
4.2	Structure and fabrication	70
4.3	Broadband bias-polarity-dependent modulation effect	72
4.4	ENZ effect of conductive oxide	76
4.5	Working bandwidth and modulation speed.....	85
4.6	Conclusions	87
5.	Ultra-compact Field-effect EA Plasmonic Modulator	89
5.1	Background and principle.....	89
5.2	Schematic and fabrication	93
5.3	Experimental validation of modulation effect.....	95
5.4	Modulation depth and modulation speed	97

5.5	Conclusions	98
6.	Nanoscale Field-effect Optical Modulators Based on Depletion of ENZ films.....	100
6.1	Background	100
6.2	Design and simulation	102
6.3	Performance analysis.....	105
6.4	Discussion and conclusion	109
7.	Ultra-compact High Speed Field-Effect Dielectric Modulator	111
7.1	Background	111
7.2	Design, modeling, and fabrication.....	112
7.3	Light coupling and modulation measurement	116
7.4	Circuit analysis	119
7.5	Conclusions	120
8.	Conclusions	122
8.1	Enhanced light absorption by graphene	122
8.2	Field-effect optical modulation by conductive oxide.....	123
8.3	Ultra-compact and ultra-fast field effect EA modulators	124
8.4	Future work	124
9.	References	127

Table of Figures

Figure 1-1. Dependence of refractive index on the electric field: (a) Pockels effect; (b) Kerr effect.	4
Figure 1-2. The Franz-Keldysh effect. (a) The bandgap for bulk semiconductor without (OFF) and with (ON) external electric field. (b) Absorption spectrum change by external electric field. The absorption peak moves towards longer wavelengths. (c) Electro-absorption modulator in a waveguide configuration [38].	5
Figure 1-3. (a) The band diagrams of a quantum well without (OFF) and with (ON) external electric field. (b) Change in the absorption spectrum in an AlGaAs/GaAs multi-quantum-well structure with increasing applied voltage [38].	6
Figure 1-4. (a) Real and (b) imaginary parts of dielectric constant of highly doped conductive oxides. Shaded areas correspond to wavelengths where CO _x exhibit metallic properties [58].	16
Figure 1-5. Multiple CVD graphene sheets with diagonal of up to 30 inches transferred to transparent flexible substrates [67].	21
Figure 1-6. Process of graphene transfer. The picture of multilayer graphene on Ni transferred to glass substrate is shown at the end.	22

Figure 1-7. (a) Layer dependence of graphene Raman spectrum. Raman spectra of N=1-4 layers of graphene on Si/SiO₂ and of bulk graphite [112]. (b) Optical microscope image of multilayer graphene sheet on Si/SiO₂[115]..... 24

Figure 1-8. Dependence of (a) real and (b) imaginary parts of AZO permittivity on oxygen pressures upon deposition [116]. Dependence of (c) cross-over wavelength and (d) Drude-damping coefficient of AZO, ITO and GZO on different dopant concentrations [117]... 25

Figure 1-9. (a) Illustration of the transfer matrix of a medium. (b) Transfer matrices of each element in a multilayered system..... 27

Figure 1-10. The distribution of E-field and H-field components in Yee cell..... 29

Figure 2-1. (a)Illustration of the graphene-sandwiched structure. (b) Numerical calculation of the reflectance and absorption as functions of incident angle, θ_1 , and substrate refractive index n_3 37

Figure 2-2. (a)Illustration of the experimental setup for ATR measurement. The red dashed line represents the monolayer graphene film. P1 and BS represent the polarizer and beam splitter, respectively. (b) Actual picture of the ATR test setup. 39

Figure 2-3. Measured reflectance of the monolayer graphene with M1.50 as substrate under TE-polarized light incidence at (a) $\lambda=650\text{nm}$ and (b) $\lambda=1520\text{nm}$. In both graphs, red curves represent the results when a BK7 deflector is used; blue curves represent the results when a BSG deflector is used. In the legend, “G” and “M” represent “graphene” and “matching

liquid”, respectively. “BK7/G/M/BK7” means the result for the BK7(prism)-graphene-M1.50(substrate)-BK7(deflector) configuration.....	40
Figure 2-4. For 1520nm TM-polarized light incidence, the measured reflectance by the monolayer graphene sample as a function of incident angle when (a) the substrate is air, and (b) the substrate is M1.50.....	42
Figure 2-5. Reflectance as a function of angle for the Au/electrolyte gel/graphene on glass slide modulator with different applied voltages for (a) TE-polarized incident light; (b) TM-polarized incident light. Inset: illustration of the modulator.....	44
Figure 2-6. (a-d) Analytical and numerical results of absorption of TE- and TM-polarized light as a function of incident angle at $\lambda_0=1000\text{nm}$ and $\lambda_0=2000\text{nm}$	48
Figure 2-7. (a) Maximum light absorption as a function of wavelength for TM and TE polarization for different number of graphene layers. (b) Light absorption as a function of wavelength for TM and TE polarization at different incident angles.	49
Figure 2-8. (a-d) Power distribution of the simulated structure at the incident angle where maximum absorption is achieved. MLG is located between -10.05nm and 0 on y-axis.	50
Figure 3-1. (a) Structure of a simple three-layer waveguide. (Value of n_{silicon} used for $\lambda_0 = 1550 \text{ nm}$ is 3.47). (b) Plots of electric field, magnetic field, power percentage in the slot and effective index of the structure versus slot dielectric constant [183].	59

Figure 3-2. (a) Real part of the dielectric constant of ITO as a function of wavelength at three different carrier concentration based on the Drude model [186]. (b) Illustration of the ENZ-slot waveguide [187].	60
Figure 3-3. The electric field profiles, effective indices and propagation loss for different ITO-slot waveguide at untuned state and ENZ state, respectively: (a) in a dielectric rib waveguide; (b) in a plasmonic waveguide [183].	62
Figure 3-4. (a) Illustration of beam steering based on ENZ-slot waveguide with periodic gratings. (b) Complex effective index in terms of carrier concentration.	63
Figure 3-5. Phase, normalized magnitude and far-field intensity of E_y for steering angles of (a) 14° and (b) 60° [183].	65
Figure 4-1. Operation of field effect in MOS capacitor. (a) Flat band. (b) Accumulation. (c) Depletion. (d) Inversion.	69
Figure 4-2. (a) Schematic of the MIC EO modulator. (b) Illustration of the setup for ATR measurement. (c) Picture of the fabricated device.	71
Figure 4-3. Reflectance as a function of incident angle for the modulator under different applied voltages for different wavelengths.	73
Figure 4-4. Power reflectance as a function of applied voltage at the modulation angle for $\lambda_0=1550\text{nm}$.	74

Figure 4-5. Power reflectance as a function of time at the modulation angle for $\lambda_0=1550\text{nm}$. (a) Fast modulation; (b) Slow modulation. Inset: reflectance change within 60s. 75

Figure 4-6. (a) Illustration of the ITO/HfO₂/Al structure and experimental setup. The dimensions are not in scale. Quartz substrate is about 0.5mm thick and the diameter of the hemicylindrical prism is about 100mm. Insets: 3D schematic of the device (upper left) and picture of the fabricated device (upper right). (b) At incident angle $\theta = 70^\circ$, the reflected power as a function of working wavelength at original state (no bias) for the ITO/HfO₂/Al sample. (c) At incident angle $\theta = 70^\circ$, the R- λ measurement for a 10-nm ITO film on quartz. (d) The R- θ measurement for a 10-nm ITO film on quartz for TM polarized light at $\lambda=1280\text{ nm}$ and the fitting curve. 76

Figure 4-7. (a) The MIC structure under no bias (original). (b) The MIC structure under negative bias (depletion). (c) The MIC structure under positive bias (accumulation). 78

Figure 4-8. (a) The R- θ measurement under DC biases at $\lambda=1280\text{nm}$ with increased time (b) Output waveforms of the reflected light power for different wavelengths when the modulator is under $V_{pp}=12\text{V}$, 500 Hz sine electric signal. (c) The reflected power as a function of incident light wavelength for A, O and D states. The inset shows the minimum value of the three curves, which correspond to ENZ. 80

Figure 4-9. (a) Drude model calculation for ϵ_{ITO} as a function of wavelength. (b) Reflectance calculation of the MIC structure by sweeping incident angle and wavelength. 83

Figure 4-10. $M-\lambda$ relations for O-A, A-D, and O-D modulations under 500Hz, $V_{pp}=12V$ AC signal. 84

Figure 4-11. (a) The output waveform for modulating frequency $f=1MHz$. (b) Modulation depth as a function of modulating frequency. (c) The circuit diagram for the MIC structure. (d) For a given V , the normalized applied voltage on the device as a function of modulating frequency..... 86

Figure 5-1. Illustration of the working modes of the metal-insulator-COx-insulator-metal structure: (a) Without bias. (b) Depletion mode, where the ITO is less absorptive and the waveguide has lower attenuation. (c) Accumulation mode, where the ITO is more absorptive and the waveguide has higher attenuation. (d) The mode profile for the no bias case. (e) The mode profile for the depletion case. (f) The mode profile for the accumulation case..... 92

Figure 5-2. (a) Schematic of the fabricated EO modulator and the test setup. (b) Back view of the modulators and their GSG contact electrodes. (c) Top view of the output port. (d) Back side SEM picture of the device input and output ports. (e) Bottom view of the edge of the device. 94

Figure 5-3. (a) Picture of the experimental setup. Inset: picture of the tested device. (b) Image of the output ports by the NIR camera. Inset: the output ports. (c) Image of the output of the device through the NIR camera when NIR light is fed in from the input port. 96

Figure 5-4. Oscilloscope measurement of the output light power under an applied electric signal of (a) 1 MHz, (b) 10 MHz, (c) 100 MHz, and (d) 500 MHz. (a&b) are obtained using a DC-coupled photodetector. (c&d) are obtained using an AC-coupled photodetector. 97

Figure 5-5. The potential applications of the MICIM modulator in 3D interconnection and in integrated photonic/plasmonic circuits. (a) The potential application of the modulator in 3D interconnection, where both sides of the modulators are passivated and Chip 1 and Chip 2 may be standard CMOS circuits. (b, c) The potential application of the MICIM modulator in integrated photonic/plasmonic circuits, where (b) illustrates the front view, and (c), 3D view. Photonic/plasmonic power flow is between the two metal layers in the red arrow direction. 99

Figure 6-1. FEM simulation of the double capacitor gating scheme on carrier distribution for (a) accumulation and (b) depletion..... 101

Figure 6-2. (a) Illustration of the metal-insulator-COx-insulator-metal structure working at the depletion mode. (b-d) FEM simulation of the residual electron distribution in the ITO film. (e) The real part of the ITO complex dielectric constant (ϵ') of ITO. (f) The imaginary part of the complex dielectric constant (ϵ'') of ITO..... 103

Figure 6-3. (a) Illustration of the Si-insulator-COx-insulator-Si structure working at the depletion mode. (b, c) FEM simulation of the residual electron distribution in the ITO film and accumulated electron distribution in Si. (d) The residual electron distribution in the ITO film. (e, f) The complex optical dielectric constant of ITO. (g) The accumulation

electron distribution in the Si. (h, i) The complex refractive index of Si in the accumulation layer..... 104

Figure 6-4. The electric field profiles ($|E(x,y)|$), effective indices, and propagation loss for different ITO-sandwiched waveguides in two cases: no bias and depletion. (a-c) In a plasmonic waveguide. (d-f) In a Si waveguide. The maximum field magnitude is normalized to be 1 in each plot. The refractive indices of Si, HfO₂, SiO₂, and Au are assumed to be 3.476, 2.070, 1.444, and 0.559+j9.81, respectively. The thickness of each HfO₂ layer is 10 nm, ITO thickness, 4 nm..... 106

Figure 6-5. (a) The illustration of an EA modulator embedded in a Au-HfO₂-Au plasmonic waveguide. The cross section dimensions of the modulator are shown in Fig. 3(a). (b, c) The 3D simulation of light propagation between the plasmonic waveguide and the EA modulator in ENZ and depletion cases, respectively. (d) The illustration of an EA modulator embedded on a rib Si waveguide. The cross section dimensions of the modulator are shown as Fig. 3(d). (e, f) The 3D simulation of light propagation between the rib Si waveguide and the EA modulator in ENZ and depletion cases, respectively. 108

Figure 7-1. (a) The schematic of a high-confinement Si slot-waveguide modulator [199]. (b) An ITO-based nanophotonic modulator [83]...... 112

Figure 7-2. (a) The multi-layer stack of the dielectric modulator. (b) The 3D schematic of the modulator. 113

Figure 7-3. (a) The simulated device schematic in Lumerical FDTD solutions. (b) The output transmission of the modulator at original state and ENZ state. (c). Fabrication flow and SEM images of the device..... 115

Figure 7-4. (a) Light coupling and modulation measurement setup. 116

Figure 7-5. (a) Output transmission of simulated device with updated parameters and measured output transmission without external electric signal. (b) The output light power waveform of the modulator under a 500 Hz, 11V- V_{pp} electric signal. 117

Figure 7-6. (a) Modulation depth versus frequency measured by spectrum analyzer. (b) Spectrum analyzer measurement showing intensity modulation at 2 GHz. 118

Figure 7-7. S_{11} measurement and curve fitting of (a) a simple RLC equivalent circuit model of the modulator and (b) a more complicated model. 120

Table of Acronyms

ALD	Atomic Layer Deposition
ATR.....	Attenuated Total Reflection
AZO	Aluminum-doped Zinc Oxide
CMOS	Complementary Metal-Oxide Semiconductor
COx.....	Conductive Oxide
CVD	Chemical Vapor Deposition
DI	Deionized
EA	Electro-Absorption
EDFA	Erbium-doped Fiber Amplifier
EM.....	Electromagnetic
ENZ.....	Epsilon-Near-Zero
EO	Electro-Optical
FDTD	Finite-Difference Time-Domain
GHz.....	Gigahertz
GZO	Gallium-doped Zinc Oxide
IPA	Isopropyl Alcohol
ITO	Indium Tin Oxide
kHz.....	kilohertz
LSPR.....	Localized Surface Plasmon Resonance
MHz	Megahertz
MIC.....	Metal-Insulator-COx

MICIMMetal-Insulator-COx-Insulator-Metal
MIMMetal-Insulator-Metal
MLG.....Multi-layer Graphene
MOSMetal-Oxide Semiconductor
NIR.....Near-infrared
PLDPulse Laser Deposition
PMMAPolymethyl-methacrylate
PVPhotovoltaic
SEMScanning Electron Microscopy
SOISilicon-On-Insulator
SPSurface Plasmon
SPPSurface Plasmon Polariton
TE.....Transverse Electric
TFTThin-Film Transistor
THzTerahertz
TIRTotal Internal Reflection
TM.....Transverse Magnetic
UHVUltra-High Vacuum

1. INTRODUCTION

1.1 Motivation

With the fast development of nanophotonics and nanoplasmonics, many key components in optoelectronic integrated circuits have been successfully made into nanoscale, including lasers, detectors, and waveguides [1-3]. Electro-optic (EO) modulators upconvert electronic signals into high bit-rate photonic data [4,5], thus serving as one of the most important devices for photonic integration. Despite some breakthroughs in the development of EO modulators in recent years [6-10], the bottleneck of lacking ultra-compact and high-speed EO modulators has not been well solved, which greatly impedes the wide deployment of the on-chip optical interconnects. Because of the poor EO properties of regular materials [11], a conventional EO modulator has a very large footprint [6,8,10,12]. Silicon modulators based on high-Q resonators enhance the EO effect due to a large quality factor of resonant cavities, thus can shrink their dimensions to tens of micrometers [7]. However, resonator modulators usually suffer from bandwidth limitation, temperature fluctuation as well as fabrication tolerance [13,14]. EO modulators based on hybrid novel semiconductors could exhibit properties of high speed, low energy consumption as well as easy integration [15–19], but their sizes are still bulky compared with on-chip electronic components. With a large modulation depth in the NIR regime, PlasMOSStors promise to be very compact [20], but they are inherently limited by large insertion loss and low operation speed. The technical barrier may not be well overcome based on conventional approaches and well-known materials.

Recent research on graphene has provided unprecedented opportunities to meet the challenges. Graphene [21,22] has attracted a great deal of interest because of its exceptional electrical and optical properties [23-26]. In particular, monolayer graphene is visible under an optical microscope due to its strong coupling with light, and it absorbs a constant amount of light over a broad spectrum range [27]. Besides, graphene has a gate-variable optical conductivity [28] and supports high-speed operation [29]. Thus, it is very promising to utilize graphene for future optoelectronic devices, including EO modulators [30]. Liu *et al* demonstrated a broadband EO modulator at telecom wavelengths based on the interband absorption of graphene with overall length only 40 μm [31]. A recently reported graphene modulator by leveraging critical coupling effects on a silicon nitride ring resonator achieves working bandwidth of 30GHz [32]. The key to achieving nanoscale graphene EO modulation is to greatly enhance light-graphene interaction based on novel waveguides and platforms. In this dissertation, I will first focus on enhanced light absorption by graphene fulfilled through a novel graphene-sandwiched structure, and reveal the potential of graphene in EO modulation. The possibility of utilizing the enhanced light absorption by graphene for photovoltaic applications will also be discussed.

Aside from graphene, another promising active material for EO modulation, CO_x, will be investigated in detail. Most of the previous effort was focused on the exploration of the EO properties of dielectrics or polymers owing to their low optical absorption for waveguide applications; the optical properties of absorptive materials, for example CO_x, have been relatively overlooked. Recent work shows that the optical dielectric constant of CO_x in the charged layer of a metal-insulator-CO_x (MIC) structure can be tuned in a large

range by electrical gating [33]. When a large electric field is applied across the insulator layer of an MIC structure, significant surface charge can be induced and the induced charge can greatly alter the optical properties of the active layer at the insulator-COx interface. Besides, COx has other impressive advantages such as low losses, easy integration and compatibility with standard CMOS fabrication [34-36]. Therefore, COx can be good alternative materials for EO modulation.

The final goal of the investigations is to realize high-speed EO modulation at nanoscale.

1.2 Physical effects for electro-optical modulation

The modulation of an optical signal can be categorized in different ways. According to the fundamental beam parameters, the modulation can be imposed on either the amplitude, phase, frequency or polarization of the beam. According to the mechanism, the modulation can be classified as either electro-refractive or electro-absorptive. When a material is exposed to an applied electric field, a change in its real and imaginary refractive indices may occur, corresponding to either electro-refraction (change in real refractive index Δn) or electro-absorption (change in absorption coefficient $\Delta\alpha$). Here, we will focus on the different physical effects that lead to electro-refraction or electro-absorption.

1.2.1 Pockels effect and Kerr effect

The primary physical effect for causing electro-refraction is called electro-optic effect [37, 38]. The field dependence of the refractive index can be described by the sum of linear terms and higher order terms,

$$n(E) = n - \frac{1}{2}rn^3E - \frac{1}{2}\xi n^3E^2 \dots, \quad (1.1)$$

where n is the refractive index, r and ξ are electro-optic coefficients. The higher-order terms in this series are considerably smaller than n so that terms higher than the third can be neglected.

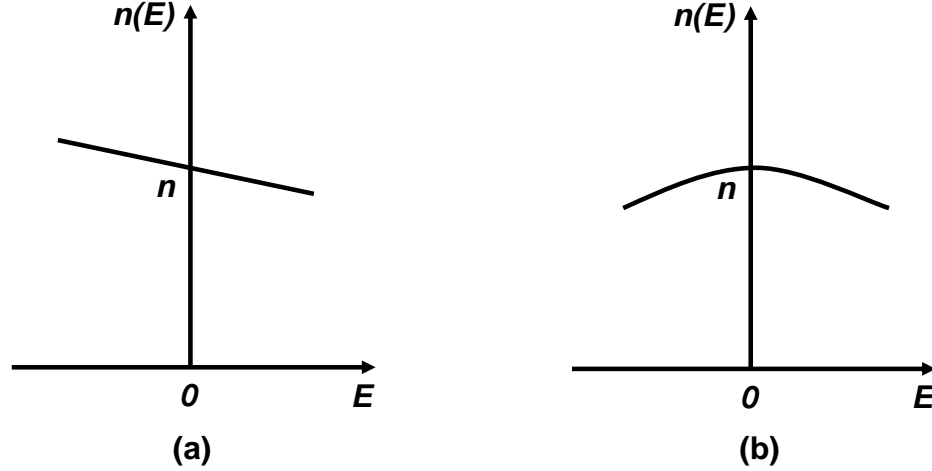


Figure 1-1. Dependence of refractive index on the electric field: (a) Pockels effect; (b) Kerr effect.

In many materials, the third term in Eq. (1.1) is still far too small, which can be taken out of consideration. Then what is left over, $n(E) = n - \frac{1}{2}rn^3E$, is called Pockels effect. The linear electro-optic coefficient, r , is known as the Pockels coefficient. For common crystals used as Pockels medium, the values of r are in the range from 10^{-12} to 10^{-10} m/V. On the other hand, another effect dominates in centrosymmetric materials since $n(E)$ must be an even symmetric function. As a result, with the Pockels coefficient $r = 0$, $n(E) = n - \frac{1}{2}\xi n^3E^2$. This effect is called Kerr effect, and the quadratic electro-optic coefficient, ξ , is known as the Kerr coefficient, which has typical values from 10^{-18} to 10^{-14} m²/V² in crystals

and 10^{-22} to 10^{-19} m^2/V^2 in liquids [38]. Figure 1-1 plots the refractive index as a function of electric field for Pockels effect and Kerr effect, respectively. Since there is no carrier transport involved in the medium, modulators based on these two effects usually have relatively low power consumption and high working speed.

1.2.2 Franz-Keldysh effect

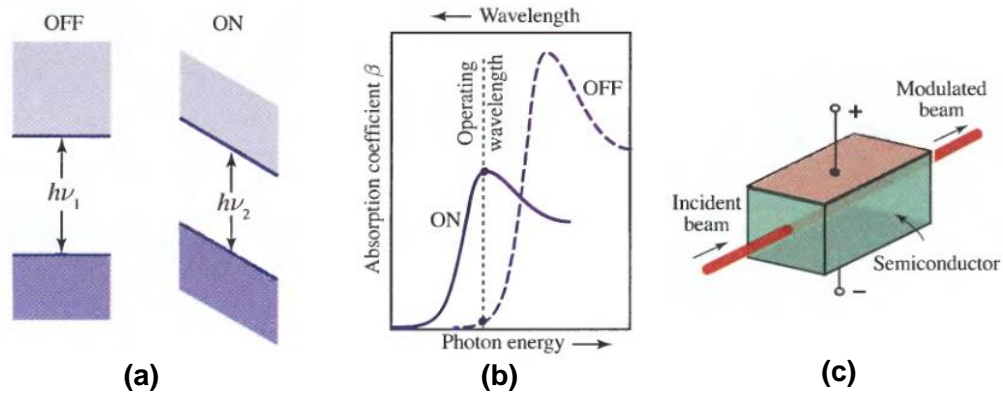


Figure 1-2. The Franz-Keldysh effect. (a) The bandgap for bulk semiconductor without (OFF) and with (ON) external electric field. (b) Absorption spectrum change by external electric field. The absorption peak moves towards longer wavelengths. (c) Electro-absorption modulator in a waveguide configuration [38].

The Franz-Keldysh effect demonstrates a change of absorption characteristics in a bulk semiconductor under an externally applied electric field. The effect is caused by tilting of the energy bands of a semiconductor. As shown in Fig.1-2(a), at equilibrium (OFF) state, an electron needs to absorb a photon with energy $h\nu_1$ in order to transit from the valence band to the conduction band. However, an external field will result in electron tunneling and the absorption edge may extend to the band gap between valance and conductance bands. Therefore, an electronic transition can happen with a lower energy $h\nu_2$ when the applied electric field is on. As shown in Fig.1-2(b), the absorption peak shifts to longer

wavelength due to the Franz-Keldysh effect. This effect can be used to realize electro-absorption. Without applied electric field (OFF), an incident light beam with photon energy smaller than $h\nu_1$ could transmit through without being absorbed. However, when the electric field is applied (ON), light with energy larger than $h\nu_2$ will be absorbed. As shown in Fig. 1-2(c), electro-absorption based on this effect is usually realized within a waveguide, where the externally applied electric field is perpendicular to the direction of light propagation. The operation is typically faster than electro-refraction and requires lower voltages.

1.2.3 Quantum-confined Stark effect

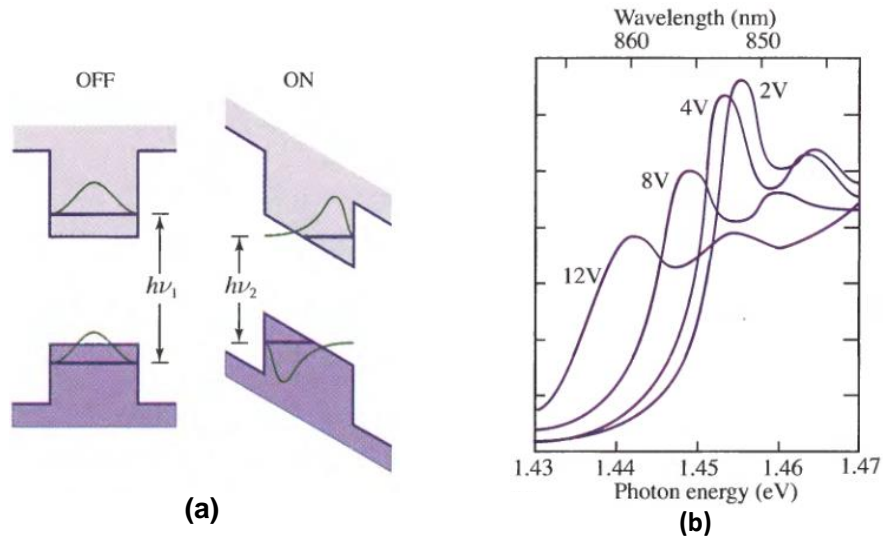


Figure 1-3. (a) The band diagrams of a quantum well without (OFF) and with (ON) external electric field. (b) Change in the absorption spectrum in an AlGaAs/GaAs multiquantum-well structure with increasing applied voltage [38].

Different from the Franz-Keldysh effect, the quantum-confined Stark effect describes a change of absorption spectrum of a quantum well due to an external electric field. As seen in Fig. 1-3(a), when the electric field is applied perpendicular to the quantum well

(ON), the wavefunctions of an electron and a hole are pushed toward the edges of the well. The electron subband energy E_e decreases while the hole subband energy E_h increases, causing the decrease of energy difference between the conduction and valence bands: $hv_1 < hv_2$. Moreover, as shown in Fig. 1-3(b) the larger the electric field, the smaller the energy difference [39]. Similar to Franz-Keldysh effect, the permitted light absorption frequency is reduced, or the absorption spectrum shifts to longer wavelength in the presence of applied electric field.

The quantum-confined Stark effect has been found in AlGaAs/GaAs quantum well structures [37], Ge/SiGe quantum wells [15], semiconductor quantum dots [40], and so on.

1.2.4 Plasma dispersion effect

Another physical effect that simultaneously achieves electro-refraction and electro-absorption is called plasma dispersion effect, or free carrier plasma dispersion effect, which is induced by the change of free carrier concentration in a material. According to the Drude theory, the equation of motion of an electron is given as [41],

$$e\vec{E} = m \frac{d\vec{v}}{dt} + \frac{m\vec{v}}{\tau}, \quad (1.2)$$

where e is the electron charge, m is the electron mass, τ is the scattering time, $\vec{E} = E_0 e^{-\omega t}$ is the electric field intensity, the electron velocity \vec{v} , thus can be expressed as

$$\vec{v} = \frac{q\vec{E}}{-i\omega m + m/\tau}. \quad (1.3)$$

Plug this into Maxwell's equation, we have

$$\begin{aligned}\nabla \times \vec{H} &= \frac{\partial \vec{D}}{\partial t} + \vec{J}_p = -i\omega \varepsilon \vec{E} + eN\vec{v} \\ &= i\omega \varepsilon_0 \left\{ \varepsilon_r + i\varepsilon_i - \frac{(\omega_p \tau)^2}{(\omega \tau)^2} \frac{(\omega \tau)^2 - i\omega \tau}{(\omega \tau)^2 + 1} \right\} \vec{E} = -i\omega \varepsilon_0 \varepsilon \vec{E},\end{aligned}\quad (1.4)$$

where \vec{H} is magnetic field intensity, \vec{J}_p is the polarization current density, ε_0 is the free space permittivity, $\omega_p = \sqrt{\frac{Ne^2}{m^* \varepsilon_0}}$ is the plasma frequency defined by free carrier concentration N and effective mass m^* . Then we obtain the material relative permittivity

$$\varepsilon = \varepsilon_r + i\varepsilon_i - \frac{(\omega_p \tau)^2}{(\omega \tau)^2} \frac{(\omega \tau)^2 - i\omega \tau}{(\omega \tau)^2 + 1} = (n + i\kappa)^2. \quad (1.5)$$

By separating the real and imaginary part of ε , we can get the relation between the real part n and imaginary part κ of the refractive index

$$\begin{cases} n^2 - \kappa^2 = \varepsilon_r - \frac{(\omega_p \tau)^2}{(\omega \tau)^2 + 1} \\ 2n\kappa = \varepsilon_i + \frac{(\omega_p \tau)^2}{\omega \tau [(\omega \tau)^2 + 1]} \end{cases} \quad (1.6)$$

Note that the average drift mobility is given by $\mu = e\tau/m$, and $n = n_0 + \Delta n$, $\kappa = \kappa_0 + \Delta \kappa$. n_0 and κ_0 represent the real and imaginary refractive index at intrinsic state. Also, consider the following conditions at infrared wavelengths, $\omega \tau \gg 1$, $n \gg \kappa$, and $n_0 \gg \Delta n$, then change of refractive index and absorption coefficient can be derived,

$$\begin{cases} \Delta n = -\frac{e^2 \lambda^2}{8\pi^2 c^2 \varepsilon_0 n_0} \frac{N}{m} \\ \Delta a = \frac{4\pi \Delta \kappa}{\lambda} = \frac{e^3 \lambda^2}{4\pi^2 c^2 \varepsilon_0 n_0} \frac{N}{m^2 \mu} \end{cases} \quad (1.7)$$

By considering the contribution of both electrons and holes, the above equations can be rewritten as

$$\begin{cases} \Delta n = -\frac{e^2 \lambda^2}{8\pi^2 c^2 \varepsilon_0 n_0} \left(\frac{\Delta N_e}{m_e} + \frac{\Delta N_h}{m_h} \right) \\ \Delta a = \frac{4\pi \Delta \kappa}{\lambda} = \frac{e^3 \lambda^2}{4\pi^2 c^2 \varepsilon_0 n_0} \left(\frac{\Delta N_e}{m_e^2 \mu_e} + \frac{\Delta N_h}{m_h^2 \mu_h} \right) \end{cases} \quad (1.8)$$

where ΔN_e and ΔN_h denote the carrier concentrations of electron and hole, respectively.

In Ref. [42], Soref and Bennett derived another way to estimate the change of refractive index based on the Kramers-Kronig relation,

$$\Delta n(\omega) = \frac{c}{\pi} P \int_0^\infty \frac{\Delta a(\omega_1)}{\omega_1^2 - \omega^2} d\omega_1, \quad (1.9)$$

where ω is the angular frequency, c is the speed of light, and P is the Cauchy principal value. For different electron and hole densities, the absorption spectrum of crystalline silicon was investigated, and the change of refractive index and absorption coefficient were calculated at different wavelengths. At the telecom wavelength of 1550nm, the relation between the change of refractive index Δn and free carrier concentrations is

$$\Delta n = \Delta n_e + \Delta n_h = -8.8 \times 10^{-22} \Delta N_e - 8.5 \times 10^{-18} (\Delta N_h)^{0.8}. \quad (1.10)$$

Similarly, the change in absorption coefficient is given by

$$\Delta \alpha = \Delta \alpha_e + \Delta \alpha_h = 8.5 \times 10^{-18} \Delta N_e + 6 \times 10^{-18} \Delta N_h. \quad (1.11)$$

The plasma dispersion effect evaluates the change of refractive index and absorption coefficient as a function of the electric field induced change of carrier concentration. The interaction between carrier concentration in material and propagating light can be

categorized into three different mechanisms including carrier injection, carrier accumulation and carrier depletion. All the three mechanisms have found applications in EO modulation with advantages and disadvantages [43]. For example, modulators based on carrier injection have small losses, but their speed is relatively low due to long carrier combination times. The speed of carrier-accumulation modulators is not limited by minority carrier lifetime, but they suffer from device RC delay and lack modulation efficiency. The carrier-depletion-based modulators are simple for processing, and offer high operation speed, but their working efficiency is limited by a lower number of involved carriers, which require further optimization [44-46].

1.3 Materials for EO modulation

Microelectronics could not develop without silicon, nor could EO modulators without proper materials. The EO properties of many materials have been revealed and investigated. Different applications and mechanisms determine the appropriate material. In this section, we introduce a few commonly used EO materials, and particularly focus on two materials that receive intense research interest in recent years, graphene and conductive oxide (COx).

1.3.1 Dielectric crystals

Crystals, such as $\text{NH}_4\text{H}_2\text{PO}_4$ (ADP), KH_2PO_4 (KDP), LiNbO_3 , LiTaO_3 , are known for their electro-optic effect, and have popular applications in EO modulators [38]. Typically, they provide high-speed light modulation with low power consumption [47,48]. However, the modulation effects are rather weak in these materials due to very small electro-optic

coefficients [38]. They are not compatible with existing silicon-based platforms, which makes it difficult to integrate with CMOS technology. Besides, due to the poor EO properties, modulators based on these materials are usually in millimeter scale, prohibiting the wide application in integrated electronic and photonic circuits.

1.3.2 Group IV materials

Electronic fabrication lines prefer silicon-based CMOS-compatible materials, including silicon and germanium. Silicon is the material that dominates the microelectronics industry. It is always a preferred choice for optoelectronics considering cost-effectiveness and ease of fabrication, for all applications where infrared light beyond the silicon absorption edge is to be guided, filtered, modulated and switched [49,50]. EO modulators based on silicon can be manufactured in a CMOS compatible fabrication process, promise full integrality with existing electronic platforms. The most popular effect investigated and used for modulation in silicon is the plasma dispersion effect, where p-i-n diode structures are usually deployed in an optical waveguide to electrically control the behavior of free carriers in the path of propagating light [43,51]. Recently, a state-of-the-art athermal silicon modulator based on a vertical p-n junction has been demonstrated and characterized, with high speed, low driven voltage, and ultralow power consumption being simultaneously achieved [52]. Meanwhile, the Franz-Keldysh effect and quantum-confined Stark effect have been utilized by using silicon-based materials. For example, both effects have been demonstrated in GeSi [17,53]. Furthermore, in Ref. [15], quantum-confined Stark effect in pure Ge is also reported. As a result, germanium is also a promising material for high-speed EO modulation.

1.3.3 III-V semiconductors

The application of III-V semiconductors in EO modulation are mostly based on GaAs and InP, which have provided popular platforms for photonic devices [54]. GaAs and InP based EO modulation can not only be caused by the electro-optic effects, but also the Franz-Keldysh effect and the quantum confined Stark effect. GaAs and InP have a direct bandgap, which makes them suitable materials for laser or detector applications [55, 56]. III-V semiconductors exhibit higher nonlinearities and larger bandgaps than group IV materials, but they are expensive, and the integration still faces many challenges. However, successful integration of electronics and photonics based on GaAs and InP would bring high-speed high-quality integrated circuits.

1.3.4 Non-linear polymers

Organic non-linear polymers have been considered as promising alternative EO materials for their advantages such as large Pockels coefficient, ultrafast response times, relatively low dielectric loss, and compatibility with other materials and substrates [57]. Compared with other materials, non-linear polymers are inexpensive and more practical materials especially for filling nanoscale gaps or slots in waveguides [58]. A plasmonic phase modulator with a compact size ($\sim 29\mu\text{m}$) has been proposed for high-speed operation (40Gbit/s) [59]. A more recent all-plasmonic Mach-Zehnder modulator has reached speed of 70 GHz, and the deployment of non-linear polymer provides large bandwidth, low energy consumption (25fJ/bit) and cheap integration method with electronic platforms [60]. While in the stage of development, non-linear polymer-based subsystems have

foreseeable benefit on next generation hybrid EO devices for telecommunication, data transfer, and sensing applications.

1.3.5 Graphene

As a cutting-edge technology, graphene may also find applications in EO modulation with its unique advantages as follows: (1) High speed: with a tremendously high carrier mobility ($2 \times 10^5 \text{ cm}^2 \text{V}^{-1} \text{s}^{-1}$) at room temperature, graphene is treated as one of the most prospective materials of next-generation ultrafast optoelectronic devices [61]. An operation speed of over hundreds of GHz can be expected owing to the ultrafast carrier processes in graphene [62]. As a result, the Fermi level, which is directly related to the optical absorption of graphene, can be rapidly modulated by applied voltage. This process actually reveals the modulation ability in graphene. (2) Broad bandwidth: due to its unique electronic structure [22,63], monolayer graphene has a constant light absorption of $\pi\alpha = 2.293\%$ all the way from visible to infrared regime [64]. Here $\alpha = e^2/\hbar c$ denotes the fine-structure constant [28]. The telecom bandwidth is fully covered by the graphene absorption range. (3) Efficient absorption: considering only one atom thickness, an optical absorption of $\sim 2.3\%$ is quite high. For comparison, GaAs with a thickness 50 times that of monolayer graphene absorbs the same amount of light. By integrating graphene with other structures or waveguides, the light-graphene interaction can be further enhanced [65]. (4) CMOS-compatible: large-scale graphene can be integrated with CMOS-compatible processes according to research in the past decade [66,67].

Graphene has a unique electronic structure in that the conduction band and valence band meet at Dirac points like two cones [22,63], which determines a linear dispersion relation in the vicinity of Dirac points. Therefore, carrier behavior that can be modeled as massless Dirac fermions. For pristine graphene, only interband transition is allowed, and the transmittance is frequency-independent and only determined by the fine-structure constant $\alpha=e^2/\hbar c$ (where e is the electronic charge, \hbar is the reduced Planck's constant, and c is the speed of light) [64]:

$$T = (1 + 2\pi G/c)^{-2} \approx 1 - \pi\alpha \approx 0.977 \quad (1.12)$$

When doped, the optical transmission of graphene is mainly determined by chemical potential μ , which can be tuned by chemical doping or electrical gating. Two absorption processes, interband absorption and intraband absorption, coexist in the light-graphene interaction. According to the Kubo formula, the two processes can be evaluated by a complex conductivity

$$\sigma_g = \sigma_{inter}(\omega, \mu, \Gamma, T) + \sigma_{intra}(\omega, \mu, \Gamma, T), \quad (1.13)$$

which depends on angular frequency of light ω , chemical potential μ , charged particle scattering rate Γ , and temperature T . Both interband transition and intraband transition are related to μ and ω . When $\mu = 0$, no intraband absorption will happen. When $|\mu| < \hbar\omega/2$, interband absorption dominates and graphene becomes absorptive. Otherwise, graphene is quite transparent to visible and NIR light.

In Ref. [32], graphene interacts with light propagating in silicon waveguide and offers absorption. By electrically tuning the Fermi level, the interband absorption in graphene can

be turned on and off. This graphene-based EO modulator has an operation speed of 1.2 GHz, and a modulation efficiency of 0.1dB/ μm . Its working bandwidth is from 1350nm to 1600nm, which covers the telecom regime. Meanwhile, intraband absorption can be equally important in graphene modulator. Lu and Zhao theoretically show that the optical conductivity of graphene changes with different chemical potential, resulting in a significant shift in dielectric constant. A modulation depth of 4.42dB/ μm can be achieved when graphene sandwiched inside the silicon waveguide, which shows great promise to make EO modulators into nanoscale [68].

Graphene shows great potential for broadband and ultrafast EO modulation. The manipulation in interband and intraband absorption in graphene is the main mechanism for modulation. The modulation speed of experimentally demonstrated graphene-based EO modulators is limited to approximately 1 GHz due to the RC constant. Following the first demonstration, many optical modulators enhanced by graphene have been theoretically and experimentally demonstrated. Graphene also shows great promise for ultrafast all-optical modulation with the picosecond level relaxation time, but direct measurement of a high speed is yet to be demonstrated. Besides, modulation of waves in terahertz range by graphene-based modulators is highly possible and has become a booming topic. In principle, much effort is needed to experimentally realize the promising potential of graphene.

1.3.6 Conductive oxide (CO_x)

Conductive oxides (COx), for instance, indium tin oxide (ITO) and aluminum-doped zinc oxide (AZO), are doped metal oxides that attract intensive research interest. They have a large bandgap that makes them visibly transparent, so they are conventionally used as transparent electrodes in solar cells and liquid-crystal displays [69-72]. The optical response of COx is governed by free electrons, whose density is controlled through the addition of *n*-type dopants. The moderate free carrier concentrations (10^{19}cm^{-3} - 10^{21}cm^{-3}) in COx make their plasma frequencies lie in the NIR range. Therefore, COx can exhibit metallic properties in NIR and mid-infrared (MIR) ranges and can be exploited for subwavelength light manipulation (Fig. 1-4). Moreover, the carrier concentration in COx can be controlled by growth/deposition conditions and post-annealing process [58, 73-75], resulting in an adjustable dielectric constant, which provides certain advantages for designing various plasmonic and nanophotonic devices. In addition, COx can be fabricated with standard physical vapor or chemical vapor deposition process and they are CMOS compatible.

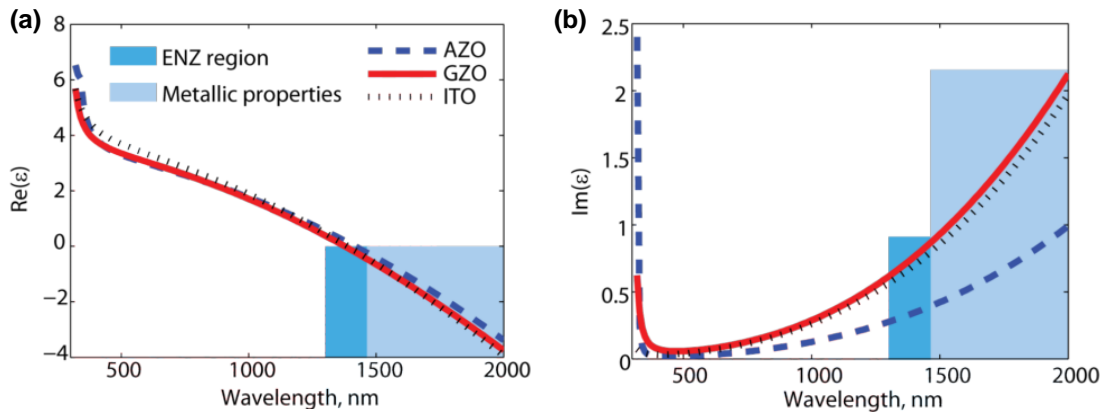


Figure 1-4. (a) Real and (b) imaginary parts of the dielectric constant of highly doped conductive oxides. Shaded areas correspond to wavelengths where COx exhibit metallic properties [58].

Plasmonics has been considered as the next generation technology that combines high speed of photonics with the nanoscale integration of nanoelectronics. Owing to the metallic properties shown in NIR region as well as small losses compared with noble metals (e.g. AZO could have losses four times smaller than silver in NIR), COx are treated as promising alternative plasmonic materials. The exploration of COx as the plasmonic metamaterial for NIR applications can be traced back to decades ago [76-78]. The past decade has witnessed more intensive study on plasmonic properties of COx, which includes realization of high doping and negative permittivity [75], surface plasmon polariton (SPP) guiding [79], tunability of localized surface plasmon resonance (LSPR) [80], negative refraction [81] as well as perfect absorption [82].

EO modulation can also be realized by utilizing COx in ultra-compact plasmonic devices. The modulation mechanism is relying on the free carrier plasma dispersion effect: the externally applied electric field changes the carrier concentration in COx, which results in the change of optical properties. For instance, a unity-order refractive index change in a 5-nm thick accumulation layer is achieved for a metal-insulator-metal (MIM) structure based on ITO [33]. Similarly, a large increase of carrier concentration within a 10 nm ITO film in a metal-oxide-semiconductor (MOS) structure is demonstrated [83]. As shown in Fig. 1-4, COx exhibits near-zero permittivity (epsilon-near-zero or ENZ) in NIR region, where light-matter interaction can be greatly enhanced. By taking advantage of this property, modulators based on COx could expect a large modulation depth. A Gallium-doped Zinc Oxide (GZO)-based plasmonic modulator has a theoretically predicted modulation depth of 46 dB/ μm [84], which may allow for ultra-compact modulators made

at the nanoscale. EO modulators based on CO_x could potentially work at a speed of over hundreds of GHz according to the mechanism. Besides, other advantages including broadband operation and low power consumption have been reported [83,85].

1.3.7 Graphene and CO_x thin films

As well known since its discovery, graphene has shown exceptional electrical, optical, thermal, as well as mechanical properties compared with bulk form of graphite, which make it very promising for optoelectronic applications. Besides, as the byproducts in the graphene synthesis processes, bi-layer and multi-layer (≥ 3) graphene have also been intensively investigated regarding to their electronic structures, transport properties, optical properties, etc [86-88], and various applications such as improving thermal conductivity [89,90] and saturable absorber [91], have been enabled. The effective Hamiltonian of graphene is shown to be equivalent to the Dirac Hamiltonian for a zero-mass particle, where the conduction band and valence band with linear dispersion touch at the so-called Dirac point. In bi-layer and multi-layer graphene, the interlayer coupling drastically changes the band structure, giving characteristic features depending on the number of layers and the stacking manner [92,93]. For example, the carrier mobility of CVD graphene can be limited by the scattering in bi-layer and multi-layer domains [94]. The issue is that graphitic AB stacking breaks the equivalency of sublattice atoms in a graphene sheet, so that multilayer films should not exhibit the graphene-like properties [95]. However, researchers also found that multi-layer graphene synthesized by epitaxy growth on SiC showed single-layer electronic properties due to epitaxial condition-induced rotational

stacking faults [96]. As a result, multi-layer graphene with tens of layers could also exhibit very high carrier mobilities.

For CO_x, researchers found that thinner films could lead to higher bandgap, decreased effective mass, and substantially higher carrier density [97]. For better EO modulation performance, the CO_x thickness should be as small as possible to reduce losses while keeping the main feature of the layer—ENZ behavior at NIR wavelengths. Thus, research efforts should be put towards the fabrication of ultra-thin, smooth continuous films of CO_x. Some theoretical studies consider thinner layers, for example, a few nanometers [98], which will provide better performance. However, ultra-thin CO_x may cause significantly differed electrical and optical properties [99], and the crack and surface problem due to delicate films could degrade the field effect for EO modulation. Besides, thinner CO_x films would lead to much increased resistance and thus contribute to larger device RC constant. As a result, the feasibility of ultra-thin CO_x films (a few nanometers) in realizing efficient EO modulation still needs verification.

1.4 Fabrication techniques for graphene and conductive oxide

Materials have significant impacts on the design, fabrication, and performance of devices. The desired functionalities of devices in return determines the fabrication techniques of materials. The properties of graphene and conductive oxide can vary a lot due to different fabrication processes. In this section, a general introduction of fabrication techniques for graphene and conductive oxide will be presented.

1.4.1 Graphene synthesis, transfer and characterization

Since first successful isolation of monolayer graphene in 2004 by mechanical exfoliation method (or scotch tape method) [21], many approaches and processes have been developed to produce single-to-few layer graphene. The major concern in graphene synthesis is to produce samples with high carrier mobility and low density of defects. Among all the graphene synthesis methods, mechanical exfoliation is the best way to obtain high-mobility, high-quality graphene flakes. However, this method has poor production efficiency. The repeated peeling by scotch tape is a time-consuming process and only small sizes of graphene flakes (up to 1 mm in length [100]) can be produced. In order to synthesis graphene in large scale for various applications, other promising techniques have been investigated, which includes thermal decomposition [101, 102], chemical vapor deposition (CVD) [67, 103-106], molecular beam deposition [107], and chemical synthesis [108,109].

By heating silicon carbide in ultra-high vacuum (UHV) to temperatures between 1000°C and 1500°C, silicon would sublime from SiC surface and leave behind thin graphitic layers or sometimes monolayer graphene. This method is called thermal decomposition [101]. The number of layers is dependent on the decomposition temperature. By annealing SiC in noble gas atmosphere as opposed to UHV, researchers have obtained much larger continuous graphene layers with reduced surface roughness [102]. This technique is capable of generating wafer-scale graphene layers.

CVD is a popular method to produce large-scale graphene at a relatively low cost. In CVD process, carbon is supplied by injected gas. A metal substrate is necessary to seed the growth of graphene, where Ni and Cu are most commonly used. After graphene growth, the metal catalyst needs to be etched away to allow graphene to be transferred to other

substrates. The growth of monolayer, bilayer and few-layer graphene on Cu have been demonstrated [103-106], while on Ni, the graphene thickness is found to be dependent on the cooling rate. Three to four layers of graphene was produced with a cooling rate of 10°C/s , and thicker graphite layers could result from faster cooling rates [103]. The size of graphene by CVD method is determined by gas flow, pressure as well as temperature. A roll-to-roll process was reported to produce graphene layers with diagonal of up to 30 inches, as shown in Fig. 1-5 [67]. The carrier mobility of CVD grown graphene can reach a high value of $16000\text{ cm}^2\text{V}^{-1}\text{s}^{-1}$ [105].

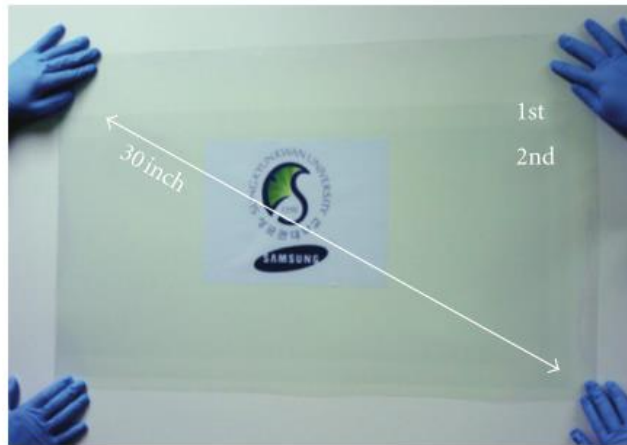


Figure 1-5. Multiple CVD graphene sheets with diagonal of up to 30 inches transferred to transparent flexible substrates [67].

Molecular beam deposition technique can be used to grow graphene layer-by-layer [107]. Starting with an ethylene gas source, gas was broken down at 1200°C by a thermal cracker and deposited on a nickel substrate. Large-area, high-quality graphene layers were produced at 800°C . By forming one layer on top of another, this method is capable of producing of one to several layers of graphene. Besides, in contrast to the CVD growth on

Ni, the number of graphene layers produced by molecular beam deposition was found to be independent of cooling rate.

Another technique for generating graphene is chemical synthesis. In this method, graphene oxide is first produced as a precursor for graphene. A commonly used procedure treats graphite in an anhydrous mixture of sulfuric acid, sodium nitrate, and potassium permanganate for several hours, followed by the addition of water [108]. The resulting graphite oxide solution can be sonicated to form graphene oxide flakes, which is then spin-coated on substrates to make monolayer or bilayer graphene oxide. Finally, graphene can be obtained by thermal or chemical reduction of graphene oxide [109].

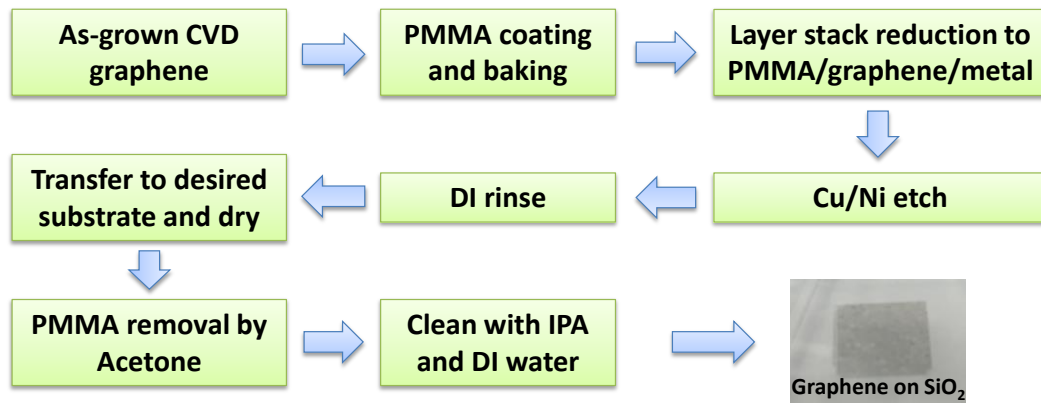


Figure 1-6. The process of graphene transfer. The picture of multilayer graphene on Ni transferred to glass substrate is shown at the end.

Commercially available, large area graphene grown by CVD process has been widely used in research. A key step to making use of as-grown graphene in various applications is to transfer graphene layer onto desired substrate such as Si or SiO₂. A polymer-assisted transfer process is commonly utilized. Fig. 1-6 illustrates the process in step-by-step. First, Polymethyl-methacrylate (PMMA) is coated on top of graphene, serving as both

supporting and protection layer. Then, depending on the substrate used to grow graphene, different methods are used to reduce the sample to a PMMA/graphene/metal (Cu or Ni) stack. If the seeding metal is on SiO₂/Si substrate, the sample will be immersed into buffered oxide etch (BOE) solution to etch SiO₂ away; if the substrate is just a metal foil, then the backside graphene needs to be removed by oxygen plasma. After that, the PMMA/graphene/metal stack will be further reduced to PMMA/graphene by applying metal etch solution (i.e. FeCl₃ or HNO₃). When the PMMA/graphene is thoroughly rinsed by deionized (DI) water to eliminate metal etch residue, it can be transferred to the desired substrate. Finally, after PMMA layer is removed by acetone, the transferred graphene is cleaned with isopropyl alcohol (IPA) and DI water. The figure includes a picture showing multilayer graphene on glass transferred from Ni/SiO₂/Si substrate. In order to get high-quality transfer, researchers have further optimized this process. For example, Li *et al* introduced a second PMMA coating step after PMMA/graphene is placed on the substrate [110]. Liang *et al* developed a “modified RCA clean” transfer process to better control both contamination and crack formation on transferred graphene [111].

Due to the atom-scale thickness and high transparency of graphene, it is important to identify it and characterize its structure after its synthesis. Raman spectroscopy is a non-contact, reflective technique, which provides a fast, nondestructive method to determine number of graphene layers, the stacking order as well as density of defects and impurities [112,113]. In Raman spectrum of graphene and other graphitic materials, three peaks are most prominent, namely G band at ~1580cm⁻¹, the D band at ~1350cm⁻¹, and the 2D band at ~2680cm⁻¹. The D band is induced by defects in graphene lattice. With its intensity

proportional to the defect level, D band is usually weak in high-quality graphene. The number of layers of graphene can be determined by the band shape of the 2D peak, as well as its intensity relative to G peak, as shown in Fig. 1-7(a). As the layer number increases, the 2D band becomes broader, less symmetric, and less intensive [114].

In order to quickly identify few- to single-layer graphene made from mechanical exfoliation, an optical microscope is usually used. Fig. 1-7(b) shows one, two and three layers of exfoliated graphene on SiO₂ observed under an optical microscope [115].

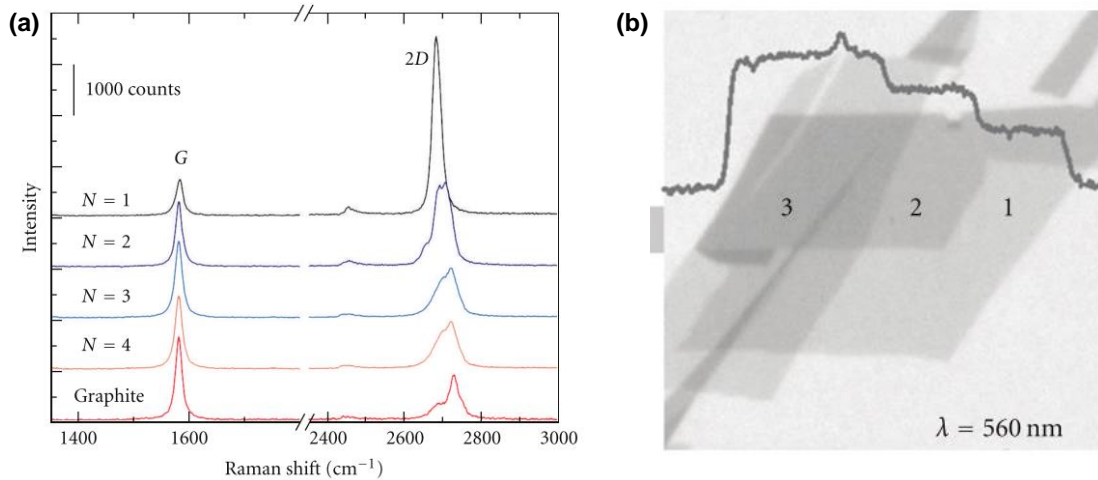


Figure 1-7. (a) Layer dependence of graphene Raman spectrum. Raman spectra of N=1-4 layers of graphene on Si/SiO₂ and of bulk graphite [112]. (b) Optical microscope image of multilayer graphene sheet on Si/SiO₂[115].

1.4.2 Fabrication of conductive oxide

Thin films of CO_x can be deposited by many physical-vapor and chemical-vapor deposition techniques. Techniques such as sputtering and pulsed-laser-deposition (PLD) can produce high conductive CO_x films. As mentioned before, it has great flexibility to obtain CO_x with varied properties by controlling the deposition process. Since CO_x are doped metal oxides, the dopant concentration and oxygen flow ratio can both determine

the thin film properties. Besides, the fabrication environment, such as temperature and pressure can be equally important. Researchers have conducted investigations on these effects [116,117]. Fig. 1-8 (a,b) plot the dependence of real and imaginary permittivity of AZO on oxygen pressure, respectively; while for AZO, GZO, and ITO, the cross-over frequencies where the real permittivity crosses zero, and their damping factors as a function of dopant concentration are illustrated in Fig. 1-8(c,d).

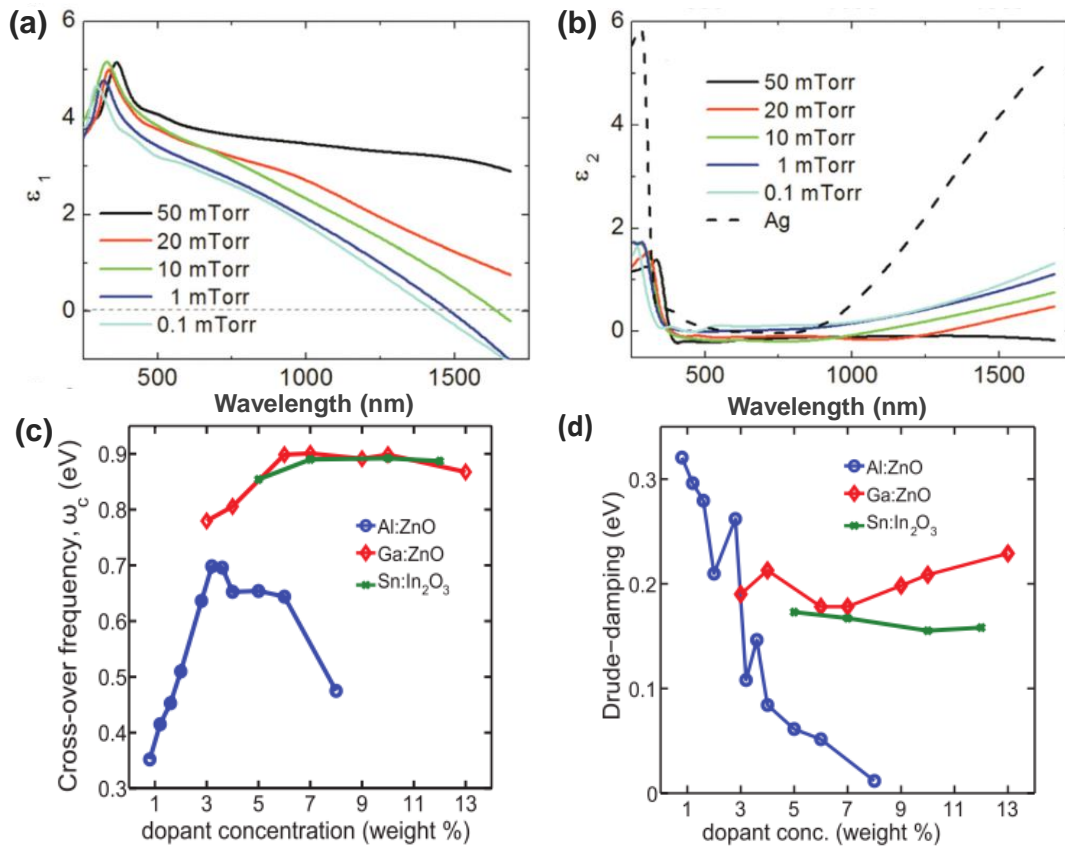


Figure 1-8. Dependence of (a) real and (b) imaginary parts of AZO permittivity on oxygen pressures upon deposition [116]. Dependence of (c) cross-over wavelength and (d) Drude-damping coefficient of AZO, ITO, and GZO on different dopant concentrations [117].

In our experiments, we fabricate ITO thin films with two different tools. In Semiconductor & Microsystems Fabrication Laboratory (SMFL) of RIT, ITO thin film can be deposited by sputtering process with CVC601. The basis of sputtering is to use accelerated particles to bombard the target and knock the target atoms out. Then these free atoms will be deposited on the surface of the substrate. During the sputtering process, plasma is usually used since it contains charged particles; this low-pressure gas is easily directed by electric fields. To obtain plasma, a voltage will be applied across a pair of electrodes. Free electrons which gain energy from the electric fields will collide with gas particles, eventually causing ionization. This is known as direct-current glow discharge [118]. The sputtering process in CVC601 is using an $(\text{In}_2\text{O}_3)_{0.9}(\text{SnO}_2)_{0.1}$ weight percentage target, with chamber environment of room temperature and 7.3 mTorr pressure introduced by Argon. After sputtering, the ITO films will go through a post-deposition annealing process to achieve the desired properties [73,119]. ITO films can also be deposited by PVD75 sputtering tool in Cornell Nanoscale Science and Technology Facility (CNF) [120]. The tool uses a 90% Indium /10% Tin target to reactively sputter with the oxygen introduced into the chamber. The composition of the ITO can be varied by controlling the percentage of oxygen (2% to 12%) that is introduced into the chamber. The lower the oxygen content; the more uniform, but the less transparent and more metallic the film will be. The tool has substrate rotation and heating capabilities up to 350°C. Denser films can be created by heating the substrate.

1.5 Numerical analysis methods

Numerical analysis is an essential component in the research of electromagnetics. People make use of different numerical analysis methods to design and analyze structures, predict the device performance and verify the experimental results. Among many different methods, two of them play significant roles in my research, namely transfer matrix method (TMM) and finite-difference time-domain (FDTD) method. This section briefly introduces the principles of the two methods.

1.5.1 Transfer matrix method (TMM)

In optics, TMM is a method used to analyze the propagation of electromagnetic waves through a layered medium [38,121]. A wave incident on a layered medium undergoes reflections and transmissions at the layer boundaries. The complex amplitudes of transmitted and reflected waves may be determined by using Fresnel equations at each boundary, and the overall transmittance and reflectance of the medium can be calculated by superposition of the individual waves.

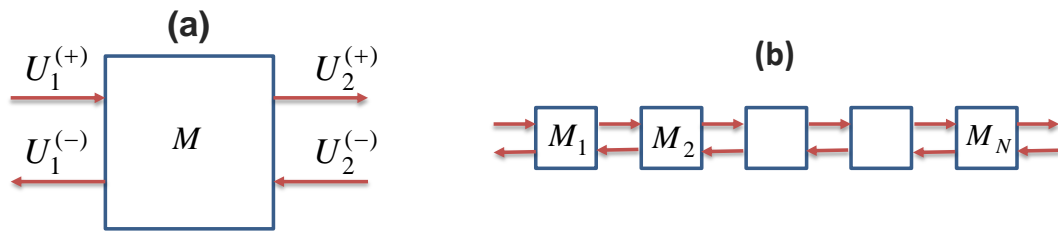


Figure 1-9. (a) Illustration of the transfer matrix of a medium. (b) Transfer matrices of each element in a multilayered system.

Consider the forward and backward waves in and out of a layered medium, as shown in Fig. 1-9(a). The complex amplitudes of the waves can be related by a matrix equation,

$$\begin{bmatrix} U_2^{(+)} \\ U_2^{(-)} \end{bmatrix} = \begin{bmatrix} A & B \\ C & D \end{bmatrix} \begin{bmatrix} U_1^{(+)} \\ U_1^{(-)} \end{bmatrix}, \quad (1.14)$$

The elements A, B, C and D forms the transfer matrix, M , which is determined by the optical properties of the layered medium. In detail, the scattering matrix S of a medium is first determined,

$$S = \begin{bmatrix} t_{12} & r_{21} \\ r_{12} & t_{21} \end{bmatrix}, \quad (1.15)$$

where the four elements are reflection and transmission coefficients calculated with Fresnel equations. Then, the transfer matrix can be converted from scattering matrix,

$$M = \begin{bmatrix} A & B \\ C & D \end{bmatrix} = \frac{1}{t_{21}} \begin{bmatrix} t_{12}t_{21} - r_{12}r_{21} & r_{21} \\ -r_{12} & 1 \end{bmatrix} \quad (1.16)$$

For a multilayered medium (Fig. 1-9(b)), the system transfer matrix can be obtained by the multiplication of the transfer matrices of each element,

$$M = M_N \cdots M_2 M_1 \quad (1.17)$$

Finally, the scattering matrix for the multilayers is determined by conversion from the system transfer matrix,

$$S = \begin{bmatrix} t_{12} & r_{21} \\ r_{12} & t_{21} \end{bmatrix} = \frac{1}{D} \begin{bmatrix} AD - BC & B \\ -C & 1 \end{bmatrix} \quad (1.18)$$

which can yield the amplitude reflectance and transmittance of the multilayers. For example, the reflectance of the whole system can be calculated by

$$R = \left| \frac{C}{D} \right|^2 \quad (1.19)$$

1.5.2 Finite-difference time-domain (FDTD) method

The FDTD method was originally introduced by Kane Yee in 1966 [122] and popularized by Allen Taflove in 1980 [123]. The Yee algorithm is based on time and spatial discretization of Maxwell's equations to obtain solutions for the EM field in the time domain. The spatial domain is decomposed into cubic unit cell filling all the computational space, shown in Fig. 1-10. The dimension of the cubic unit cell, $\Delta x \times \Delta y \times \Delta z$, determines the discretization of space derivative.

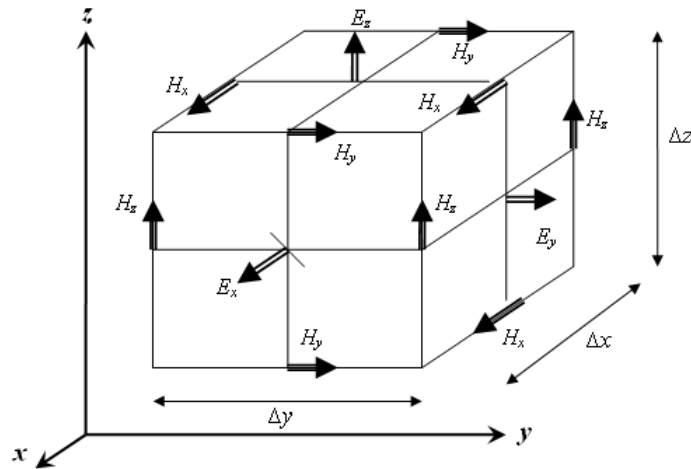


Figure 1-10. The distribution of E -field and H -field components in Yee cell.

The method is numerically implemented by continuously sampling the electromagnetic field over the wave propagation medium in the cubic cell. Start with Maxwell's curl equations:

$$\frac{\partial \vec{E}}{\partial t} = \frac{1}{\epsilon} \nabla \times \vec{H} \quad (1.20)$$

$$\frac{\partial \vec{H}}{\partial t} = -\frac{1}{\mu} \nabla \times \vec{E} \quad (1.21)$$

where \vec{E} is the electric field, \vec{H} is the magnetic field, ϵ is the medium permittivity and μ is the permeability. Expanding the vector components of Eq. (1.20) and (1.21) produces six scalar equations in Cartesian coordinates:

$$\frac{\partial E_x}{\partial t} = \frac{1}{\epsilon} \left(\frac{\partial H_z}{\partial y} - \frac{\partial H_y}{\partial z} \right) \quad (1.22)$$

$$\frac{\partial E_y}{\partial t} = \frac{1}{\epsilon} \left(\frac{\partial H_x}{\partial z} - \frac{\partial H_z}{\partial x} \right) \quad (1.23)$$

$$\frac{\partial E_z}{\partial t} = \frac{1}{\epsilon} \left(\frac{\partial H_y}{\partial x} - \frac{\partial H_x}{\partial y} \right) \quad (1.24)$$

$$\frac{\partial H_x}{\partial t} = \frac{1}{\epsilon} \left(\frac{\partial E_y}{\partial z} - \frac{\partial E_z}{\partial y} \right) \quad (1.25)$$

$$\frac{\partial H_y}{\partial t} = \frac{1}{\epsilon} \left(\frac{\partial E_z}{\partial x} - \frac{\partial E_x}{\partial z} \right) \quad (1.26)$$

$$\frac{\partial H_z}{\partial t} = \frac{1}{\epsilon} \left(\frac{\partial E_x}{\partial y} - \frac{\partial E_y}{\partial x} \right) \quad (1.27)$$

These scalar equations form the basis of FDTD algorithm for modeling electromagnetic waves in arbitrary three-dimensional structures. As can be seen in Fig. 1-10, all E -field and H -field components are placed in an interlinked array inside the Yee cell.

In Yee algorithm, the E -field components in a volume of space are first computed at a given instant in time; then the H -field components in the same spatial volume are solved at the next instant in time, based on the previously computed H -field components and newly updated E -field data. The leapfrog process is repeated over and over again until the desired transient or steady-state electromagnetic field behavior is fully evolved [124].

The most prominent advantage of FDTD method is its simplicity in solving Maxwell's equations. There are also limitations in the implementation of the technique. For example, the method requires the length of the grid cell to be much shorter than the wavelength of the wave inside the cell, which may hinder the application of the method in solving a variety of problems. This constraint is brought by both sampling limitation and grid dispersion errors. Another important restriction is that the Courant condition needs to be satisfied to ensure the computing stability [125]. The condition imposes constraints on time increments to prohibit waves to travel too far in each time increment. In three dimensions, the condition is described by the following equation:

$$\frac{1}{V_{p,max}\Delta t} \geq \left(\frac{1}{\Delta x^2} + \frac{1}{\Delta y^2} + \frac{1}{\Delta z^2} \right)^{1/2}, \quad (2.28)$$

where $V_{p,max}$ is the maximum phase velocity of electromagnetic waves in the model.

1.6 Dissertation overview

The goal of this dissertation presents analytical, numerical and experimental results of realizing enhanced light absorption as well as EO modulation based on novel photonic materials, graphene and COx. These results are structured as follows:

Chapter 2 presents the numerical modeling and experimental demonstration of greatly enhanced light absorption by monolayer graphene over a broad spectral range, based on an attenuated total reflection (ATR) configuration. An EO modulator is proposed and investigated based on the experimental validation of enhanced absorption. Besides, a structure that utilizes multilayer graphene to absorb a large amount of broadband,

unpolarized light is numerically studied. The potential application of the structure in photovoltaics is briefly discussed.

Chapter 3 presents the theoretical and numerical study of a novel ENZ-slot waveguiding structure based on CO_x. Greatly enhanced light matter interaction is realized when the active material, ITO, is tuned to ENZ state by an applied electrical signal. This helps the design of nanoscale EA modulators with modulation depth over 20 dB/μm. Another application of the CO_x based ENZ-slot waveguide in laser beam steering made possible by significant effective index change of the waveguide, is also demonstrated.

Chapter 4 continues the study in Chapter 3, and experimentally demonstrates field-effect EA modulators based on a metal-insulator-CO_x (MIC) structure. The modulators exhibit a broadband bias-polarity-dependent modulation effect, where both carrier accumulation and depletion contribute to the EA modulation. ENZ effect is observed for the active material, ITO.

In Chapter 5, an ultra-compact field-effect EA plasmonic modulator is designed, fabricated and characterized. Based on both carrier accumulation and depletion, the modulator has an effective modulation length of only 800 nm. Preliminary results show that it has an extinction ratio of 3.04 dB/μm at 10 MHz, works up to 500 MHz and can potentially operate at high speed.

Chapter 6 focuses on the numerical analysis of nanoscale field effect optical modulators based on depletion of ENZ films. In the simulation, the depletion of a 4-nm thin ENZ ITO

film will result in an extinction ratio of 7.86dB for modulator based on the plasmonic platform, and 3.44dB for that based on the dielectric platform.

Chapter 7 experimentally demonstrates a COx-based EA modulator integrated in a dielectric platform. The modulator has an ultra-compact footprint of $4 \mu\text{m}^2$. Besides, it exhibits up to 2 GHz operation speed at telecommunication wavelengths, which is expected to be further boosted by optimizing device circuit designs.

Chapter 8 will present the summary of this dissertation as well as an outlook for potential future work.

2. ENHANCED LIGHT ABSORPTION BY GRAPHENE

In this Chapter, based on a novel graphene-sandwiched structure, enhanced light absorption by monolayer graphene over a broad spectral range will be demonstrated. In the experiment, graphene is sandwiched between two dielectric media referred as superstrate and substrate. Based on the experimental results, up to 42.7% transverse electric (TE)-polarized light absorption has been achieved [126]. Furthermore, by changing the materials of the superstrate and substrate, multilayer graphene could absorb 70%-80% of unpolarized incident light, which may provide possibilities for detectors and photovoltaic devices [127].

2.1 Introduction

Graphene can support remarkably high density of electric currents [24], and has high thermal conductivity [26] and elasticity [128]. At room temperature, the electron mobility of graphene is extremely high [129]. This enables graphene a desirable material in the advancement of nanoelectronics [23]; for example, metal-oxide-semiconductor field effect transistor (MOSFET) channels [130], graphene nanoribbons [131-133], bilayer graphene transistor [134] and perforated graphene transistors [135-137]. The optical properties of graphene have intrigued considerable interest as well [27]. Recent research revealed gate-variable optical conductivity [30] and high-speed operation [29] of graphene. These extraordinary properties combine with its high electron mobility make graphene a

promising candidate satisfying the need of broadband optical modulators [31,32,68,138] and photodetectors [30,139,140].

2.2 Enhanced polarized light absorption by monolayer graphene

2.2.1 Background

Light absorption can go up to $\pi\alpha = 2.293\%$ (α is the fine-structure constant) [141,142] over a broad wavelength range when light is normally incident through monolayer graphene. By considering its single atom thickness, the interaction between light and graphene is quite strong, the absolute value ($\sim 2.3\%$) of absorption is still weak for many optoelectronic applications where a strong light-matter interaction is usually desired [143,144]. Therefore, novel approaches need to be explored to enhance light absorption of graphene. Some researchers have proposed graphene photodetectors integrated with plasmonic nanostructures [144] or nanoparticles [145] where the responsivity can be significantly enhanced due to the localized surface plasmons. It was also demonstrated that over 60% absorption can be reached by integrating graphene with a microcavity structure [140]. More recent work suggested monolayer graphene-based photodetector with ultrahigh photoresponsivity relying on band structure engineering [146]. However, all these methods mentioned above either need complicated, time-consuming fabrication processes [140,146] or the devices exhibit very narrow bandwidth [140,145,147]. An easily fabricated graphene-based device with a broadband performance is then desired for fundamental research and practical applications.

Herein, we present a simple approach to greatly enhance optical absorption of monolayer graphene over a broad spectral range, from visible to near infrared, based on an attenuated total reflection (ATR) configuration. This configuration has been used to measure the graphene absorption spectra [148], analyze terahertz surface plasmons on graphene [149], estimate number of carbon layers in an unknown graphene sample [150], and more recently, enhance coherent light absorption by graphene [151]. In Ref. [151], up to 10% visible light ($\lambda=525\text{nm}$ to 800nm) absorption by monolayer graphene was demonstrated through an F2 prism coupling into a graphene-sandwiched silica waveguiding structure. In our work, we found that by utilizing an even simpler structure, (1) absorption nearly 100% can be theoretically achieved; and (2) the enhanced absorption can be achieved within an ultrabroad band, all the way from visible to near infrared.

2.2.2 Numerical analysis

The proposed graphene-sandwiched structure is shown in Fig. 2-1(a). It consists of three layers, superstrate, graphene, with refractive indices named by n_1 , n_2 , and n_3 , respectively. Light is obliquely incident into the three-layer structure, and the corresponding propagation angles to the normal direction are θ_1 , θ_2 , and θ_3 , respectively. According to Snell's law, $n_q \sin \theta_q = n_1 \sin \theta_1$ ($q=1, 2, 3$). Based on the TMM, the amplitude reflectance can be calculated by

$$r = \frac{(\tilde{n}_3 - \tilde{n}_2)(\tilde{n}_2 + \tilde{n}_1)e^{+j\tilde{\varphi}_2} + (\tilde{n}_3 + \tilde{n}_2)(\tilde{n}_2 - \tilde{n}_1)e^{-j\tilde{\varphi}_2}}{(\tilde{n}_3 - \tilde{n}_2)(\tilde{n}_2 - \tilde{n}_1)e^{+j\tilde{\varphi}_2} + (\tilde{n}_3 + \tilde{n}_2)(\tilde{n}_2 + \tilde{n}_1)e^{-j\tilde{\varphi}_2}} \quad (2.1)$$

where $\tilde{\varphi}_2 = n_2 k_0 d \cos \theta_2$ (k_0 is the wavenumber of the light wave in free space; $d \approx 0.335\text{nm}$ is the thickness of graphene). Also, $\tilde{n}_q = n_q \cos \theta_q$ ($q=1, 2, 3$) for TE-polarized

light (i.e. electric field is parallel to the three-layer structure), and $\tilde{n}_q = n_q / \cos\theta_q$ ($q=1, 2, 3$) for TM-polarized light.

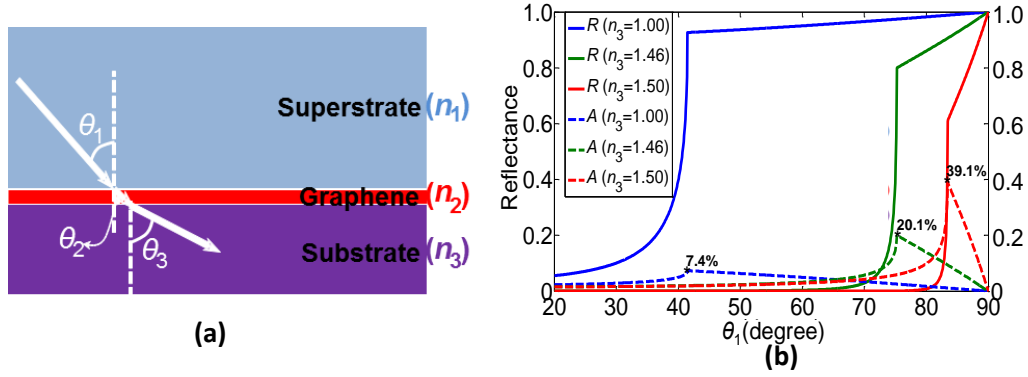


Figure 2-1. (a) Illustration of the graphene-sandwiched structure. (b) Numerical calculation of the reflectance and absorption as functions of incident angle, θ_1 , and substrate refractive index n_3 .

We assume the refractive index of the superstrate is $n_1=1.51$ at $\lambda=650\text{nm}$, and first consider the TE-polarized light case. The solid lines in Fig. 2-1(b) plot the power reflectance $R = |r|^2$ as a function of the incident angle θ_1 and substrate refractive index. Similarly, the power transmittance T can be calculated by transfer matrix method. The absorption $A=1-R-T$. The dashed lines in Fig. 2-1(b) plot the $A-\theta_1$ relations for different substrates. Almost identical curves can be obtained at $\lambda=1520\text{nm}$ or even longer wavelengths if n_1 and n_3 remain the same as their corresponding values.

From the graph, we can see that the maximum absorption occurs at the critical angle $\theta_c = \sin^{-1}\left(\frac{n_3}{n_1}\right)$ for each case. Based on the three-layer model, the absorption grows with the increase of n_3 . If $n_3 < n_1$. The closer n_3 to n_1 , the larger the absorption is. The maximum absorption can be achieved is 7.4%, 20.1%, and 39.1% when the index of the substrate is

1.00, 1.46, and 1.50, respectively. In particular, the absorption can reach 79.6% when $n_3=1.509$. However, when $n_3>n_1$, the maximum absorption will sharply drop. In our work, we only consider the cases where $n_1>n_3$. The power transmittance $T=0$ when $\theta_1 \geq \theta_c$; thus, the incident power will be either reflected back or absorbed by graphene, i.e. $A=1-R$. The scattering by graphene is negligible as can be seen in the experimental result for TM-polarized light. In other words, when $\theta_1 \geq \theta_c$, the absorption can be easily measured by testing the reflectance. Furthermore, there is no cavity or resonant component involved in the structure. As a result, the absorption expression is not an explicit function of frequency, which implies that the same level of enhanced light absorption can be achieved in a broad band.

2.2.3 Experimental validation and discussion

To experimentally demonstrate the greatly enhanced light absorption by graphene, we have built an ATR setup in the Kretschmann configuration [152], as illustrated in Fig. 2-2(a). A collimated laser beam propagates through a broadband polarizer (P1) to choose either TE- or TM-polarization, and is then split into two by a beam splitter (BS). One beam is used for recording source power fluctuation and fed into a germanium photodiode (PD2); another is incident at the angle θ_1 into a BK7 glass hemicylindrical ($\varnothing 100\text{mm}$) lens, which functions as a coupling prism in this setup. The reflected light is then collected by another germanium photodiode (PD1). The power ratio between PD1 and PD2 can well measure the reflectance, R , even if there is power fluctuation in the laser source. The rotation of the prism (together with the graphene sample) and PD1 is in a $\theta_1-2\theta_1$ configuration, which is precisely controlled by two motorized rotation stages. In our experiment, we made one

measurement for every 0.25° increment of θ_1 . As a result, the reflectance, R , as a function of θ_1 can be plotted. The picture of the setup is shown in Fig. 2-2(b).

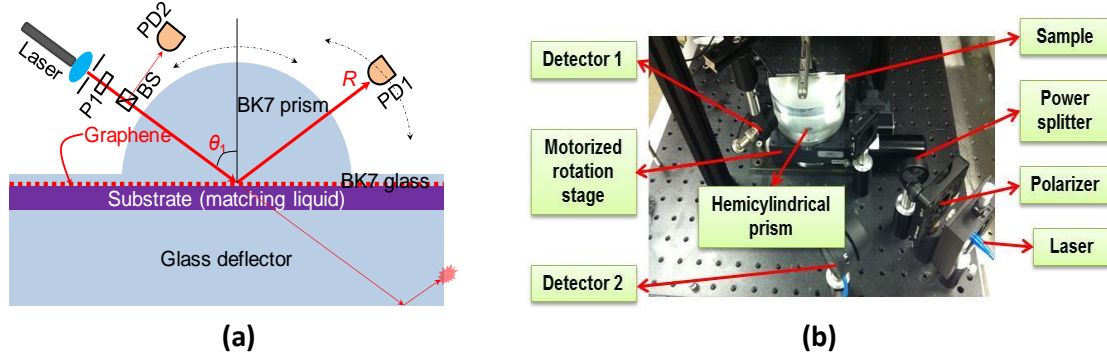


Figure 2-2. (a) Illustration of the experimental setup for ATR measurement. The red dashed line represents the monolayer graphene film. P1 and BS represent the polarizer and beam splitter, respectively. (b) Actual picture of the ATR test setup.

Our sample is commercially available monolayer graphene [153] synthesized by the CVD process then transferred to our bare BK7 glass slide. Its Raman spectroscopy result indicates that the sample is monolayer graphene with an obviously higher 2D peak than the G peak [154]. The graphene sample is mounted at the back of the hemicylindrical prism. To avoid a thin air gap between the prism and the graphene sample, a BK7 index matching liquid is applied between them. In this case, the superstrate can be simplified and treated as a BK7 medium, consisting of the BK7 prism and the BK7 glass slide. The medium on the other side of the graphene is referred as the substrate, which is another matching liquid from Cargille™ in our case to better control the refractive index. A thick (>10mm) glass plate is used to hold the matching liquid and meanwhile to deflect light away from PD1. In our work, we focused on TE-polarization and carried out the experiment in a step-by-step fashion. First, we tested the graphene on BK7 glass sample without any substrate (or

air as the substrate) but without the deflector. At the critical angle, the absorption of the monolayer graphene can be calculated as $A=1-R$, which is 7.6% (at $\lambda=650\text{nm}$) and 9.8% (at $\lambda=1520\text{nm}$). Based on the same sample and configuration, we also measured the absorption of graphene at longer wavelengths up to 1620nm. At the critical angle, the absorption of monolayer graphene is in the range of 7.6%-11.2%, which is 3~5 times stronger than the widely known absorption coefficient ($\sim 2.3\%$). When the incident angle is larger than the critical angle, the reflectance of graphene is observed to gradually increase and projected to be 100% at $\theta_1 = 90^\circ$.

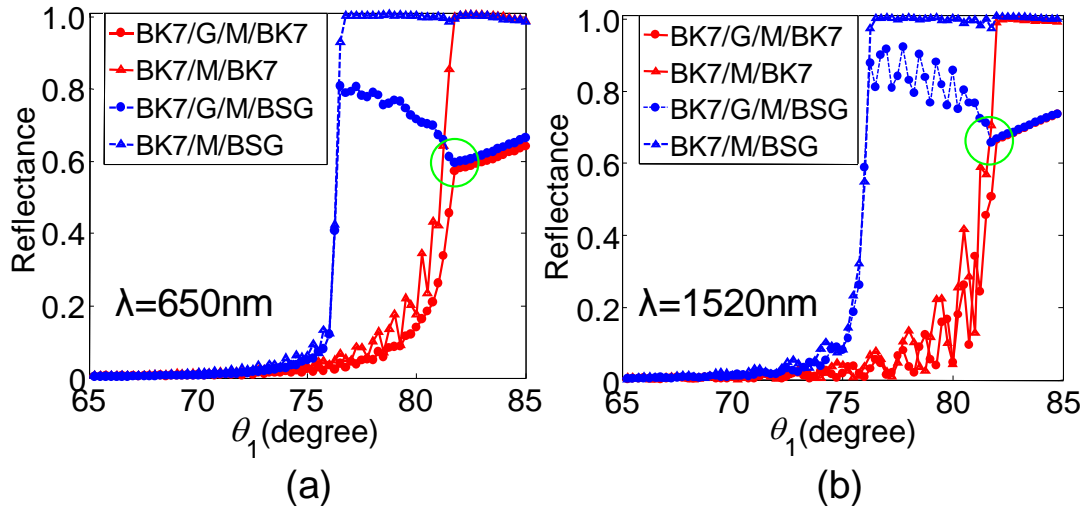


Figure 2-3. Measured reflectance of the monolayer graphene with M1.50 as the substrate under TE-polarized light incidence at (a) $\lambda=650\text{nm}$ and (b) $\lambda=1520\text{nm}$. In both graphs, red curves represent the results when a BK7 deflector is used; blue curves represent the results when a BSG deflector is used. In the legend, “G” and “M” represent “graphene” and “matching liquid”, respectively. “BK7/G/M/BK7” means the result for the BK7(prism)-graphene-M1.50(substrate)-BK7(deflector) configuration.

The absorption of the monolayer graphene can be further enhanced when the refractive index of the substrate increases. In our work, a matching liquid with refractive index 1.50

(at $\lambda=589.3\text{nm}$ according to the manufacturer; referred as “M1.50”) is applied as the substrate of the graphene. Two different supporting glass deflectors, BK7 and borosilicate glass (BSG), are separately used to hold the substrate M1.50. In Fig. 2-3, triangle points are the control experiments measured by “removing” the graphene. Both the curves measured with graphene sample are normalized with the corresponding control curves.

In the control experiment with BK7 deflector, the total internal reflection occurs at the interface of the superstrate BK7 and the substrate M1.50, $\theta_C \approx 81.75^\circ$. As shown in the red dot curve, at θ_C the absorption of monolayer graphene is measured as 42.7%, which is ~18 times stronger than the widely known absorption (~2.3%)!

This result is further confirmed by replacing the BK7 deflector with the BSG deflector and repeating the measurement, as shown in the blue dot curves in Fig. 2-3(a), where the absorption is measured as 40.5%. In this configuration, there are two total internal reflections: the first one occurs at the interface of the substrate M1.50 and BSG deflector with a critical angle $\theta_{C1} \approx 76.75^\circ$, and the second one occurs at the interface of the superstrate BK7 and the substrate M1.50 with $\theta_{C2} \approx 81.75^\circ$. Beyond θ_{C2} , the blue dot curve is in good agreement with the red dot curve, and both indicate the reflectance of the monolayer graphene in the sandwich configuration. The oscillation of the blue triangle curve between the two angles θ_{C1} and θ_{C2} is due to the substrate M1.50 functioning as a cavity between the graphene and BSG deflector.

Similarly, the $R-\theta_1$ relation at different wavelengths is measured. Figure 2-3(b) shows the results for the measurement at $\lambda=1520\text{nm}$. The absorption is about 35.3% at the critical

angle. When the wavelength varies from 650nm to 1620nm, the absorption gradually decreases from 40.5% to 33.1% with the BSG deflector, and from 42.7% to 35.3% with the BK7 deflector. Thus, ultrabroad band enhanced light absorption is achieved. The variation of the absorption with the wavelength can be attributed to the dispersion of the superstrate BK7 and substrate M1.50. In particular, the absorption becomes more sensitive when n_1 and n_3 are close enough. When the substrate is replaced by M1.49 matching liquid, the absorption will considerably decrease, for example, dropping from 42.7% to 28% at $\lambda=650\text{nm}$.

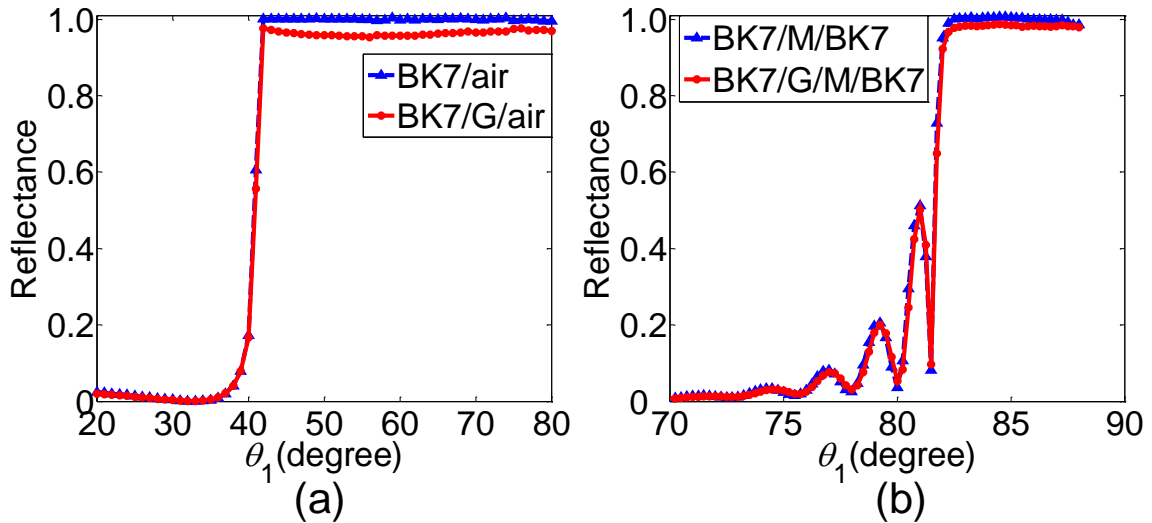


Figure 2-4. For 1520nm TM-polarized light incidence, the measured reflectance of the monolayer graphene sample as a function of incident angle when (a) the substrate is air, and (b) the substrate is M1.50.

The enhanced absorption of graphene is shown to be very sensitive to the polarization of the incident light. Similar as previous experiments, we measured the reflectance of the monolayer graphene when the substrate is air and M1.50 separately with TM-polarized incident light. As can be seen in Fig. 2-4, the maximum absorption does not occur at the

critical angle and is not sensitive to the substrate refractive index. The minimum reflectance beyond the corresponding critical angle is 97.65% (when the substrate is air) or 97.7% (when the substrate is M1.50), respectively. Therefore, the absorption in both cases is calculated as ~2.3%, which is similar to the widely known absorption coefficient.

2.2.4 Potential application in electro-optical modulation

Graphene, with its single atom thickness, exceptional electrical and optical properties, has been considered as a promising material to build integrated EO modulators which aim at a compact size, large working bandwidth as well as ultrafast modulation. The first electro-absorption modulator based on graphene has been proposed and the modulation was realized by electrically tuning the Fermi level of graphene sheet [32]. Based on our previous investigation on graphene absorption of the sandwiched structure, we further explore its potential possibility to realize EO modulation [155].

Here, we employ a similar structure like MOS but using a new material called electrolyte gel to replace the sandwiched oxide material and form simple multi-layer modulators based on graphene. Electrolyte has been used as gate insulators in organic field-effect transistors in 2005 by Nilsson et al [156]. The interface between a metal (or heavily-doped semiconductor) and electrolyte is of interest in most electrolyte applications, where two parallel layers of positive and negative charges called an electric double layer (EDL) are formed. Another advantage of using electrolyte as the gating material is, the device behavior can be conveniently controlled by varying the concentration of chemical compounds in the electrolyte [157,158]. In our experiments, a commercially available

electrolyte Redux® Gel is used to fabricate the graphene-based multi-layer modulator. Sodium chloride (NaCl) is the main chemical compound in the electrolyte gel that makes it highly conductive.

The fabrication process of the modulators is quite simple. Commercially available 1” by 1” monolayer graphene on BK7 glass samples serve as the platform. Two 100nm thick gold strips are deposited on the two sides of the sample by E-beam evaporation. They work as drain metal contact on graphene. Then a heavily doped silicon or germanium chip (resistivity as low as $0.001\text{-}0.002\Omega\cdot\text{cm}$) is tightly bonded in the center part of the sample with sticky electrolyte gel thin film in the middle, as shown in the inset of Fig 2-5(a). The heavily doped semiconductor functions as both gate contact and light deflector.

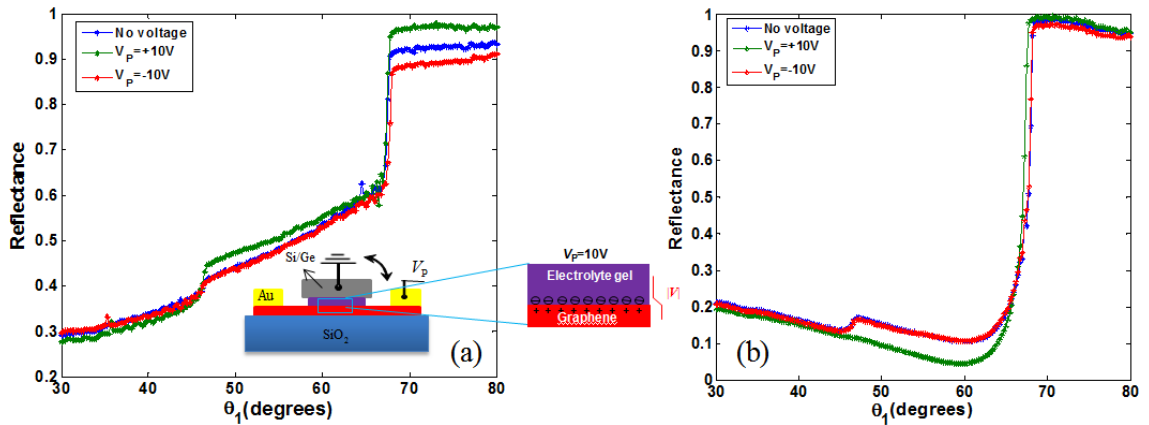


Figure 2-5. Reflectance as a function of angle for the Au/electrolyte gel/graphene on glass slide modulator with different applied voltages for (a) TE-polarized incident light; (b) TM-polarized incident light. Inset: illustration of the modulator.

Again, we use the ATR setup to test the performance of the graphene-based modulators. During the experiment, the modulators were mounted on the back of the hemicylindrical BK7 prism. To avoid a thin air gap between the prism and the modulator, a BK7 index

matching liquid is applied between them. In all the experiments, the reflectance of the modulators was measured in a sequence of: (1) without externally applied voltage, (2) with an externally applied voltage V_P , and (3) with an externally applied voltage which has reversed polarity but the same magnitude. We examined both TE- and TM-polarized light. The measured reflectance of the modulator with different applied voltages, as a function of θ_1 with a TE-polarized incident light beam at $\lambda=1520\text{nm}$ are shown in Fig. 2-5(a). With an applied voltage, an EDL is formed at the interface of the electrolyte gel and graphene layer, which could either increase or decrease the surface conductivity σ_g . Thus, the refractive index of graphene is modulated which would lead to reflectance change according to Eq. (2.1). The modulation depth, $M(\theta_1)$, as a function of angle θ_1 at a given wavelength can be defined as:

$$M(\theta_1) = \frac{|R_{V_P} - R_{-V_P}|}{R_0}, \quad (2.2)$$

where R_0 is the experimentally measured reflectance without applied voltage, $|R_{V_P} - R_{-V_P}|$ is the magnitude of the difference of the two reflectances with applied voltages. From Fig. 2-5(a), for TE-polarized light, the modulation depth at a specific angle of $\theta_1=67.5^\circ$ can be calculated as $M(67.5^\circ)=22.77\%$. We attribute the modulation to the change of surface conductivity of graphene at the gel-graphene interface, which is assisted by the redistribution of the ions in electrolyte gel induced by the applied voltage. The charge distribution at the interface and electric potential (V) at a stable status with the applied voltage is schematically illustrated in Fig. 2-5.

For TM-polarized incident light, similar with enhanced absorption, the modulation effect is also trivial compared with that of TE-polarized light, as can be seen in Fig. 2-5(b).

2.3 Enhanced unpolarized light absorption by multilayer graphene

2.3.1 Background

To overcome the bandwidth limitation and fabrication complicity in previous works that contribute to strong light absorption in graphene, we have proposed a simple three-layer structure based on the ATR method, which experimentally realizes up to ~43% light absorption by monolayer graphene over a broad spectral range, from visible (650nm) to near-infrared (1620nm). Multi-layer graphene (MLG) is also under investigation for the same purpose. In our work, we suggested 93% light absorption by 5-layer graphene based on the same configuration [126]. More recently, a method utilizing graphene-based hyperbolic metamaterial has achieved perfect (100%) light absorption [159]. Unfortunately, both works are restricted to a specific incidence polarization (i.e. the former only works for TE mode and the latter is limited to TM polarization), so it is necessary to develop new approaches.

2.3.2 Numerical analysis

The structure utilized in our previous work was essentially graphene sandwiched in superstrate (BK7 glass) and substrate (index liquid with a slightly smaller index than that of superstrate) (Fig. 2-1(a)). In this work, we replaced the superstrate (n_1) and substrate (n_3) by two types of silicon, e.g. *p*-Si and *n*-Si, with n_1 being slightly larger than n_3 . This is the typical case where the superstrate is crystalline Si and the substrate is amorphous Si.

Although materials are replaced, the working mechanism is quite analogous: ATR configuration is still applied to characterize the absorption of the three-layer stacks.

In our structure, we assume $n_1=3.5$ and $n_3=3.4$ for all examined wavelengths, and multi-layer graphene with overall thickness of 10 nm is sandwiched between the superstrate and substrate. The surface conductivity of pristine graphene $\sigma_g(\omega, \mu_c, \Gamma, T)$ is a complex number depending on the light angular frequency ω , chemical potential μ_c , charged particle scattering rate Γ and temperature T , however, in a broad range of photon energies, its real part can be universally approximated as $\sigma_g = \frac{\pi e}{2h} = 6.084 \times 10^{-5} \text{S}$, where h is the Planck's constant and e represents the elementary charge [160-162]. Thus, the refractive index of graphene is a complex number and can be calculated by $n_2 = \sqrt{1 + j \frac{\sigma_g}{\epsilon_0 \omega d}}$, where ϵ_0 is the vacuum permittivity, ω is the angular frequency of the incident light, and d is the graphene thickness. In the previous research, people have found that epitaxially grown MLG exhibits consistency with monolayer graphene in characteristics such as high carrier mobility and infrared transmission [96,163,164]. Therefore, here we adopt the optical constant of monolayer graphene for calculating our MLG sandwiched structure.

We analytically calculated the reflection and transmission of the proposed structure based on the TMM described in the previous section, and numerically simulated the structure by the FDTD method with mesh size down to 0.1nm for the MLG. In the numerical simulation, we set the same parameters as in analytical calculation, and collected the reflection and transmission data. In the analysis and calculation, we spanned the working wavelength from 1000nm to 2000nm. Figure 2-6 plots the absorption of TE- and

TM-polarized light as a function of incident angle θ_1 obtained by the two methods at $\lambda_0=1000\text{nm}$ and $\lambda_0=2000\text{nm}$, respectively. As can be seen, analytical and numerical results match quite well. At $\theta_1\approx 80^\circ$, maximum absorption near 100% can be achieved for TM-polarized light at $\lambda_0=1000\text{nm}$ and it drops to about 70% at $\lambda_0=2000\text{nm}$. On the other hand, for TE polarized light, the maximum absorption (at $\theta_1\approx 76^\circ$) for the two wavelengths keeps above 80%. As a result, absorption of both polarizations of light, or unpolarized light absorption, can be greatly enhanced.

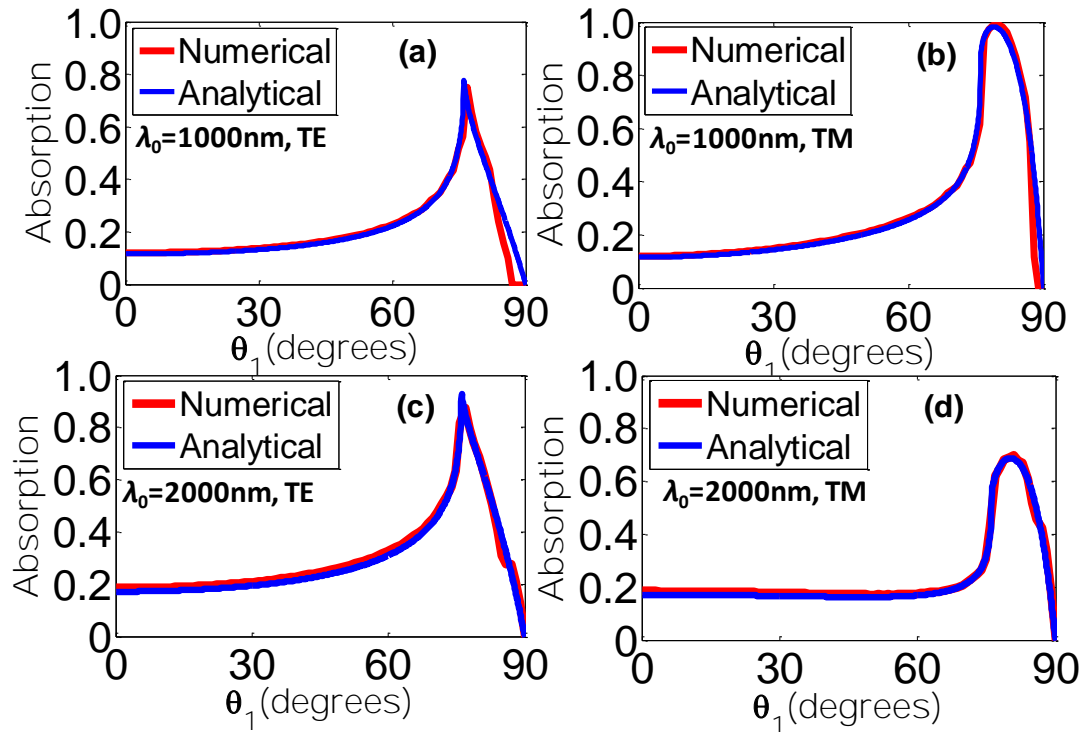


Figure 2-6. (a-d) Analytical and numerical results of absorption of TE- and TM-polarized light as a function of incident angle at $\lambda_0=1000\text{nm}$ and $\lambda_0=2000\text{nm}$.

To further investigate the absorption spectral response of the structure, we plot the maximum absorption obtained as a function of wavelength for both TM and TE polarizations, as shown in Fig. 2-7(a). According to the figure, the proposed structure (with

10-nm graphene) can absorb over 70% of incident power all the way from $\lambda_0=1000\text{nm}$ to $\lambda_0=2000\text{nm}$, regardless of the incidence polarization. Therefore, the structure has a broadband performance. Besides, here we also investigate the influence of the number of graphene layers on the absorption-spectrum response. We can see that the number of layers does not greatly affect the maximum absorption for TE polarization; however, it does make a significant difference for TM polarization at larger wavelengths: if large absorption were desired at wavelengths toward the mid-infrared regime, thicker MLG would be necessary. In addition, by comparison, absorption under TM polarization is much more sensitive to wavelength.

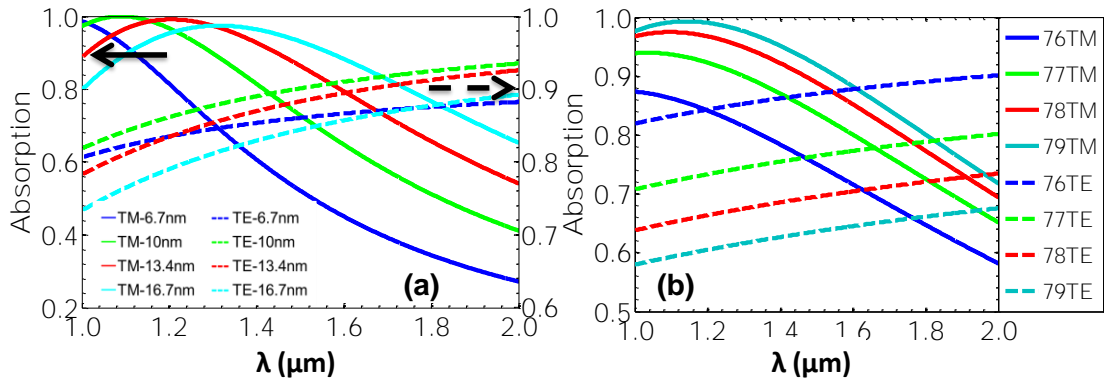


Figure 2-7. (a) Maximum light absorption as a function of wavelength for TM and TE polarization for MLG with different thicknesses. (b) Light absorption as a function of wavelength for TM and TE polarization at different incident angles.

As can be seen in Fig. 2-6, light absorption strongly depends on the incident angle. In order to illustrate what level of absorption can be achieved at a specific angle θ_1 , we plot the absorption-wavelength relation for both polarizations at $\theta_1=76^\circ$, 77° , 78° and 79° , respectively (Fig. 2-7(b)). Note that still 10-nm MLG is applied in the calculation. From the figure, over 80% unpolarized light absorption can only be achieved at $\theta_1=76^\circ$ for shorter

wavelengths ($\lambda_0 < 1280\text{nm}$). For high absorption over a large spectrum, $\theta_1 = 76^\circ$ and $\theta_1 = 77^\circ$ may be desired incident angles, at which we can see over 64% light absorption anywhere between $\lambda_0 = 1000\text{nm}$ and $\lambda_0 = 2000\text{nm}$!

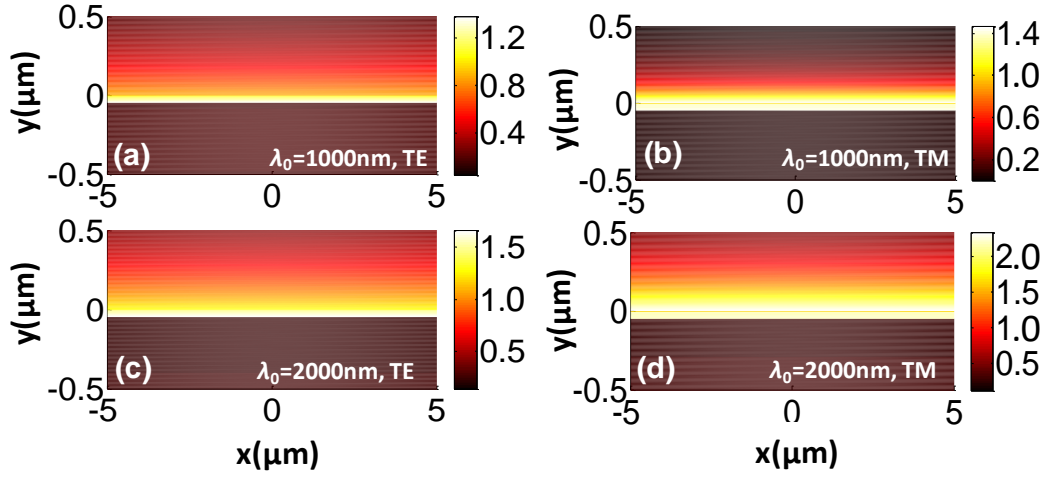


Figure 2-8. (a-d) Power distribution of the simulated structure at the incident angle where maximum absorption is achieved. MLG is located between -10nm and 0 on the y -axis.

The power density distribution of the simulated structure, when the maximum absorption is reached, is shown in Fig. 2-8, which also includes TE and TM polarizations at $\lambda_0 = 1000\text{nm}$ and $\lambda_0 = 2000\text{nm}$, respectively. From the figures, most power is confined in the MLG or its vicinity. This has further verified the enhanced light absorption.

For the proposed structure, the incident angles that allow maximum absorption to appear are near the critical angle between the superstrate and the substrate, which are quite large ($>76^\circ$). A larger index contrast between the n_1 and n_3 will make the critical angle smaller. However, this would bring a considerable absorption drop especially for TM-polarized light at longer wavelengths. For example, if the index of the substrate changes to 3.3, $\sim 55\%$ can be achieved for 2000nm TM-polarized light. On the other hand, for TE

mode or TM mode at shorter wavelengths, the maximum absorption decreases very slowly with larger index contrast.

2.3.3 Quantitative explanation

The reason why light absorption can be enhanced for both polarizations can be explained qualitatively as follows. Thirty layers of graphene counts for a total thickness of only 10 nm, which is so small that can be treated as a perturbation. In this way, the three-layer structure is approximated as a two-layer ($n_1|n_3$) structure. We know that the tangential component of electric field is continuous at the boundaries between layers. According to Fresnel's law, the electric field in graphene for TE polarization, E_2 , can be written as

$$E_2 = tE_i = \frac{2n_1 \cos\theta_1 E_i}{n_1 \cos\theta_1 + n_3 \cos\theta_3} \quad (2.3)$$

where E_i is the electric field of the incident light wave. The power dissipation density in graphene can be calculated by $p_d = \frac{1}{2} \sigma_g |E_2|^2$, and maximum $|E_2|$ results in maximum p_d , or maximum absorption. From Eq. (2.3), when $\cos\theta_3=0$ or equivalently $\theta_1=\theta_c$, $|E_2|$ reaches its maximum, $2|E_i|$. This also explains why enhanced light absorption is achieved for TE polarization in the sandwiched monolayer graphene structure in Section 2.2.

Unlike the case in TE polarization that electric field only has tangential component; for TM polarization, the electric field in graphene E_2 also includes normal component, thus can be approximated as

$$E_2 = \sqrt{|E_{2t}|^2 + |E_{2n}|^2} \approx \left| \frac{2n_1 \cos\theta_1 E_i}{n_1 \cos\theta_3 + n_3 \cos\theta_1} \right| \sqrt{\left(|\cos\theta_3|^2 + \left| \left(\frac{n_3}{n_2} \right)^2 \sin\theta_3 \right|^2 \right)} \quad (2.4)$$

Note that the tangential component of electric field, E_{2t} , is continuous at boundaries, and the normal component, E_{2n} , is proportional to the dielectric constant of the substrate. If n_3 is too small, for example, $n_3=1.5$, as the case in the previous section, the value of $E_{2n} \propto \left(\frac{n_3}{n_2}\right)^2 \sin \theta_3$ would also be quite small. As a result, the sandwiched monolayer graphene structure is very sensitive to the polarization of incident light. In the structure discussed in this section, however, the maximum electric field $|E_2|$ is still found at the critical angle between the substrate and superstrate because the refractive index n_3 and hence E_{2n} are very large. Therefore, the electric field in the sandwiched graphene can be simultaneously enhanced for both TE and TM polarization.

2.3.4 Potential application in photovoltaics

We have demonstrated at least 70% of unpolarized incident light in a broad band absorbed by MLG. Furthermore, if the superstrate and substrate were transparent to shorter or longer wavelengths, similar level of enhanced absorption would be achieved in the whole visible and NIR regimes (400nm-3000nm), covering nearly the whole solar spectrum! We will discuss the potential application of the graphene-sandwiched silicon structure in solar cells. Different from most previous works [165,166], the graphene, in this case, acts as a photoactive material instead of transparent electrodes. The performances of photodiodes intended for photovoltaic application depend on its optical absorption process, carrier transport, and interaction with external circuit systems. A photovoltaic cell absorbs the incident photons, and consequently, electron-hole pairs are generated. Silicon-based materials, owing to their compatibility in semiconductor fabrication technologies,

dominate current photovoltaic technology. One drawback of silicon or other semiconductor solar cells is the absorption restricted by the material bandgap E_g : if photon energy, $h\nu < E_g$, no absorption occurs; if photon energy, $h\nu > E_g$, absorption occurs, but the excess energy, $h\nu - E_g$, dissipates. Due to the unique band structure of graphene, the absorption of a photon with any wavelength can potentially create an electron-hole pair. However, the drawback of graphene lies in no bandgap and ultra-fast intraband carrier relaxation.

Carrier relaxation dynamics inside graphene include several routes, namely carrier-carrier scattering, and phonon emission [167]. In conventional semiconductor structures, energy and momentum conservation need to be satisfied to generate electron-hole pairs. In contrast, graphene can generate multiple excitons upon illumination of a single photon. As described in Ref. [168], the critical step to increasing the solar cell efficiency is the recombination of charge carriers, which occurs via both Auger recombination and impact ionization processes. In Auger recombination process, an electron is scattered from the conduction band into the valence band, while at the same time, the energy is transferred to another electron, which is excited to higher energy level in the conduction band. The reverse of this phenomenon occurs via impact ionization. On the other hand, an electron intraband relaxation in the conduction band is associated with the excitation of a valence band electron into the conduction band [168]. Both processes also occur for holes in an analogous way. For the photovoltaic application, a key issue will be how to extract the photon-excited electron-hole pairs before they relax within $\tau \approx 0.30\text{ps}$ [169].

2.4 Conclusions

In this chapter, we have experimentally demonstrated that the absorption of monolayer graphene can be significantly enhanced over a broad spectral range, from visible to infrared, when the incident light is TE-polarized. At the critical angle, the absorption is in the range of 7.6%-11.2%, when the substrate is air, and up to 42.7%, when the substrate is replaced by a medium with a closer refractive index compared to that of the superstrate. The enhanced absorption is not strongly dependent on the wavelength but very sensitive to the polarization of incoming light. We have also demonstrated preliminary results of EO modulation by applying electrolyte gel in the graphene-based multilayer structure. These results may lead to potential development of next generation optoelectronic components. Furthermore, we have solved the problem of polarization dependence by introducing an MLG-sandwiched silicon structure. For 10-nm thick MLG, analytical calculation and numerical simulation both show absorption over 80% (for TE) and 70% (for TM) at any wavelength between $\lambda_0=1000\text{nm}$ and $\lambda_0=2000\text{nm}$. Besides, we have discussed the potential of the structure as photovoltaic device. Detailed calculation and analysis of an MLG *p-n* junction model are given in Ref. [127], where we have shown that electric current can be extracted much faster than carrier recombination.

3. ENZ-SLOT WAVEGUIDE BASED ON CONDUCTIVE OXIDE

Starting from this chapter, I will present a detailed investigation on another promising active material for enhanced light absorption as well as EO modulation, conductive oxide (COx). The investigation starts from preliminary numerical analysis of an ENZ-slot waveguide structure, which demonstrates great field enhancement and power confinement within the ENZ slot. By applying COx as the slot material, considerable light absorption can be achieved for the waveguide at ENZ state. Switching between ENZ state and Epsilon-far-from-zero (EFFZ) state by external electric signal would lead to modulation of optical absorption, which promises future nanoscale EA modulators. Besides, the significant shift of effective index of the COx-based ENZ-slot waveguide between ENZ and EFFZ state can find applications in laser beam steering.

3.1 Background

The development of metamaterials enables material permittivity to be engineered to almost any arbitrary value. Particularly, some recent research has been focused on the epsilon-near-zero (ENZ, or index-near-zero) material, which has a dielectric constant (or refractive index) with small magnitude in a frequency range of interest. Novel applications of ENZ materials have been investigated, such as tunneling and squeezing electromagnetic energy through subwavelength narrow channels [170,171], design of matched zero-index materials [172,173], and shaping the radiation pattern of a source [174,175].

The optical dielectric constant of a material is determined by its free carrier concentration, and the effect of free carriers on an optical material can be approximated by the Drude model, which was proposed in 1900 [176,177]. There are two main solid state systems that exhibit strong free electron effects: metals and doped semiconductor. Both can be treated as plasma, which is a neutral gas of heavy ions and light electrons. Considering the oscillations of a free electron induced by the AC electric field $E(t)$ of an electromagnetic wave, the equation of motion for the displacement x of the electron is

$$m_0 \frac{d^2x}{dt^2} + m_0\gamma \frac{dx}{dt} = -eE(t) = -eE_0 e^{-i\omega t} \quad (3.1)$$

where ω is the frequency of the light with an amplitude of E_0 . γ is the damping coefficient of free carriers. The acceleration of the electron is represented by the first term, while the second is the frictional damping force of the material. The term on the right-hand side is the driving force exerted by the light.

By substituting $x = x_0 e^{i\omega t}$ into Eq. (3.1), we obtain

$$x(t) = \frac{eE(t)}{m_0(\omega^2 + i\gamma\omega)}. \quad (3.2)$$

The polarization P of the gas is equal to $-Nex$, where N is the number of electron per unit volume. Recalling the electric displacement field D , which is defined as

$$D = \epsilon_0 E - \frac{Ne^2 E}{m_0(\omega^2 + i\gamma\omega)} \quad (3.3)$$

Hence, we get

$$\epsilon_r(\omega) = 1 - \frac{Ne^2}{\epsilon_0 m_0} \frac{1}{(\omega^2 + i\gamma\omega)} \quad (3.4)$$

Eq. (3.4) can be written more concisely as

$$\varepsilon_r(\omega) = 1 - \frac{\omega_p^2}{(\omega^2 + i\gamma\omega)} \quad (3.5)$$

where the plasma frequency, ω_p , is defined as

$$\omega_p = \sqrt{\frac{Ne^2}{\varepsilon_0 m_0}} \quad (3.6)$$

where e is the unit electric charge, ε_0 the free space permittivity, and m_0 the electron mass. The plasma frequency ω_p corresponds to the natural resonant frequency of the free carrier gas.

The free electron model presented above can be applied to doped semiconductors with two appropriate modifications [178]. Firstly, the fact that the electrons and holes are moving in the conduction or valence band of a semiconductor needs to be considered. In this scenario, we can assume that those carriers behave as particles with an effective mass m^* rather than the free electron mass m_0 . Secondly, there are other mechanisms that may contribute to the dielectric constant as well as the free carrier effects. The main extra part is the contribution to the polarization due to the optical response of the bound electrons. Therefore, Eq. (3.3) can be rewritten in the following form when the two modifications are considered,

$$D = \varepsilon_\infty \varepsilon_0 E - \frac{Ne^2 E}{m^*(\omega^2 + i\gamma\omega)} \quad (3.7)$$

The effective mass m^* accounts for the band structure of the semiconductor, ε_∞ is the high frequency dielectric constant, and carrier density N in this equation is the density of free

electrons or holes generated by the doping process. From Eq. (3.7) we can write the frequency dependence of the dielectric constant as

$$\varepsilon = \varepsilon' + j\varepsilon'' = \varepsilon_{\infty} \left[1 - \frac{\omega_p^2}{(\omega^2 + i\gamma\omega)} \right] \quad (3.8)$$

where the plasma frequency is updated as

$$\omega_p = \sqrt{\frac{Ne^2}{\varepsilon_{\infty}\varepsilon_0 m^*}} \quad (3.9)$$

which is determined by free carrier concentration and effective mass.

From this chapter, Eq. (3.8) will be used to model the optical properties of COx, where COx is treated as heavily doped semiconductor.

3.2 ENZ material and slot waveguide

According to the Drude model, when $\omega \approx \omega_p$, the ENZ effect of a material would show up. With abundant free carriers ($N \sim 10^{22} \text{cm}^{-3}$), metals have such high plasma frequencies that they exhibit large negative real dielectric constant in the NIR range. Most semiconductors have doping limitations that result in their plasma frequencies located beyond MIR. The moderate carrier concentrations in COx ($10^{19} - 10^{21} \text{cm}^{-3}$), together with advantages of low intrinsic loss, tunable optical properties, as well as easy fabrication and integration, have made them excellent plasmonic materials in the NIR regime [73,179]. Several other ENZ metamaterials have also been reported [180-182].

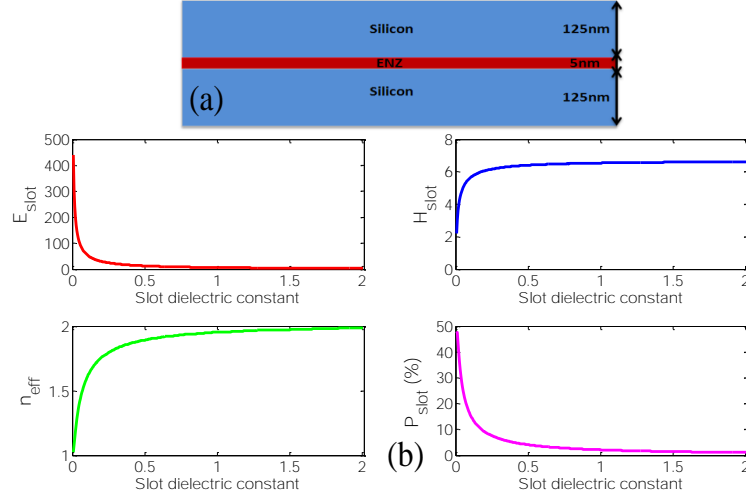


Figure 3-1. (a) Structure of a simple three-layer waveguide. (Value of n_{silicon} used for $\lambda_0 = 1550 \text{ nm}$ is 3.47). (b) Plots of the electric field, magnetic field, power percentage in the slot and effective index of the structure versus slot dielectric constant [183].

In our recent work, we studied a structure combining ENZ material with slot waveguide, namely ENZ-slot waveguide, and found some unprecedented properties. A slot waveguide [184,185] consists of a narrow low refractive index “slot” sandwiched at the center of a single mode high-index waveguide, which can greatly confine light and enhance optical fields in the slot region. The slot waveguide only works well for transverse magnetic (TM) mode where the magnetic field is parallel to the slabs. When the free carrier effect is considered in complex dielectric constants, the continuity of electric flux density between two media holds, i.e., $\epsilon_1 E_{1n} = \epsilon_2 E_{2n}$ or $E_{1n} = (\epsilon_2/\epsilon_1)E_{2n}$. If ENZ material is applied as the slot, enormous enhancement of E-field will take place and more power can be confined in the ENZ-slot.

As a simple example showing field enhancement and power confinement of ENZ-slot waveguide, the structure shown in Fig. 3-1(a) is analytically examined. Fig. 3-2(b) plots

the electromagnetic field intensity, power percentage in the slot and effective index of the structure as a function of slot dielectric constant ϵ_{slot} . We can see the dramatic change of these terms when ϵ_{slot} is approaching zero. In particular, the effective index sharply decreases from 1.6 to nearly 1 when ϵ_{slot} decreases from 0.1 to nearly zero due to larger power confinement within the low index slot.

3.3 Nanoscale EA modulators based on COx-slot waveguide

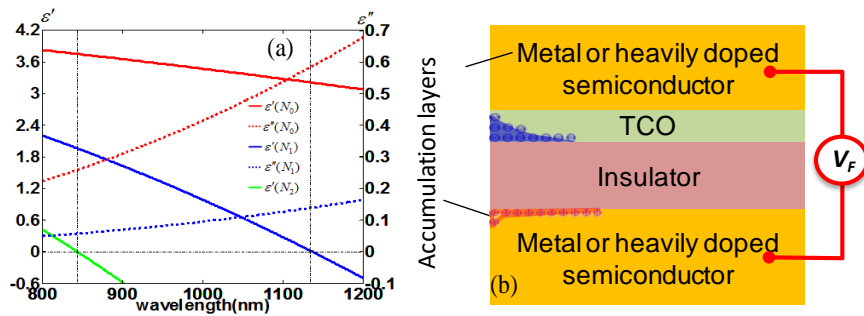


Figure 3-2. (a) Real part of the dielectric constant of ITO as a function of wavelength at three different carrier concentration based on the Drude model [186]. (b) Illustration of the ENZ-slot waveguide [187].

According to the experimental data in Ref. [33], ITO with different carrier concentrations could work as ENZ material at specific wavelengths. As shown in Fig. 3-2(a), ENZ effect of ITO is achieved at $\lambda_0 = 1136 \text{ nm}$ and $\lambda_0 = 843 \text{ nm}$ under carrier concentrations $N_1 = 1.65 \times 10^{22} \text{ cm}^{-3}$ and $N_2 = 2.77 \times 10^{22} \text{ cm}^{-3}$, respectively. As suggested, the accumulation of carriers can be realized by electric signal in a MOS-like structure (Fig. 3-2(b)), which indicates the optical tunability of ITO.

Table 3.1. Dielectric constant of ITO at untuned and ENZ state

Wavelength	ϵ_0	ϵ_{ENZ}
1136nm	$3.0274 + j0.586$	$-0.0014 + j0.1395$
843nm	$3.7541 + j0.2579$	0.0045

The dielectric constant of ITO at epsilon-far-from-zero (EFFZ, or untuned) state and ENZ state is shown in Table 3.1, where we can see the magnitude has changed tens or even hundreds of times due to externally applied voltage. The huge change in the magnitude of dielectric constant may find applications in EA modulators. For lossy medium, the dielectric constant can be formulated as $\epsilon_{ITO} = \epsilon' + \epsilon''$, where $\epsilon'' = \frac{\sigma}{\omega\epsilon_0}$. The power dissipation density can be written as

$$p_d = \frac{1}{2}\sigma E^2 \propto \frac{1}{2}\epsilon'' E^2 \propto \frac{1}{2}\epsilon''/|\epsilon|^2, \quad (3.10)$$

which can be greatly enhanced when $|\epsilon| \rightarrow 0$. Fig. 4-2(b) depicts typical EA modulator configurations based on COx-slot waveguide. The modulator would be off with low-absorption at EFFZ state and on with high-absorption at ENZ state, due to the change of dielectric constant. Note that the working wavelength chosen for the EA modulators is $\lambda_0 = 1136$ nm.

ITO EA modulators based on a dielectric waveguide (Fig. 3-3(a)) and a plasmonic waveguide (Fig. 3-3(b)) were proposed and simulated. Their modes were solved by FDTD method. Note that we applied 10nm thick ITO in the waveguides, of which 5nm at ITO-SiO₂ interface was assumed to be tuned. From the results, we can see significant field enhancement and confinement within the ENZ-slot and considerable shift in effective index. More importantly, a huge change in waveguide attenuation (21.85dB/ μ m for dielectric waveguide, and 20.64dB/ μ m for plasmonic waveguide) is achieved.

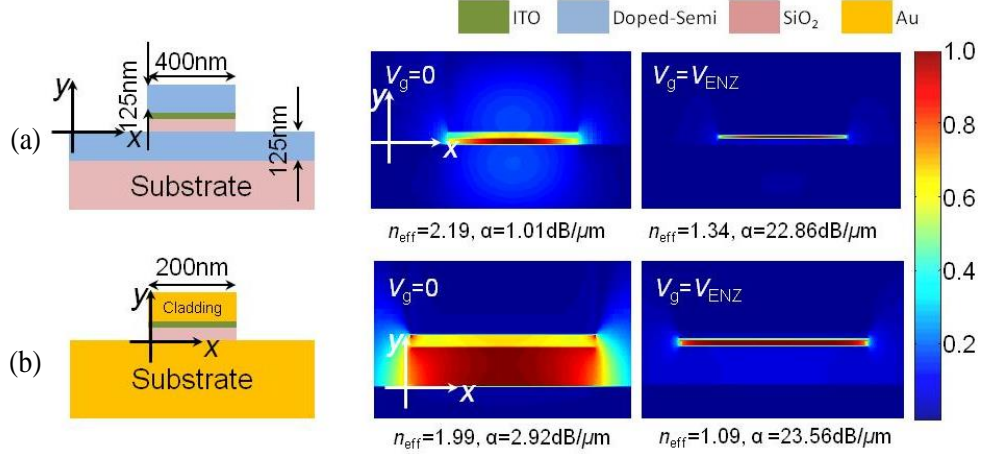


Figure 3-3. The electric field profiles, effective indices and propagation loss for different ITO-slot waveguide at untuned state and ENZ state, respectively: (a) in a dielectric rib waveguide; (b) in a plasmonic waveguide [183].

The insertion loss of the EA modulators was evaluated by 3D FDTD simulation. For a 150nm long modulator embedded in a plasmonic rib waveguide, the insertion loss is 0.48dB and the modulation depth is 3.42dB, which is very close to the one predicted by 3D mode solver. A 200nm long modulator embedded in a dielectric rib waveguide shows an insertion loss of 0.56dB, and a modulation depth of 3.53dB.

In Ref. [187], we utilized similar theory and demonstrated EA modulation based on ENZ-slot waveguide where another COx material, AZO, is serving as the tunable slot. We also showed the optical bandwidth of these modulators could be over several THz due to slow Drude dispersion. These COx-slot waveguide based EA modulators are compact, and could potentially work at ultra-high speed, being mainly limited by the RC delay introduced by electric circuits.

3.4 Laser beam steering by CO_x-slot waveguide

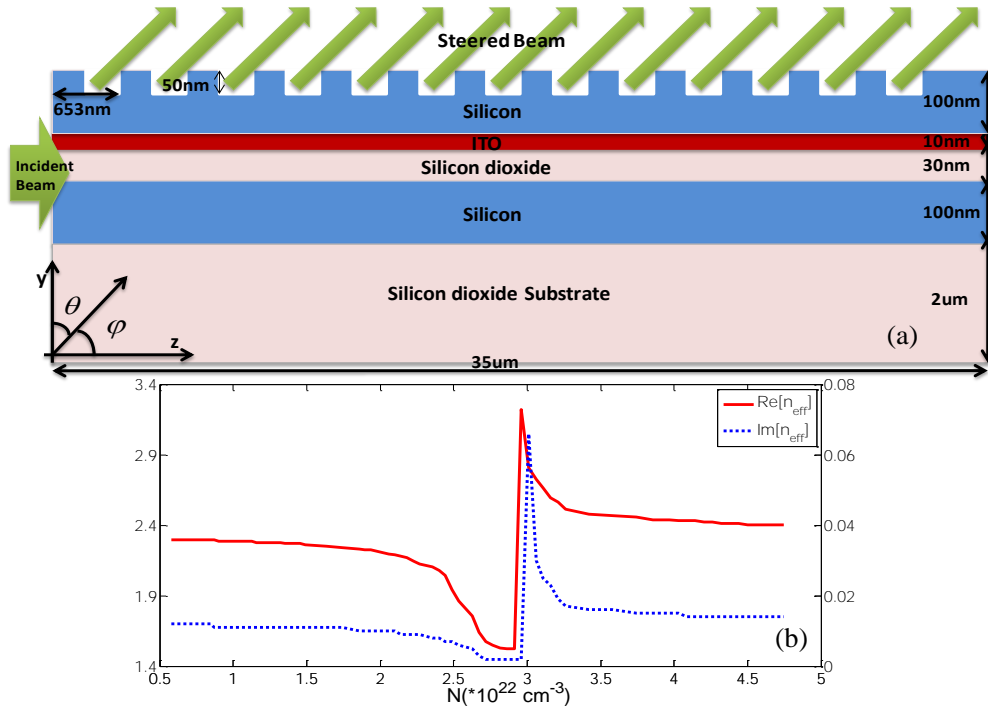


Figure 3-4. (a) Illustration of beam steering based on ENZ-slot waveguide with periodic gratings. (b) Complex effective index in terms of carrier concentration.

In both the analytical calculation of simple ENZ-slot waveguide and the numerical simulation of the EA modulators in previous sections, we see that the effective indices of the waveguides undergo considerable change. Thus, we can engineer the effective index of the ENZ-slot waveguide by tuning the refractive index of ITO film. This phenomenon may find applications in laser beam steering. Laser beam steering techniques are being widely investigated because of their applications in laser-based sensing, communication and power projection and other fields. Mechanical and non-mechanical methods such as beam steering with rotating (Risley) prism, macro-optical mirrors, micro-lens arrays, liquid crystal polarization gratings have been proposed [188-190], heading to the purposes of

compactness, low power, high speed, lightweight and large field of regard. To advance this technique, we propose a novel beam steering structure based on the tunable ENZ-slot waveguide.

In order to realize beam steering, we added periodic gratings on top of the ITO-slot waveguide (Fig. 3-4(a)) and made use of the tunable effective index of the structure to steer the incident laser beam. According to the grating equation

$$k_0 \sin\theta + \frac{2\pi l}{\Lambda} = k_0 n_{\text{eff}} \Leftrightarrow \sin\theta + l\lambda_0/\Lambda = n_{\text{eff}} \quad (3.11)$$

where λ_0 is the wavelength of the incident beam, $k_0 = 2\pi/\lambda_0$ is the wave number. Λ is the period of the gratings, $l = \{\pm 1, \pm 2, \dots\}$ is an integer representing the propagating mode of interest, n_{eff} is the effective index of the waveguide, θ is the steering angle. Given fixed grating period and wavelength, the incident beam can be steered by tuning the effective index, which, as discussed above, is able to be realized by electrically tuning the optical property of ITO.

For an incident beam of $\lambda_0 = 1136$ nm, the attenuation would be too large for the waveguide when ITO is at ENZ state. Since long distance propagation is a major concern here in order for easy detection. We chose the working wavelength to be 843nm, which is the cross wavelength for ITO under N_2 . Here the damping factor $\gamma \approx 0$ [33], so the attenuation of the ENZ-slot waveguide decreases quite a bit: $\alpha_0 = 0.328\text{dB}/\mu\text{m}$ when untuned and $\alpha_2 = 0.107\text{dB}/\mu\text{m}$ under N_2 . Besides, effective index is also significantly shifted from 2.29 to 1.65, which promises a wide steering angle.

For convenience, in Eq. (3.11), we assume $\Lambda = 653$ nm, $\lambda_0 = 843$ nm and $l = 1$, which make $l\lambda_0/\Lambda = 1.29$. Fig. 3-4(b) plots the complex effective index of the waveguide

in terms of the carrier concentration. The effective index that can be obtained ranges from 1.53 to 3.22 (values larger than 2.29 may correspond to a higher harmonic mode). Therefore, the value range for $\sin\theta$ that can be achieved is from 0.24 to 1, which results in the steering angle θ from 14° to 90° . Note that the minimum effective index is achieved when active ITO layer (5nm) at ITO-SiO₂ interface is at ENZ state.

FDTD simulations were performed to verify the predictions. The phase plot, normalized intensity magnitude plot and far-field intensity plot of the dominant electric field E_y for the steering angles of 14° and 60° are shown in Fig. 3-5.

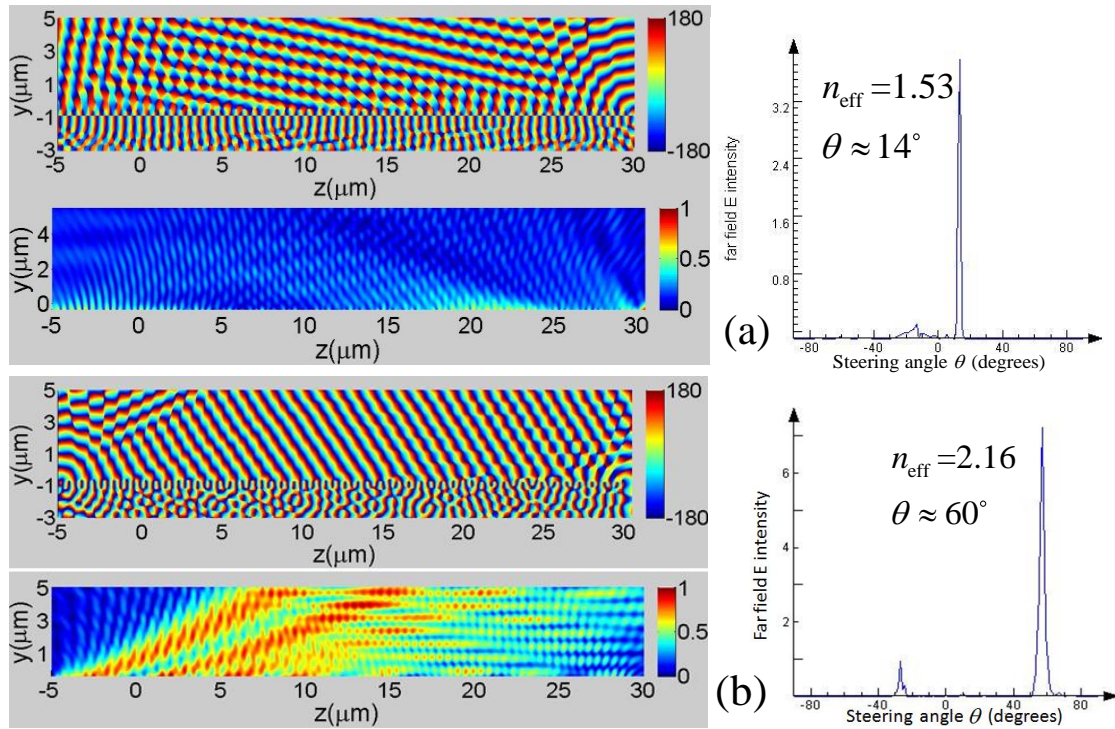


Figure 3-5. Phase, normalized magnitude and far-field intensity of E_y for steering angles of (a) 14° and (b) 60° [183].

The phase and magnitude plots illustrate the propagation direction of the steered beam in the near-field, which is normal to the phase line, or along with the magnitude trend. Note

that the magnitude plots only show the electric field above the ENZ-slot due to a much higher electric field in the slot. Far-field intensity plots can clearly identify the steering angle. According to the figures, laser beam steering is achieved by the effective index change of the ENZ-slot waveguide. The maximum steering angle we got from simulation is $\theta \approx 75^\circ$.

As one example, we showed some theoretical study of COx behaving as ENZ material in ENZ-slot waveguides and their applications in EA modulation and laser beam steering. ENZ-slot waveguides highly confine electromagnetic fields in the slot region, so the behaviors of the waveguides can be greatly changed by tuning the slot material. Besides, they can be easily fabricated layer by layer. With the advantages of COx in low intrinsic loss, excellent tunability as well as ease of fabrication and integration, the combination, COx-slot waveguides, is of great promise in building novel optoelectronic devices for NIR applications.

3.5 Conclusions

In this chapter, the investigation shows the potential applications COx as ENZ materials. For the ENZ-slot waveguide structure, the light absorption may be greatly enhanced within a very thin slot at a certain wavelength. Moreover, the effective index of the waveguide can be shifted by providing different carrier concentrations. Based on COx, which nearly have all the properties that a novel plasmonic material requires, especially for NIR applications, we introduced some waveguiding structures and revealed their potentials to realize EA modulators with compactness, ultra-high speed, and easy fabrication.

Another application of COx-based ENZ-slot waveguide in laser beam steering was also presented. A maximum steering angle of 61° may be achieved. This structure enables beam steering device made in micro-scale or even nano-scale. Although only preliminary results are provided here, we look forward to the successful development of such techniques which may lead to significant breakthroughs in on-chip optical interconnects. In the next chapter, I will present our experimental investigation on EO modulators based on COx-slot waveguide.

4. FIELD-EFFECT EA MODULATORS BASED ON CONDUCTIVE OXIDE

In Chapter 3, EA modulation based on CO_x realized by ENZ-slot waveguide is theoretically studied. In the numerical analysis, ITO parameters from other group [33] are used to model the attenuation of the waveguide at ENZ or EFFZ state in the NIR regime. A voltage-induced accumulation layer formed at ITO-insulator interface is the key to achieve EA modulation. The results show great potential for future nanoscale EO modulators. In this chapter, I will present our experimental study of a MOS-like, or more specifically, a metal-insulator-CO_x (MIC) structure [191-193]. The structure roughly works as a parallel capacitor and exhibits field effect when a bias voltage is applied across the insulating layer. The experiment reveals that both carrier depletion and accumulation will contribute to EA modulation. The ENZ effect of active material, ITO, is observed [182].

4.1 Background

Compared to the *p-n* or *p-i-n* structures in silicon-based modulators, optical modulators may be also realized based on the MOS structure, which roughly functions as a parallel capacitor. When a bias voltage is applied across the oxide layer, charges are induced at metal and semiconductor surfaces. The field-induced charge per unit area in the MOS capacitor can be calculated according to

$$Q_s = \epsilon E \approx \epsilon \left(\frac{V}{d} \right) \quad (4.1)$$

where ε is the DC or RF permittivity of the insulator, and E is the applied electric field across the insulator layer with thickness d . According to the bias polarity and strength, a MOS structure may work in three well-known modes: accumulation, depletion, and inversion, as shown in Fig. 4-1. Generally speaking, accumulation induces more majority carriers, and the accumulation layer becomes more electrically conductive and more optically absorptive, whereas depletion removes free carriers, and the optical absorption by free carrier in the depletion layer can reduce to a negligible level. The inversion between electron and holes requires slow thermal excitation; thus, inversion is insignificant for high-speed optical modulation. The accumulation layer thickness can be estimated as

$$l_{ac} \approx \pi L_D / \sqrt{2}, \quad (4.2)$$

where L_D is the Debye length of the semiconductor. The depletion layer thickness can be estimated by

$$w_d = \frac{Q_s}{eN_0} \quad (4.3)$$

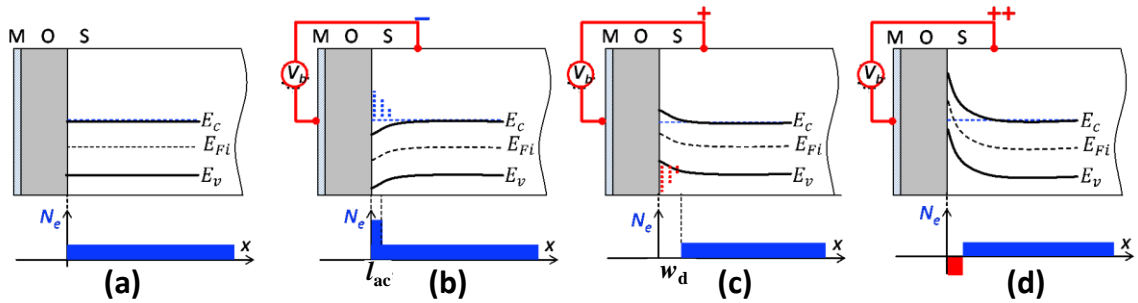


Figure 4-1. Operation of field effect in MOS capacitor. (a) Flat band. (b) Accumulation. (c) Depletion. (d) Inversion.

Dionne, *et al.* demonstrated a field effect optical modulator (FEOM) based on crystalline silicon sandwiched into two silver films [20], where the modulating electric field can switch the waveguide between guiding and cut-off states. Feigenbaum *et al.* investigated an FEOM based on conductive oxide (COx) [33], which is the first experimental demonstration of COx as active material for optical modulation. In particular, unity-order refractive index change in the COx accumulation layer was measured based on the ellipsometry method. Many works have followed this work, including numerical studies reported in Refs. [187,194-198]. Experimental demonstrations of COx as the active material for EA/EO modulation are also reported [83,191,199]. Modulation extinction ratio is reported as 1 dB/ μm in Ref. [83], and 2.71 dB/ μm in Ref. [199].

We are interested in EA modulation based on ENZ materials. We noticed that ENZ could be achieved in graphene [67] and COx [200] for NIR applications. As demonstrated in the last chapter, when a thin ENZ film is sandwiched in a single mode dielectric or plasmonic waveguide (ENZ-slot waveguide), very strong electric field can be excited in the ENZ film for the transverse magnetic (TM) mode. The greatly enhanced electric field leads to greatly enhanced light absorption. To experimentally achieve ENZ and EA modulation, we investigate EO modulators based on a MOS-like MIC structure.

4.2 Structure and fabrication

We fabricated an ITO/HfO₂/Al concentric structure on the quartz substrate as shown in Fig. 4-2(a,b). HfO₂ is known for its high DC/RF dielectric constant. It also has high dielectric strength so that a thin insulating layer could withstand a large electric field

without breaking down. As a result, HfO_2 may be used to enhance the field effect in the device. Aluminum is chosen here for its excellent conductivity, low absorption in the NIR regime, as well as low cost. Another advantage of using aluminum layer is that light absorption can be directly measured by $1-R$ (R is the power reflectance) with ATR setup.

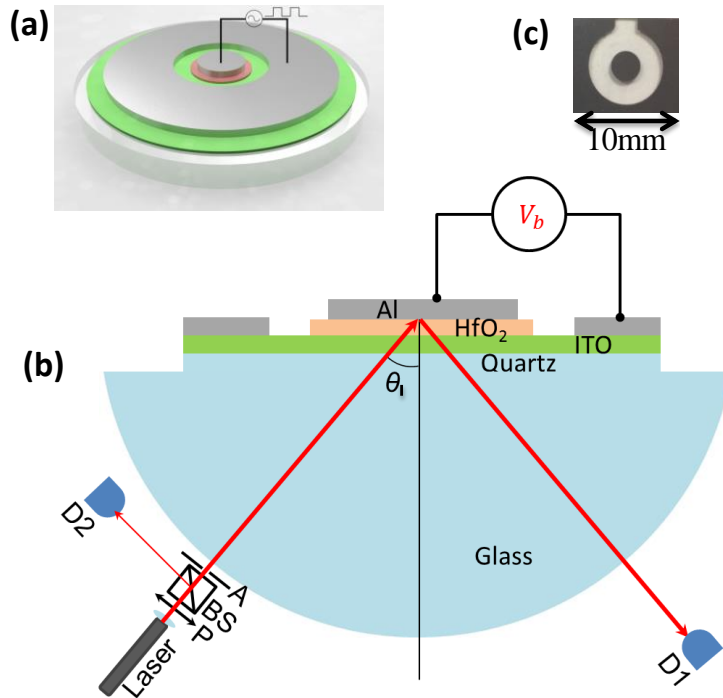


Figure 4-2. (a) Schematic of the MIC EO modulator. (b) Illustration of the setup for ATR measurement. (c) Picture of the fabricated device.

The fabrication of the modulators starts from ITO film deposition on transparent glass, by CVC601 at SMFL (see Section 1.4.2). The thickness of ITO film is measured in the range of 10~12nm with a 5-minute deposition time. After 4-hour post annealing process, the sheet resistance of ITO film is measured around $400\sim 600\Omega/\square$. After that, 50nm thick HfO_2 is deposited on ITO layer by atomic layer deposition (ALD). Finally, a 200nm thick layer of aluminum is deposited on top by E-beam evaporation. General photolithography

and lift-off process are applied to define the pattern of HfO₂ and Al, where AZ® nLOF 2020 negative photoresist and Shipley 1165 remover are used, respectively. The picture of the fabricated sample is shown in Fig. 4-2(c). We made the samples very large in order to easily focus our light sources on the multi-layers. Theoretically, the modulator can be made within micro-scale.

4.3 Broadband bias-polarity-dependent modulation effect

In the experiments, the sample is tested by the ATR setup (Fig. 4-2(b)) in a similar manner with the graphene-sandwiched structure (see Section 2.2.3). The polarizer (P) is set to choose TM polarization for all measurements. We first measured the reflectance of ITO modulator as a function of incident angle θ_1 at different wavelengths ranging from $\lambda_0=1260\text{nm}\sim 1620\text{nm}$ without externally applied voltage. The measured reflectance is then numerically fitted by calculating the reflectance through the multilayer structure based on the TMM. The fitting parameters of the dielectric constant of ITO are further fitted based on the Drude model. The fitting parameters are $\varepsilon_\infty=4.4$, $\omega_p=2.51\times 10^{15}\text{rad/s}$, and $\gamma=1\times 10^{15}\text{rad/s}$. The corresponding carrier concentration is $N_0=3.05\times 10^{21}\text{cm}^{-3}$. As a non-stoichiometric compound, the optical properties of ITO largely depend on the deposition processes and post-annealing conditions. The ε_∞ is slightly different from those obtained in other groups [33,77,82] due to the non-identical fabrication conditions.

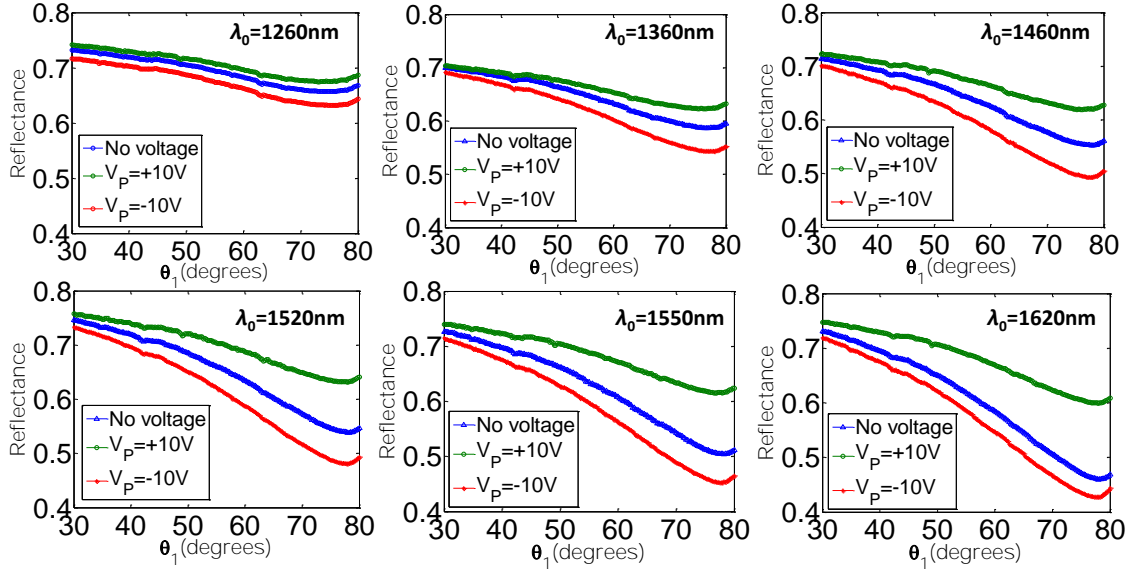


Figure 4-3. Reflectance as a function of incident angle for the modulator under different applied voltages for different wavelengths.

After that, an external voltage was applied. During the experiment, we found that the reflectance (or 1-absorption) of the modulator λ could either be increased or decreased by applying positive or negative voltage, respectively. We conducted measurements with an externally applied voltage of different polarities but the same magnitude $\pm V_P$. For different wavelengths, the measured reflectance of the modulator with different applied voltages, as a function of θ_1 with a TM-polarized incident light beam is shown in Fig. 4-3, respectively. According to Eqs. (4.2 & 4.3), the thickness of accumulation layer formed at ITO-HfO₂ interface is estimated to be 0.144 nm, while the depletion layer thickness is 0.453 nm. The modulation depth, $M(\theta_1)$, as a function of angle θ_1 at a given wavelength can be defined as: $M(\theta_1) = |R_{+V_P} - R_{-V_P}|/R_0$, where R_0 is the experimentally measured reflectance without applied voltage; $|R_{+V_P} - R_{-V_P}|$ is the magnitude of the difference of the reflectance under applied voltages.

From Fig. 4-3, broadband EO modulation has been achieved and the largest modulation depth obtained at a specific angle, $\theta_1=78^\circ$, is $M_{\max}(78^\circ)=37.42\%$ for $\lambda_0=1620\text{nm}$. We call the angle where the maximum modulation depth is achieved, the modulation angle. We attribute the modulation mainly to the change of the free carrier concentration in the voltage induced active layer in ITO at the interface. In detail, when negative bias is applied, excess carriers will be accumulated at the ITO-HfO₂ interface, which results in a more absorptive active ITO layer; on the contrary, the free carriers in the active layer will be depleted under positive bias and the modulator becomes less absorptive.

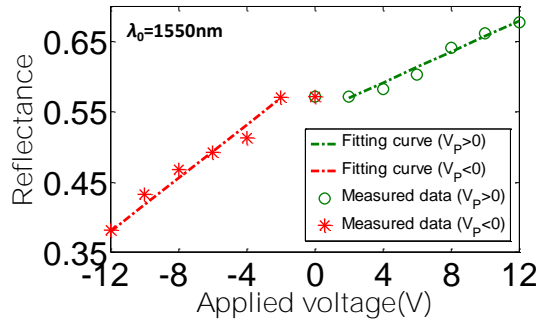


Figure 4-4. Power reflectance as a function of applied voltage at the modulation angle for $\lambda_0=1550\text{nm}$.

Besides, we examined the variation of modulation depth with regard to applied voltages of different magnitude. Starting from 0V, we measured the power reflectance at the modulation angle at a $\pm 2\text{V}$ step. The measured results for $\lambda_0=1550\text{nm}$ are shown in Fig. 4-4. From the figure, when $\pm 2\text{V}$ voltages are applied, nearly no modulation can be observed, which indicates that there may exist a threshold voltage for the modulator to start working. After that, modulation depth and applied voltage almost follow a linear relation. It is true that the higher voltage we apply, the larger modulation depth we can achieve; however,

higher voltages may induce large current and heat which would burn or break down the sample. The voltage limit may vary due to different sheet resistances of the samples.

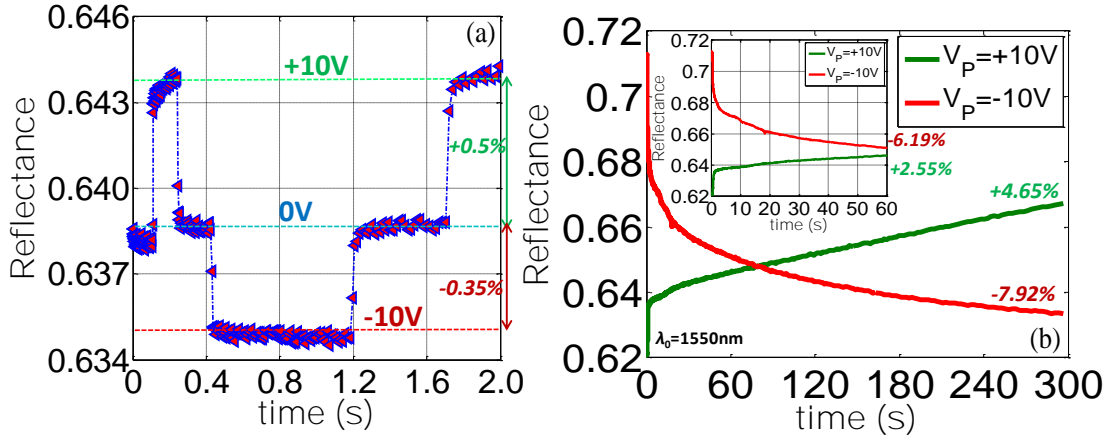


Figure 4-5. Power reflectance as a function of time at the modulation angle for $\lambda_0=1550\text{nm}$. (a) Fast modulation; (b) Slow modulation. Inset: reflectance change within 60 seconds.

Furthermore, we have investigated the modulation speed of the ITO-HfO₂-Al modulator. We observed two stages of modulation: namely fast modulation and slow modulation. Fig. 4-5(a) shows the reflectance at modulation angle with respect to time. We can see when positive or negative bias is applied, the reflectance almost instantly shifts up or down; also, if it's turned to zero bias, the reflectance quickly recovers to the baseline level. The fast modulation continues for few milliseconds or less, which results in less than 0.5 percent modulation depth. The second stage is slow modulation. As shown in Fig. 4-5(b), after the first stage, the reflectance is keeping increasing or decreasing under applied voltage. In 300s, the reflectance could increase by 4.65% under positive bias, or decrease by 7.92% under negative bias. We can see the slope gets smaller and smaller as time elapses, which indicates a slower and slower absorption change. Besides, given longer time

at a specific bias, for example, 30 minutes, even larger modulation depth could be observed.

4.4 ENZ effect of conductive oxide

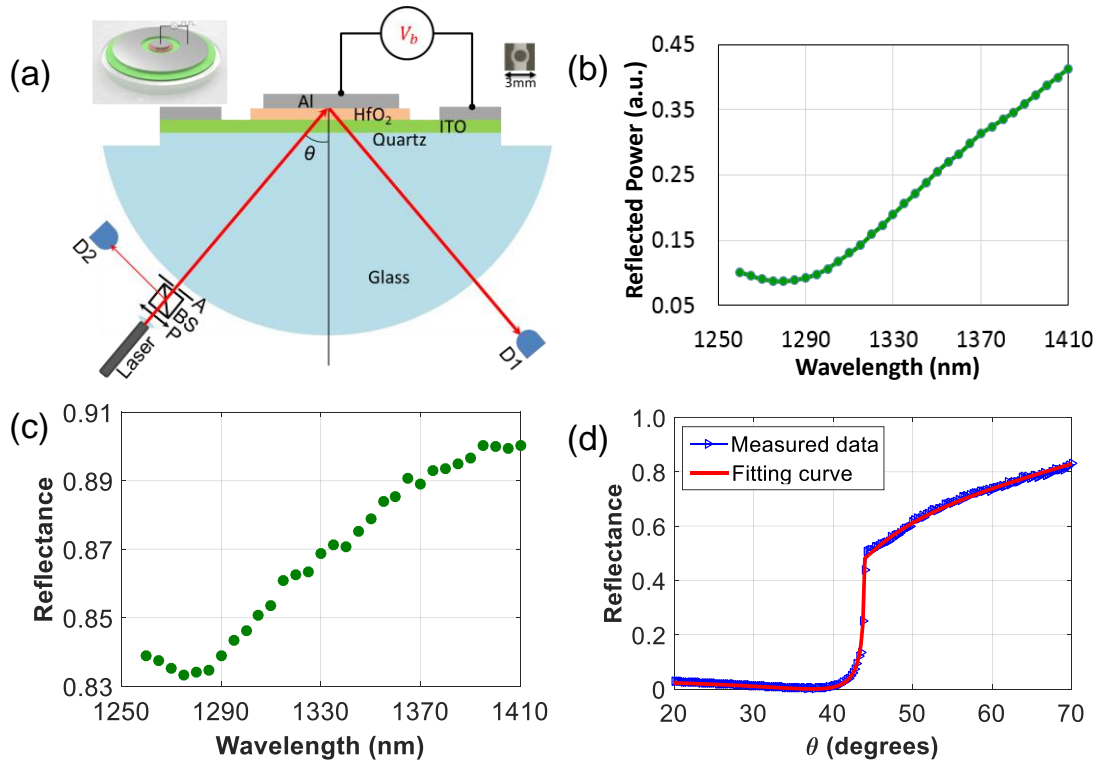


Figure 4-6. (a) Illustration of the ITO/HfO₂/Al structure and experimental setup. The dimensions are not in scale. The Quartz substrate is about 0.5mm thick and the diameter of the hemicylindrical prism is about 100mm. Insets: 3D schematic of the device (upper left) and the picture of the fabricated device (upper right). (b) At incident angle $\theta = 70^\circ$, the reflected power as a function of working wavelength at original state (no bias) for the ITO/HfO₂/Al sample. (c) At incident angle $\theta = 70^\circ$, the R - λ measurement for a 10-nm ITO film on quartz. (d) The R - θ measurement for a 10-nm ITO film on quartz for TM polarized light at $\lambda=1280$ nm and the fitting curve.

In Section 4.3, the MIC EO modulator does not exhibit ENZ effect of the active material. This might be due to the fabrication method that makes its cross-over wavelength out of our investigated spectral range. Therefore, we update the fabrication process. The

ITO film is deposited by PVD75 RF sputtering on 200 °C substrate with 2% oxygen flow ratio [119]. A 60 s deposition time yields ~10 nm thick ITO film. The sheet resistance of the ITO film on quartz substrate was measured to be ~200 Ω /sq. Following the ITO film, a 10-nm HfO₂ film is produced by the ALD, and finally, 150-nm Al is deposited by evaporation. The reduced insulating layer thickness is targeting for an enhanced field effect. The dimension of the modulator slightly decreases, as shown in the upper right inset of Fig. 4-6(a). The same test setup is used here.

In the previous section, the reflectance as a function of incident angle is measured for a given wavelength. In this work, at a specific incident angle $\theta = 70^\circ$, the reflected light power as a function of working wavelength for the transverse magnetic (TM) polarization of light is first measured and plotted in Fig. 4-6(b). Note that the input light power is kept the same for all wavelengths. As can be seen, there is a dip around $\lambda=1280$ nm in the R - λ plot. This dip corresponds to the maximum absorption, and ENZ should be in the vicinity of the dip. From the theory (Section 3.3), we know that When $|\epsilon_{ITO}| \rightarrow 0$, the electric field in ITO can be greatly enhanced and power dissipation p_d reaches the maximum. As a result, ENZ represents an absorption resonance for TM light. Figure 4-6(c) shows similar result by measuring the R - λ relation of pure ITO on quartz sample, also demonstrating an ENZ effect of ITO film around $\lambda = 1280$ nm. To quantitatively verify this, we measured the reflectance (R)-incident angle (θ) relation of pure ITO on quartz sample at $\lambda = 1280$ nm and fit the dielectric constant of ITO, as shown in Fig. 4-6(d). The fitting parameter $\epsilon_{ITO} = 0.209 + j0.477$. Here, if we adopt $\epsilon_\infty = 3.9$, $m^* = 0.35m_e$ [194], then based on the

Drude model, other parameters of ITO can be extracted as $\omega_p = 2.85 \times 10^{15} s^{-1}$, $\gamma = 1.9 \times 10^{14} s^{-1}$, and $N = 8.94 \times 10^{20} cm^{-3}$.

Furthermore, we investigate the field-effect optical modulation based on the ENZ COx. In the MIC structure, light absorption is controlled by the electric-field induced charge in the active ITO film, which is adjacent to the gate oxide. As shown in Fig. 4-7, there exist three states for the device, namely original state (O), depletion (D), and accumulation (A). The whole ITO film stays at original state with no applied bias. When a positive bias is applied on the ITO film, the free electrons in the ITO film close to insulator-ITO boundary will be depleted. The depletion layer (ITO-*d*) thickness, l_d , is about few nanometers. Without free carriers, the absorption by the depletion layer is negligible; equivalently, the ITO absorption layer thickness decreases. Thus, the structure becomes less absorptive. On the contrary, if negative bias is applied on the ITO, more free electrons would accumulate on the ITO film surface. The result is that the accumulation layer is more absorptive. The accumulation layer (ITO-*a*) thickness, l_{ac} , is about few Debye lengths (≤ 1 nm).

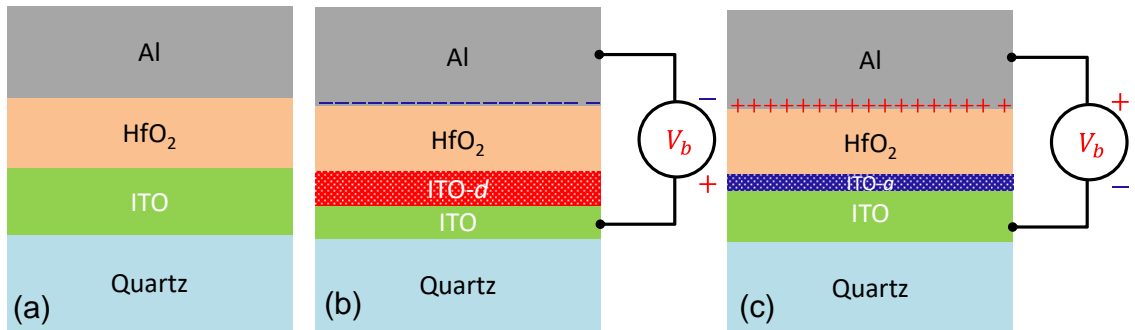


Figure 4-7. (a) The MIC structure under no bias (original). (b) The MIC structure under negative bias (depletion). (c) The MIC structure under positive bias (accumulation).

In Section 4.3, we performed DC test on the fabricated device, and revealed the bias polarity-dependent modulation effect: the absorption of the EA modulator could be increased by negative bias or decreased by positive bias. In particular, the light absorption to DC bias is composed of significant ratio of slow response. The fast response which happens within few milliseconds from the moment of switching on DC bias only contributes to a small portion of modulation depth. The majority of modulation depth is accumulated over a long period of time (over 30 minutes). Similarly, in this work, we observed, for the same positive or negative bias, the modulation depth increases with time (up to several minutes), as shown in Fig. 4-8(a). The slow response may due to the unstable property of ITO under a large DC bias. Similar phenomenon is found more recently in the investigation of a plasmonic memristor based on an MIC structure from another group [191]. The authors attribute the large but slow modulation to the formation of a reversible conductive path in the dielectric layer induced by applied DC voltage, which results in resistive switching. Although a relatively large modulation depth is achieved, the slow response does not contribute to the modulation working at high speed. To this end, we test the FEOM in response to AC sine signals. All tests are performed in the ATR setup.

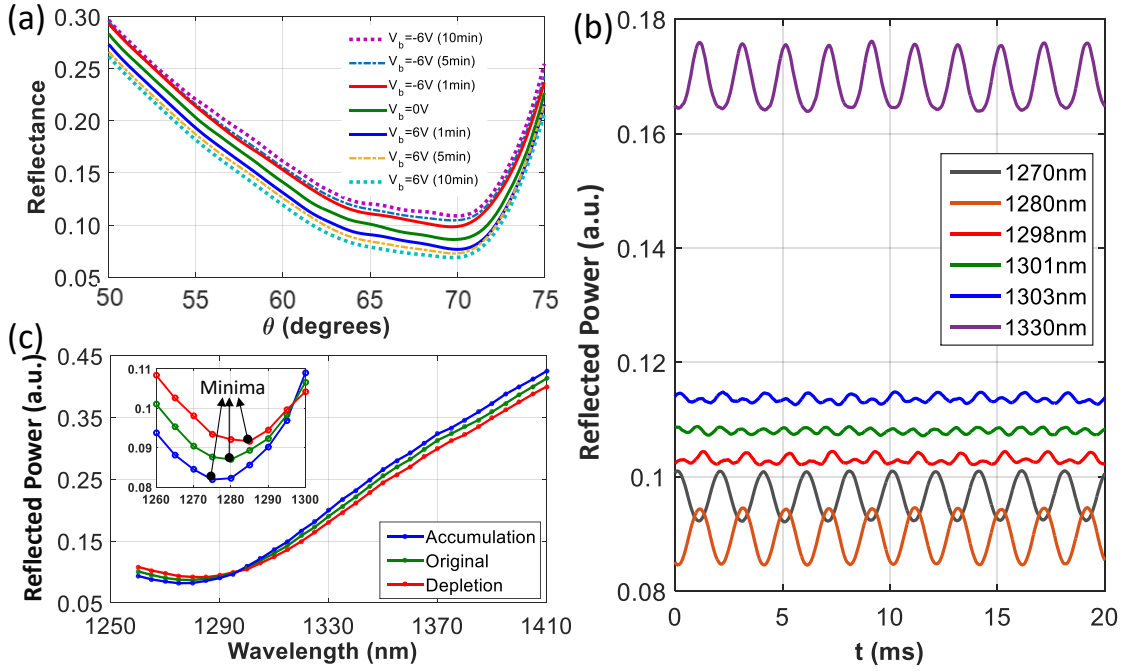


Figure 4-8. (a) The R - θ measurement under DC biases at $\lambda=1280\text{nm}$ with increased time (b) Output waveforms of the reflected light power for different wavelengths when the modulator is under $V_{pp}=12\text{V}$, 500 Hz sine electric signal. (c) The reflected power as a function of incident light wavelength for A, O and D states. The inset shows the minimum value of the three curves, which correspond to ENZ.

In this work, a function generator is used to apply an AC sine signal on the device. The photodetector D1 (Thorlabs SM1PD5A) collects the reflected light power and converts it into an electric signal in an oscilloscope. A $50\text{-}\Omega$ load is used to convert the photocurrent into voltage, and we record the reflected power as R_O . In this paper, the modulation depth is defined as $M = (R_{O_{max}} - R_{O_{min}})/R_{O_{max}}$. We first applied a 500 Hz, $V_{pp}=12\text{V}$ sine signal on the MIC modulator at a specific wavelength, and an output wave with the same frequency was observed on the oscilloscope. Then, we rotated both the prism and D1 to find the optimal incident angle where it exhibited the largest modulation depth. After the optimal angle was set ($\theta = 70^\circ$ in this work), we examined the output waveform at

different wavelengths. Note that the AC bias results in a switch between depletion ($V_b > 0$) and accumulation ($V_b < 0$) states.

In the test, the input light power maintains constant for all wavelengths between 1260 nm and 1410 nm. The output waveforms for different wavelengths are plotted in Fig. 4-8(b). Three factors define each waveform: the average, \bar{R}_O , peak-to-peak variation, $R_{O_{pp}}$, and frequency, f . Our experiments show the results as follows.

(1) \bar{R}_O changes with working wavelength. \bar{R}_O decreases from 1260 nm to minimum at 1280 nm, and then increases. This is consistent with the results shown in Fig. 4-6(b), where a dip exists at 1280 nm.

(2) $R_{O_{pp}}$ is minimized at 1301 nm, which corresponds to the cross-over wavelength.

Starting from smaller wavelength, we can see $R_{O_{pp}}$ reduces to a minimum at $\lambda_c=1301\text{nm}$, and then bounces back. In detail, the crests and troughs of the waveform are squeezed as λ approaches λ_c . At the cross-over wavelength, the crests low down to become troughs, while the troughs rise to become crests. Consider that light absorption would be either increased by electron accumulation or decreased by electron depletion according to the working principle. Here, if the troughs correspond to accumulation and the crests correspond to depletion, the modulation effect must have undergone an inversion at the cross-over wavelength.

(3) When R_{Opp} goes to very small, the frequency f nearly doubled. An interesting phenomenon here is that at the cross-over wavelength $\lambda_c=1301\text{nm}$, the frequency of the output wave is double that of the applied signal.

Conceptually, the closer ϵ_{ITO} is to zero, the larger the light absorption will be. Imagine an extreme case that the maximum absorption is achieved at a certain wavelength, both accumulation and depletion would decrease absorption. When the applied voltage runs for one cycle, (A) \rightarrow (O) \rightarrow (D), the power reflectance will be (increase) \rightarrow (normal) \rightarrow (increase) or “ $\cap_ \cap$ ”, which is roughly similar to the waveform of $|\sin(2\pi ft)|$. Thus, the frequency seems doubled. In detail, in the output waveform in Fig. 4-8(b), the crests, which correspond to the decrease in absorption would remain; while the troughs, would turn into crests, indicating a conversion from absorption increase to decrease. This conversion is observed when the working wavelength is scanned through the cross-over wavelength, which can be seen by comparing the output waveforms at $\lambda=1298\text{nm}$, 1301nm and 1303nm . The double-frequency waveform is an interaction of accumulation and depletion at the cross-over wavelength, where ITO is at an extreme ENZ state.

According to the observation, the effect of carrier depletion and accumulation on increasing or decreasing absorption is opposite below and above the cross-over wavelength. In Fig. 4-8(c), when $\lambda < \lambda_c$, the reflectance by depletion is greater than that by accumulation; when $\lambda > \lambda_c$, the reflectance by accumulation is greater than that by depletion. The reflectance curve by the ITO film without bias is located between the curves for depletion and accumulation. This can be explained by how carrier accumulation or

depletion quantitatively changes the optical property of ITO. When $\lambda < \lambda_c$, ITO layer is at dielectric state with a positive dielectric constant. Carrier accumulation would push the ITO-*a* layer towards the ENZ state, resulting in absorption increase. On the contrary, when $\lambda > \lambda_c$, ITO layer is at metallic state with negative dielectric constant. With excess free carriers, ITO-*a* layer would deviate further away from ENZ state, which decreases absorption. Therefore, the cross-over wavelength λ_c witnesses the inversion of optical property of ITO layer from dielectric to metallic, as well as the inversion of modulation effect in active ITO layer brought by carrier accumulation or depletion.

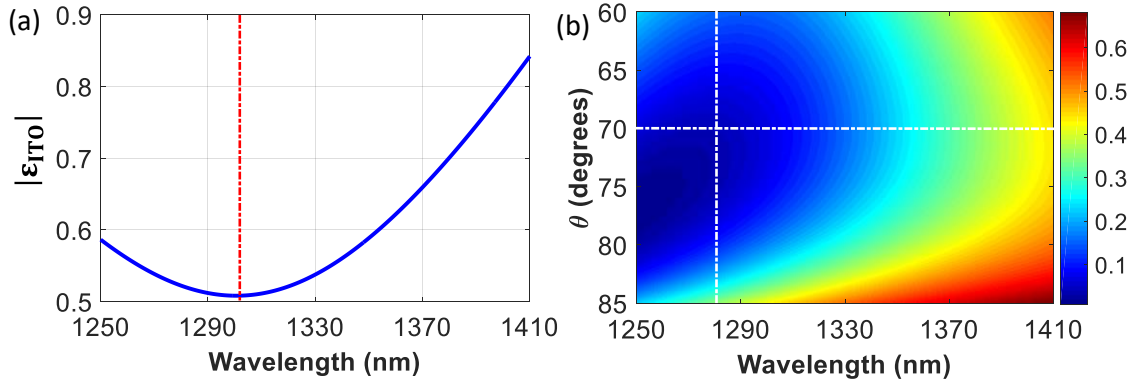


Figure 4-9. (a) Drude model calculation for $|\epsilon_{ITO}|$ as a function of wavelength. (b) Reflectance calculation of the MIC structure by sweeping incident angle and wavelength.

Despite the ENZ effect shown at the cross-over wavelength $\lambda_c=1301\text{nm}$, the maximum absorption for the MIC modulator is found around $\lambda=1280\text{nm}$. This shift could be owing to the working mechanism of the MIC structure and the ATR measurement setup. To verify this, we calculate $|\epsilon_{ITO}|$ as a function of wavelength with extracted ITO parameters $\epsilon_\infty = 3.9$, $\omega_p = 2.85 \times 10^{15} \text{s}^{-1}$, $\gamma = 1.9 \times 10^{14} \text{s}^{-1}$. From Fig. 4-9(a), the minimum value of $|\epsilon_{ITO}|$, which indicates the cross-over wavelength, is identified at $\lambda=1300\text{nm}$. Then, with

the same set of parameters, we calculate the reflectance of the MIC structure based on transfer matrix method (TMM), where both the incident angle θ and wavelength are swept. As seen in Fig. 4-9(b), at the optimal incident angle ($\theta = 70^\circ$) used in the measurement, the minimum reflectance is located near $\lambda=1280\text{nm}$, which matches the experimental result. In addition, according to the Fig. 4-9(b), the incident angle where maximum absorption is found varies with wavelength.

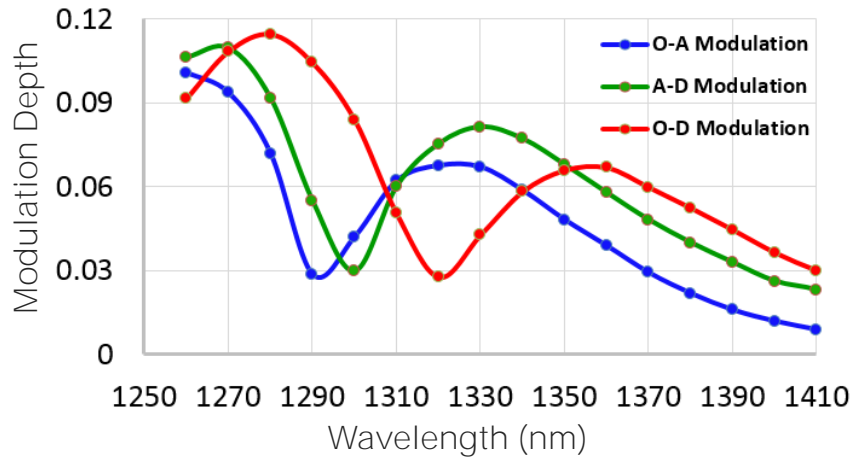


Figure 4-10. M - λ relations for O-A, A-D, and O-D modulations under 500Hz, $V_{pp}=12\text{V}$ AC signal.

Furthermore, modulation can be achieved between any two states among “original”, “depletion”, and “accumulation”. We combine the 500Hz, $V_{pp}=12\text{V}$ AC signal with a 0V, +6V or -6V DC offset in order to examine A-D, O-A, and O-D modulations, respectively. Figure 4-10 plots the modulation depth as a function of incident light wavelength for the three modulations. Minimum “A-D” modulation occurs at cross-over wavelength. Peak “A-D” modulation depths are located at about ± 30 nm from cross-over wavelength. The

spectrum shift in the three curves is caused by the DC offset-induced optical property change of the active ITO film.

4.5 Working bandwidth and modulation speed

In the measurement, we have observed similar modulation effect all the way from 1260nm to 1620nm; however, compared with the modulation caused by DC bias in Section 4.3, the modulation depth becomes much smaller because considerable slow modulation has been eliminated by applying AC electric signal. Besides, the modulation depth is much more sensitive to wavelength. When the wavelength is far away from the ENZ region, the modulation depth becomes trivial. For example, as can be seen in Fig. 4-11, the modulation depth for A-D modulation drops to less than 3% when $\lambda > 1400\text{nm}$. As expected, the ENZ region of the modulator depends on the property of ITO layer, which can be controlled by fabrication process. We have obtained ITO films with sheet resistance from 100 to $400\Omega/\square$, and the resulting cross-over frequency λ_c varies within, or even beyond the wavelength range we investigate. Despite the difference in λ_c due to ITO film property, the EO modulators all behave in a comparable manner as illustrated in this paper. Promising applications could be achieved by this property; for example, one could make EO modulators working at the desired wavelength.

Compared with the MIC modulator in Section 4.3, which shows very slow response under DC bias, the updated version in this section has a boost in speed. This is also one of the goals of the optimization. Nevertheless, high-speed operation is yet to be verified. Due to a limited working bandwidth of Ge photodiode D1, absorption modulation could hardly

be observed at frequencies over 10 kHz. In order to well investigate the working speed of the EO modulator, we utilized an AC-coupled InGaAs photodetector (Newport 818-BB-30A). Figure 4-11(a) illustrates the reflected power fluctuation of MIC EO modulator under an AC sine electric signal of $V_{pp}=12V$ working at 1 MHz. The incident light wavelength $\lambda=1280nm$. Though the EO modulation has been achieved at MHz scale, however, the rapid decrease of modulation depth obviously shows the speed limitation of the MIC EO modulator. As shown in Fig. 4-11(b), starting from over 10% at 1 kHz, the modulation depth quickly drops below 1% at 500 kHz.

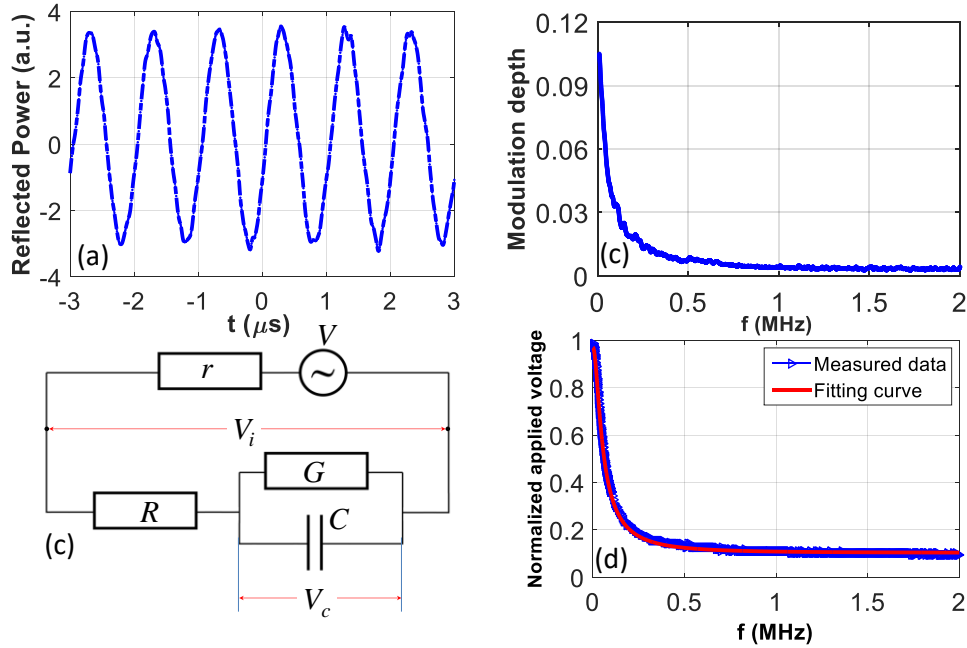


Figure 4-11. (a) The output waveform for modulating frequency $f=1MHz$. (b) Modulation depth as a function of modulating frequency. (c) The circuit diagram for the MIC structure. (d) For a given V , the normalized applied voltage on the device as a function of modulating frequency.

We believe that RC delay is the factor that limits the speed of the device. In order to verify this, we examined the electric circuit of the MIC structure, shown in Fig. 4-11(c).

Here R is a series resistance brought by the function generator and device, $1/G$ is a resistor parallel to the capacitor, and r is a 1 k Ω resistor externally added to the circuit. We measured the applied voltage on the device V_i as a function of modulating frequency f on condition that the total applied voltage V is normalized to 1. Plotted in Fig. 4-11(d), the results show agreement with Fig. 4-11(b), which indicates that only a very small portion of voltage is applied across the HfO₂ layer at higher frequencies. Based on the equation $V_i = V \frac{1+R(G+j\omega C)}{1+(R+r)(G+j\omega C)}$, we fit the V_i - f curve (Fig. 4-11(d)) and extract the circuit RC constants as $C=4.13$ nF, $R=111.7$ Ω , and $1/G=32$ k Ω . According to the actual dimension of the sample, the capacitance is calculated as $C = \frac{\epsilon A}{d} \approx 25$ nF ($\epsilon = 25$ is used here for HfO₂). The measured value is several times smaller than the theoretical value, probably due to the over estimation of the dielectric constant of the insulating layer as well as capacitor fringe effect. However, the RC constants are still too large to allow for a fast modulator. We are optimizing the design and fabrication process for better device performance, and we are expecting a speed boost of several orders by shrinking the size of the modulator from millimeter scale to micro- or even nano-scale.

4.6 Conclusions

In this chapter, we have experimentally demonstrated multi-layer MIC EA modulators based on ITO. The initial investigation on the modulators has shown broadband EA modulation with a relatively large modulation depth under DC biases. The switching speed is rather low. We optimized the design and fabrication process, and further explored the tunable property of ITO, and verified its ENZ behavior in the MIC structure around telecom

wavelength. Light absorption of the MIC structure can be modulated by both carrier accumulation and depletion. The modulation effect by accumulation and depletion in changing light absorption is opposite below and above the cross-over wavelength, near which the maximum modulation depth can be found. The ENZ working region depends on ITO film property, which can be tuned in the fabrication process. The modulation speed is mainly limited by device RC constant, which should be solved by more compact dimensions and optimized design. The results in this chapter may find promising applications in making efficient and broadband EO modulators.

5. ULTRA-COMPACT FIELD-EFFECT EA PLASMONIC MODULATOR

In Chapter 4, field-effect EA modulation based on COx has been experimentally demonstrated through an MIC structure. Cross-over wavelength which corresponds to ENZ has been observed at the telecom wavelength. However, the investigation is mainly focusing on the material property. Neither compact dimension nor high-speed operation of the modulator has been achieved. In this chapter, based on the previous study, an ultracompact field-effect EA plasmonic modulator will be proposed and investigated. The effective modulation length of the modulator is only 800nm, which is the smallest recorded dimension according to our knowledge. Preliminary results show successful operation of the modulator at 500 MHz, which is limited by the testing setup. Potential EA modulation at GHz is expected with this ultracompact field-effect plasmonic modulator.

5.1 Background and principle

It has been discussed in detail that COx could be promising alternative active material for EO modulation. Besides our research, many EO modulators have been proposed based on COx. To apply a COx as the active medium in an EO modulator, one challenge is that the field-effect-induced charge layer is only few nanometers thick. To enhance the impact of the charged layer on light absorption, three strategies are taken in this work.

First, the COx is integrated into an MIM plasmonic waveguide. Surface plasmons as hybrid electrical-optical waves give rise to strong confinement, which makes their

propagation to be extremely sensitive to minor changes in the optical properties of the guiding materials. This provides a remarkable opportunity for optical modulation. Various plasmonic EO modulators have been reported since the 1980s [20, 202-205], including three based on CO_x [83,191,199]. In particular, Dionne, et al. [20] reported an EO modulator integrating a metal-oxide-silicon junction into two silver films, where the modulating electric field can switch the waveguide between guiding and cut-off states. However, its large extinction ratio extremely relies on the junction uniformity in the light propagation direction. Two more recent works from another group reported microscale plasmonic phase modulator [59] and plasmonic intensity modulator [60]. In both works, MIM plasmonic waveguides are employed, and nonlinear polymers work as the active media with modulator waveguide length shrunk to 10s of micrometers. Recent experimental works [83,198,199] report the integration of the MIC structure on the silicon waveguide, in a plasmonic waveguide, and below a glass prism, respectively. Modulation extinct ratio is reported 1 dB/μm in Ref. [83], and 2.71 dB/μm in Ref. [199]. In both cases, the dynamical operation of the modulators has not been reported. The result from Ref. [196] shows that the part of large modulation may only work at low speed, which coincides with our previous observation. Whether the modulation can work at high speed is still a question.

Second, HfO₂ is employed as the insulator layer to enhance the field effect. HfO₂ has high DC dielectric constant, large dielectric strength, and is transparent for NIR light. Basically, the MIC structure functions as a parallel plate capacitor. Thus, a high-k insulator can induce large surface charge for a given gate voltage.

Third, two MIC structures are designed back-to-back to double the field-induced charge, simultaneously on top and bottom sides of COx, for the same gate voltage. The use of this double capacitor-gating scheme in modulators can date back to dual-channel EO modulators proposed in 1970s or earlier [207]. It was recently used in a graphene modulator [208] and a proposed silicon slot-waveguide-based EO modulator [209]. The entire structure in this work is thus a metal-insulator-COx-insulator-metal (MICIM) structure, as shown in Fig. 5-1(a). The COx used in this work is ITO. Another advantage of using the double insulator layers is to decrease the MIM plasmonic waveguide attenuation, which sharply decreases with the increase of insulator thickness, especially at the nanoscale.

This work shows that the three strategies can greatly improve the modulator performance and result in an EA modulator with a propagation length only 800 nm. To our knowledge, this is the first experimental demonstration of an EO modulator with a nanoscale waveguide length. The EO modulators in previous works [58,59,82,191,198,199] involve waveguides with nanoscale width or thickness, but the waveguide length is still at the microscale.

As shown in Fig. 5-1, the principle of this EO modulator is quite straightforward. Light absorption in the gap between two gold films is controlled by the electric-field-induced charge in the ITO layer. Each MIC structure functions as a parallel plate capacitor. The field induced charge on each side of ITO can be calculated according to $Q = \epsilon EA$, where ϵ is the DC dielectric constant of HfO₂, E is the applied electric field across the HfO₂ layer, and A is the capacitor area. According to the bias polarity and strength, an MIC structure may work in two well-known modes. When a positive bias is applied on the ITO layer,

depletion (of electrons) ($Q > 0$) occurs. Effectively, the thickness of ITO layer decreases and the MICIM waveguide becomes less absorptive, resulting low attenuation (i.e. ON state). When a negative bias is applied at the ITO layer, accumulation (of more electrons) ($Q < 0$) occurs. The ITO layer becomes more conductive and the MICIM waveguide becomes more absorptive, resulting in high attenuation (i.e. OFF state).

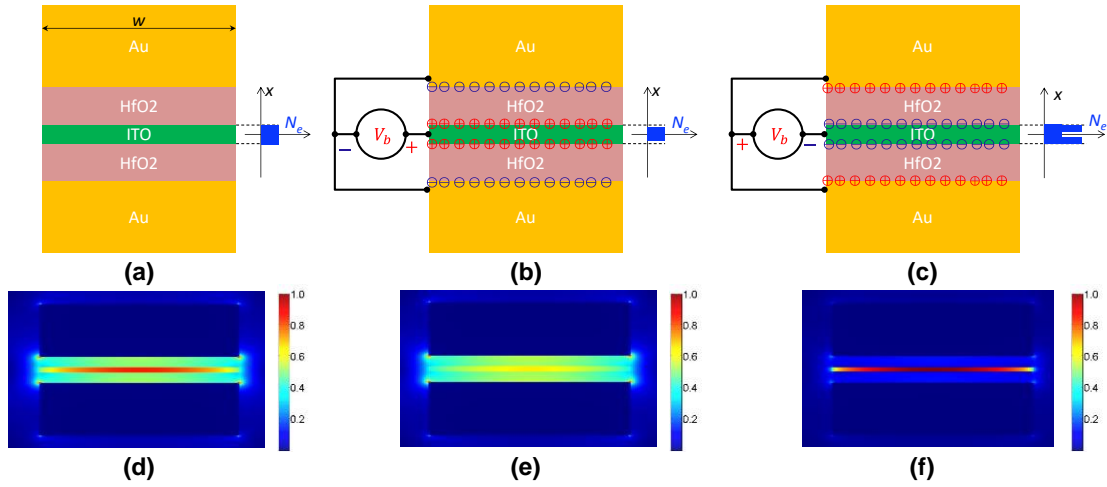


Figure 5-1. Illustration of the working modes of the metal-insulator-CO_x-insulator-metal structure: (a) Without bias. (b) Depletion mode, where the ITO is less absorptive and the waveguide has lower attenuation. (c) Accumulation mode, where the ITO is more absorptive and the waveguide has higher attenuation. (d) The mode profile for the no bias case. (e) The mode profile for the depletion case. (f) The mode profile for the accumulation case.

In our work, the thickness of ITO is 10 nm; each HfO₂ layer is 20 nm thick. At 1550 nm, the refractive indices of HfO₂ and gold are 2.07 and 0.583+j9.864, respectively. We fabricated ITO film at 60°C on quartz and obtained its carrier concentration as $N_d = 5.6 \times 10^{20} \text{ cm}^{-3}$ by Hall effect measurement. Based on the Drude model, the dielectric constant of ITO at 1550 nm can be calculated as $0.44 + j0.32$. If $V_b = -20 \text{ V}$ bias is applied across the HfO₂ layer, and assume the accumulation layer thickness is $l_{ac} = 1 \text{ nm}$, the

excited accumulation charge will be $\Delta N = \frac{Q_s}{el_{ac}} = 1.38 \times 10^{21} \text{cm}^{-3}$. The dielectric constant in the accumulation layer changes to $-8.05 + j1.12$. If $V_b = +20 \text{ V}$ bias is applied across the HfO_2 layer, all ITO layer will be depleted. The dielectric constant in the depletion layer is 3.9. Assume the width of the MICIM structure $w = 200 \text{ nm}$. The attenuation in the three cases is calculated to be 15.49, 15.77, and 13.12 $\text{dB}/\mu\text{m}$, respectively. Thus, an extinction ratio 2.65 $\text{dB}/\mu\text{m}$ can be achieved. Figure 5-1 (d-f) shows the mode profiles ($|E|$) for the three cases. The following table summarizes the parameters of the MICIM structure and attenuation for the plasmonic waveguide under the three cases.

$\lambda=1550 \text{ nm}$	No bias	Accumulation	Depletion
$\epsilon = \epsilon' + j\epsilon''$	0.44+j0.32	$-8.05+j1.12$	3.9
(Active + inactive + Active) thickness	(0+10+0) nm	(1+8+1)nm	(2.5+5+2.5)nm
Attenuation	15.49 $\text{dB}/\mu\text{m}$	15.77 $\text{dB}/\mu\text{m}$	13.12 $\text{dB}/\mu\text{m}$
Extinction ratio	2.65 $\text{dB}/\mu\text{m}$		

5.2 Schematic and fabrication

The schematic of the device is illustrated in Fig. 5-2(a). The device fabrication consists of a series of layer-by-layer processes. For accurately patterning each layer, general photolithography and lift-off processes are applied. The fabrication starts from the deposition of 10 nm thick Ti adhesion and 100 nm thick gold layers on the quartz substrate. Then, a 20-nm HfO_2 is deposited as the first buffer insulator by atomic layer deposition (ALD). The next process is the sputtering of 10-nm active material, ITO, at a substrate temperature of 60°C [116]. After that, another 20-nm thick HfO_2 is deposited to provide the second buffer layer. Finally, 150-nm thick gold is deposited to define the light input port, the modulator length as well as to form electric contacts.

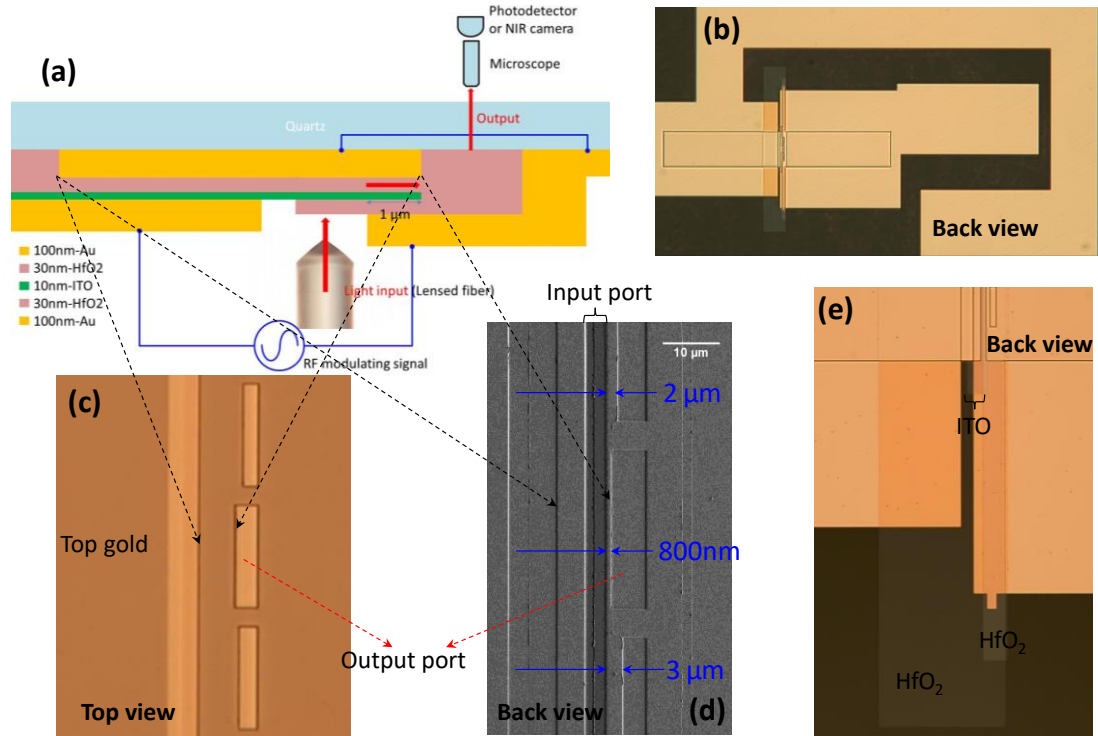


Figure 5-2. (a) Schematic of the fabricated EO modulator and the test setup. (b) Back view of the modulators and their GSG contact electrodes. (c) Top view of the output port. (d) Back side SEM picture of the device input and output ports. (e) Bottom view of the edge of the device.

To conduct measurement, the sample is flipped upside down as illustrated in Fig. 5-2(a). For easy description, the quartz substrate is treated as the top layer. Figure 5-2 (b) is the back side microscope image of the whole fabricated device. Figure 5-2 (c) shows the top side microscope images of the fabricated device showing three output ports. Figure 5-2 (d) is the back side scanning electron microscope (SEM) image of the device showing detailed dimension. Figure 5-2(e) is the image of the edge of the device taken from the bottom side showing the multi-layer stacks. As can be seen in Fig. 5-2 (d), there are three modulators with waveguide lengths, 2.0 μm, 800 nm, and 3.0 μm, respectively. The three modulators share the same GSG contact electrodes. Our investigation is focused on the 800-nm waveguide.

5.3 Experimental validation of modulation effect

In the test, light from a tunable laser is amplified by an erbium-doped fiber amplifier (EDFA) and then coupled into the sample through a lensed fiber from the bottom side of the sample. The lensed fiber can focus NIR light into a $\sim 2\ \mu\text{m}$ diameter spot at the working distance of $\sim 15\ \mu\text{m}$. The entire sample is covered by either the top or bottom gold layer, or both layers. For easy explanation, the top and bottom gold layers are shown as slightly different colors. The gold layers are thick enough so that light cannot directly propagate through as shown in Fig. 5-2(b & c). The input port is a $4\text{-}\mu\text{m}$ wide slit in the bottom gold layer as shown in Fig. 5-2(d). Light propagation through the sample must follow the gaps, i.e. plasmonic waveguides, between the two gold layers. See Fig. 5-2(a). Two MIM plasmonic waveguides simultaneously exist in our modulator. The left side one is an Au-HfO₂-ITO-Au waveguide, which has very large attenuation and its length is designed to be $4\ \mu\text{m}$. Thus, the light transmission through the Au-HfO₂-ITO-Au waveguide is negligible. The right side one is an Au-HfO₂-ITO-HfO₂-Au waveguide, which is our modulating waveguide. It has much smaller attenuation, owing to the double HfO₂ layers, and much short length, only $800\ \text{nm}$, terminated by a slit in the top gold layer, which works as the output port. Therefore, the input and output ports are linked by the Au-HfO₂-ITO-HfO₂-Au waveguide.

As illustrated in Fig. 5-2(a), the top gold layer seems three separate parts, but the middle and right parts actually represent a continuous film with a $5\ \mu\text{m}$ -by- $30\ \mu\text{m}$ rectangular window, as shown in Fig. 5-2(c), which means the top gold layer only has two electrically insulated parts. The bottom gold layer is also two isolated films: the left part works as a metal contact electrode for ITO; the right part simultaneously works as another electrode and a confining layer of the Au-HfO₂-ITO-HfO₂-Au plasmonic waveguide. As can be seen in Fig. 5-2(a), two confining gold layers of this

waveguide are electrically connected at the right end. Consequently, when a voltage is applied between ITO and bottom gold layer, the same voltage is always applied between ITO and the top gold layer. The result is the double capacitor gating scheme as shown in Fig. 5-1. The gate voltage comes from a function generator and is applied to the electrodes through a microwave GSG probe from the sample bottom side. See Fig. 5-2(b). The picture of the whole setup is shown in Fig. 5-3(a).

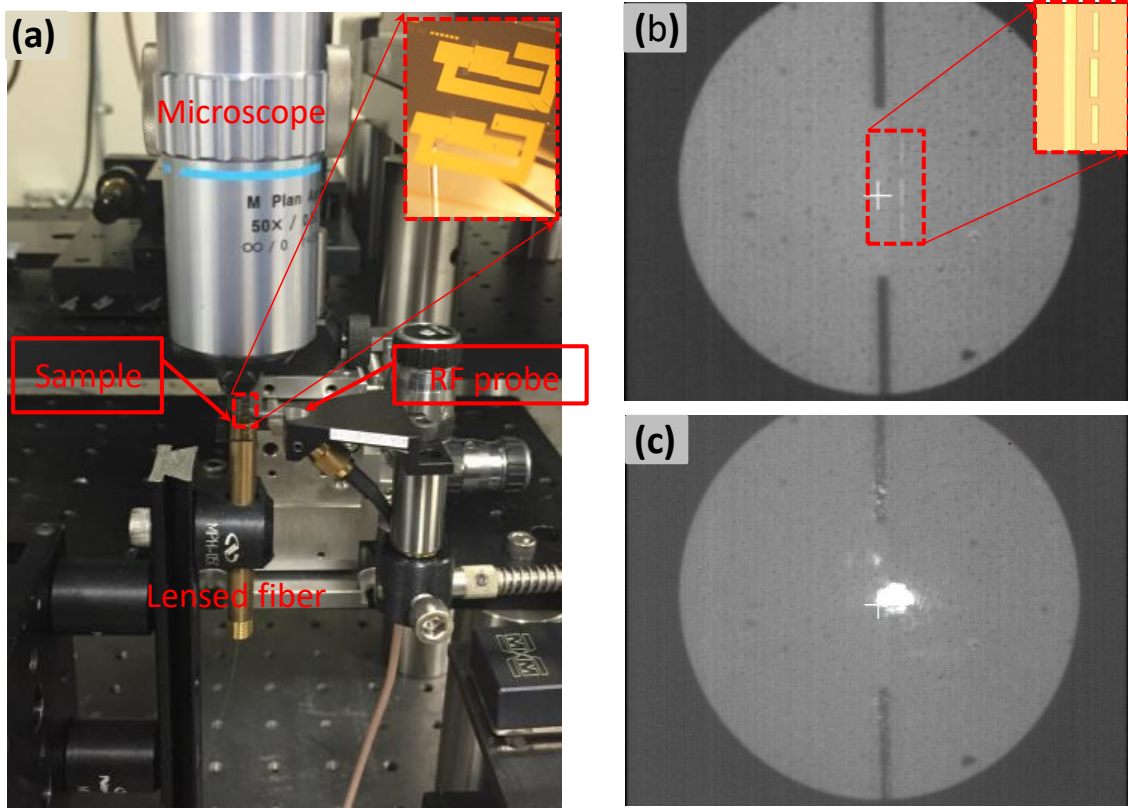


Figure 5-3. (a) Picture of the experimental setup. Inset: picture of the tested device. (b) Image of the output ports by the NIR camera. Inset: the output ports. (c) Image of the output of the device through the NIR camera when NIR light is fed in from the input port.

In the experiment, a microscope, installed with an NIR camera at the top through an adapter, is placed over the sample for observation, alignment, and NIR imaging. The microscope is first

adjusted to locate the output port. Fig. 5-3(b) shows the image of the sample by the NIR camera. Then amplified NIR light ($\lambda = 1560$ nm) is fed into the input port through a lensed fiber. After the light propagates through the device, it is scattered into the quartz substrate and then into the air. Partial scattered light is imaged by the microscope NIR camera. Figure 5-3(c) shows the light scattering from the middle output window.

When an AC voltage ($14\text{V}-V_{pp}$) is applied on the device, the change of power level of the output light with the voltage fluctuation can be observed. This verifies that the light output is really modulated. The modulation is so obvious that light intensity change in the NIR image can easily be seen by eyes at extremely low frequencies. Our supplemental movies document the modulation at $f = 3$ Hz. [Movies 1](#) and [Movie 2](#) show the output from the modulators with waveguide lengths 800 nm and $2.0\ \mu\text{m}$, respectively.

5.4 Modulation depth and modulation speed

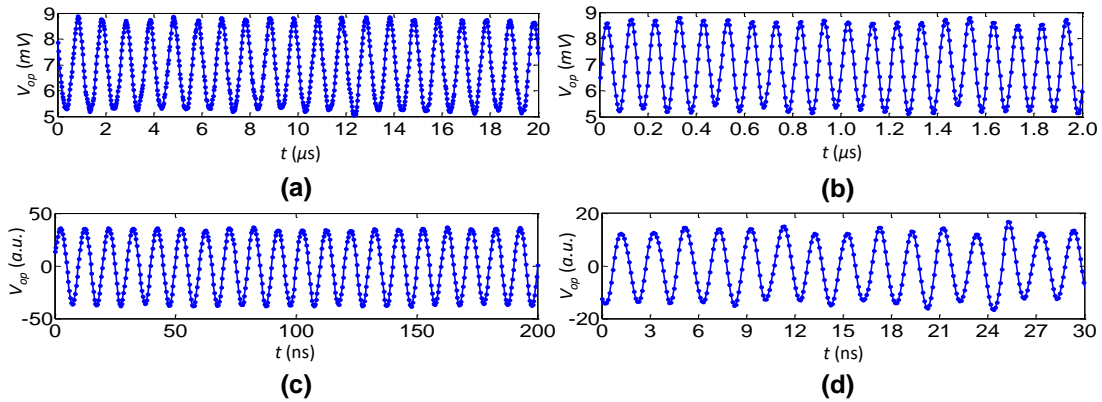


Figure 5-4. Oscilloscope measurement of the output light power under an applied electric signal of (a) 1 MHz, (b) 10 MHz, (c) 100 MHz, and (d) 500 MHz. (a&b) are obtained using a DC-coupled photodetector. (c&d) are obtained using an AC-coupled photodetector.

To test the response of the device to higher frequency modulating voltages, the NIR camera is first replaced by a DC-coupled InGaAs photodetector (Thorlabs PDA10CF), which is positioned exactly at the focused image of the microscope adapter. The photodetector collects the output light power and converts it into an electric signal in an oscilloscope. A 50- Ω load is used to convert the photocurrent into a voltage, V_{op} . Figures 5-4 (a&b) depict the tested photo voltage of the EA modulator under an applied 14 V- V_{pp} RF sine signal of 1 MHz and 10 MHz, respectively. If the extinction ratio is defined by $r_e = \frac{\max\{V_{op}\}}{\min\{V_{op}\}}$, the extinction ratio measured at 10 MHz is around 1.75 or 3.04 dB/ μm . To demonstrate the operation of the modulator at even higher frequencies, the DC-coupled photodetector is replaced by an AC-coupled, amplified InGaAs photodetector (Newport 818-BB-30A), and the output is further amplified by a microwave amplifier. Figures 5-4 (c&d) plot the tested photo voltage of the EA modulator under an applied 14 V- V_{pp} RF sine signal with frequencies $f = 100$ MHz and $f = 500$ MHz, respectively.

Owing to the limitation in the speed of the photodetector, the power level of the incident light, and the input coupling efficiency we observed light modulation only up to 500 MHz. The obtained results show a very promising prospect for an ultra-compact, ultra-fast optical modulator. We are upgrading our testing setup to evaluate its performance at GHz modulating frequencies. The results will be reported in the future.

5.5 Conclusions

In conclusion, we have experimentally demonstrated an 800-nm-long plasmonic EA modulator, which has a significant modulation depth and can potentially work at GHz high speed at telecommunication wavelengths. In this device, we have combined the MIC structure with an

MIM plasmonic waveguide configuration, with double capacitor gating scheme for greatly enhanced field effect. The involved fabrication processes are undemanding and CMOS-compatible. The device may meet the requirements for an ultra-compact and ultra-fast EO modulator as future 3D interconnection, where NIR light propagates between top and bottom sides of chip-based systems and is modulated by electric gate. To this end, both sides of the modulators are passivated and Chip 1 and Chip 2 may be standard CMOS circuits. As shown in Fig. 5-5, a variation of the modulator, yet based on the same principle, may also be employed for future on-chip nanophotonic/nanoplasmonic interconnection.

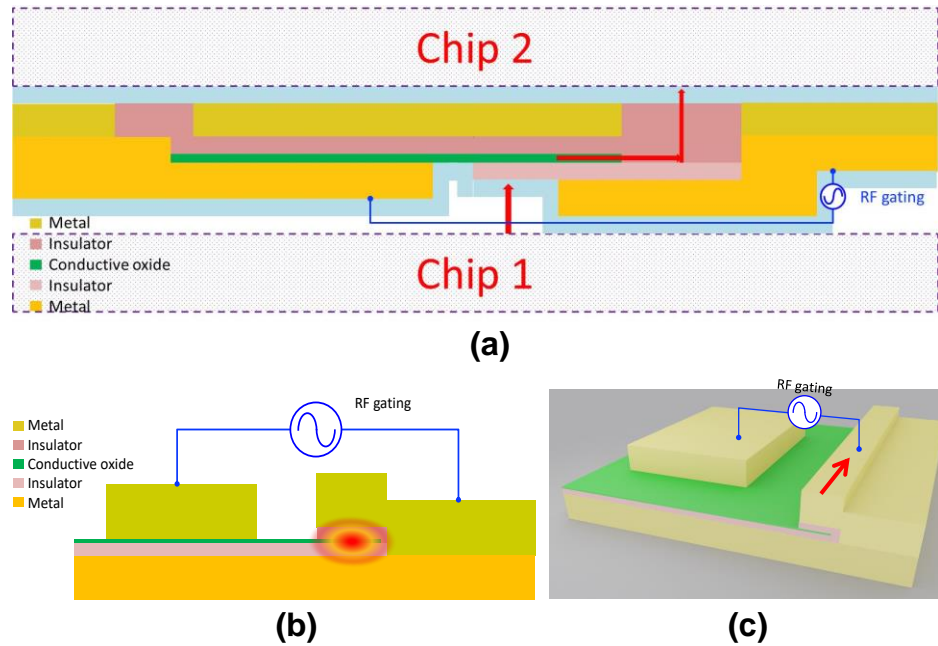


Figure 5-5. The potential applications of the MICIM modulator in 3D interconnection and in integrated photonic/plasmonic circuits. (a) The potential application of the modulator in 3D interconnection, where both sides of the modulators are passivated and Chip 1 and Chip 2 may be standard CMOS circuits. (b, c) The potential application of the MICIM modulator in integrated photonic/plasmonic circuits, where (b) illustrates the front view, and (c), 3D view. Photonic/plasmonic power flow is between the two metal layers in the red arrow direction.

6. NANOSCALE FIELD-EFFECT OPTICAL MODULATORS BASED ON DEPLETION OF ENZ FILMS

In the previous chapters, we have numerically demonstrated EA modulators based on ENZ-slot waveguide by free carrier accumulation [187]. However, the electron density in the accumulation layer nearly exponentially decays with distance, which leads to very non-uniform optical dielectric constant across the accumulation layer. We have also experimentally shown that both accumulation and depletion can lead to EA modulation [191, 192]. Herein, in this chapter, we propose EA modulators each based on the depletion of an ENZ thin film. In contrast to accumulation, the initial film can be designed with uniform carrier concentration and uniform ENZ optical dielectric constant. The depletion can greatly remove the carriers. Thus, optical modulation can be achieved between ENZ and depletion with very large extinction ratios [193].

6.1 Background

In Section 4.1, the operation principle of optical modulators based on MOS structure has been demonstrated. The accumulation layer thickness and the depletion layer thickness can be given by $l_{ac} \approx \pi L_D / \sqrt{2}$ and $w_d = \frac{Q_s}{eN_0}$, respectively. According to the parameters obtained from experiment [191,192], the thicknesses of accumulation and depletion layers are estimated to be very thin due to high carrier concentrations of the fabricated ITO film. For example, w_d is typically less than 2 nm and l_{ac} is usually only a few angstroms. As a

result, we conduct numerical analysis to model the carrier distributions in the double capacitor gating scheme, as illustrated in Fig. 6-1. In this scheme, the thickness of ITO film is set to be 4 nm, and each HfO₂ layer is 10-nm thick. With a doping level of $N = 6.32 \times 10^{20} \text{ cm}^{-3}$ and a bias voltage of 10 V, the scheme is simulated with finite element method (FEM) for both accumulation (Fig. 6-1(a)) and depletion (Fig. 6-1(b)). From the figure, very thin accumulation layers with non-uniform carrier concentrations can be observed. Meanwhile, we can see the 4-nm ITO film is almost depleted by the double capacitor gating scheme. Therefore, we focus our investigation on depletion of an ENZ thin film.

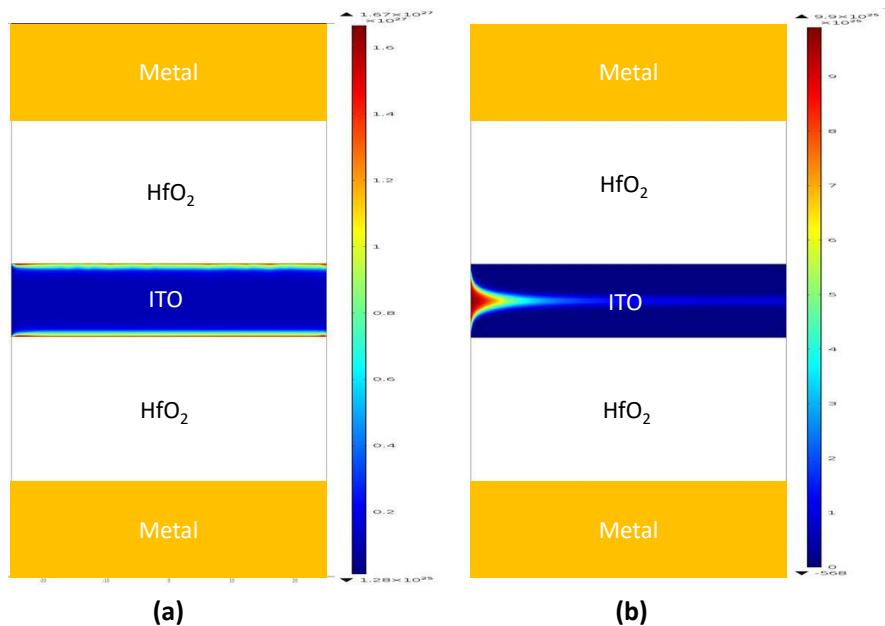


Figure 6-1. FEM simulation of the double capacitor gating scheme on carrier distribution for (a) accumulation and (b) depletion.

6.2 Design and simulation

In the investigation, we consider EA modulators based on the metal-insulator-metal waveguide and Si waveguide platforms, respectively. The double capacitor gating scheme is employed as illustrated in Fig. 6-2(a), where the same gate voltage can induce depletion layers simultaneously on top and bottom sides of the ENZ film. The ultrathin film may be 2D semiconductor or COx. As an example, we first consider an optical modulator based on “metal-insulator-COx-insulator-metal” (MICIM), where ITO works at ENZ, and the metal layer is assumed to be Au owing its chemical stability and low absorption at near-infrared frequencies. Figure 6-2(a) illustrates the MICIM structure to be investigated. Based on the Drude model, for the typical optical parameters for ITO [194]:

$$\epsilon_{\infty} = 3.9, \quad m^* = 0.35m_e, \quad \gamma = 1.8 \times 10^{14} \text{ rad/s},$$

ENZ can be achieved when $N = 6.32 \times 10^{20} \text{ cm}^{-3}$ at $\lambda_o = 1550 \text{ nm}$. The corresponding optical dielectric constant is $\epsilon_r(\text{ENZ}) = 0.0942 + j0.563$, where the minimum $|\epsilon_r|$ can be achieved. Assume the insulator layers are both 10-nm thick HfO_2 , which has a DC and RF dielectric constant of $\epsilon_r = 25$ and dielectric strength $> 1 \text{ V/nm}$. If 10-V positive bias is applied on the ITO, the depletion layer thickness can be estimated to be $\sim 2.2 \text{ nm}$ according to Eqs. (4.1 & 4.3). If the thickness of ITO is designed as 4 nm, then the entire ITO film can be mostly depleted by the double capacitor gating scheme. Figure 6-2(b) depicts the residual electron distribution for the depletion based on the finite element method (FEM) simulation, where a 10-V positive bias is applied at the left end of ITO film. Figure 6-2(c, d) is the 1D scan of electron distribution in Fig. 6-2(b) at $x = 0$. As can be seen, the

maximum electron density at the center ($y = 0$) in ITO reduces to $3.93 \times 10^{20} \text{ cm}^{-3}$ and then sharply decreases to a negligible level within 0.9 nm on both sides. The effect of induced surface charge on the optical properties of gold is negligible as Au has a huge free electron density, $\sim 5.9 \times 10^{22} \text{ cm}^{-3}$. Based on the Drude model, we calculated the complex optical dielectric constant distribution in the ITO as shown in Fig. 6-2(e, f).

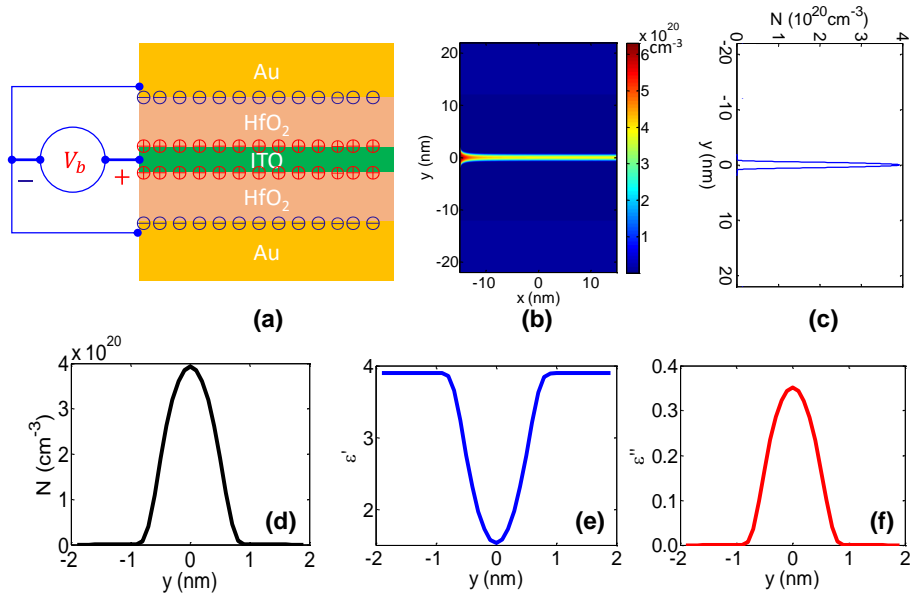


Figure 6-2. (a) Illustration of the metal-insulator-COx-insulator-metal structure working at the depletion mode. (b-d) FEM simulation of the residual electron distribution in the ITO film. (e) The real part of the ITO complex dielectric constant (ϵ') of ITO. (f) The imaginary part of the complex dielectric constant (ϵ'') of ITO.

The double capacitor-gated ITO film can also be used in Si-based waveguides when the metal layers are replaced by n^+ Si, as illustrated in Fig. 6-3(a). In this case, the HfO₂ layers are each assumed as 10 nm thick, too. Note that the n^+ Si layers work at accumulation when the ITO works at depletion. Assume the carrier concentration of the n^+ Si is $N = 1 \times 10^{18} \text{ cm}^{-3}$ and the flat-band condition is satisfied without bias. The thickness of the accumulation

layer in Si is less than 1 nm. Figure 6-3(b, c) depicts the electron density distribution in the ITO and Si. As shown in Fig. 6-3(d-f), the electron density and complex optical dielectric constant distributions in ITO are very similar to those in the plasmonic device as shown in Fig. 6-3(d-f). The maximum residual ITO electron density at the center ($y = 0$) is $4.58 \times 10^{20} \text{ cm}^{-3}$, which is slightly higher than the corresponding value in the plasmonic device, as shown in Fig. 6-3(a), because the potential drop in the Si accumulation layer reduces the voltage applied across the HfO_2 layers.

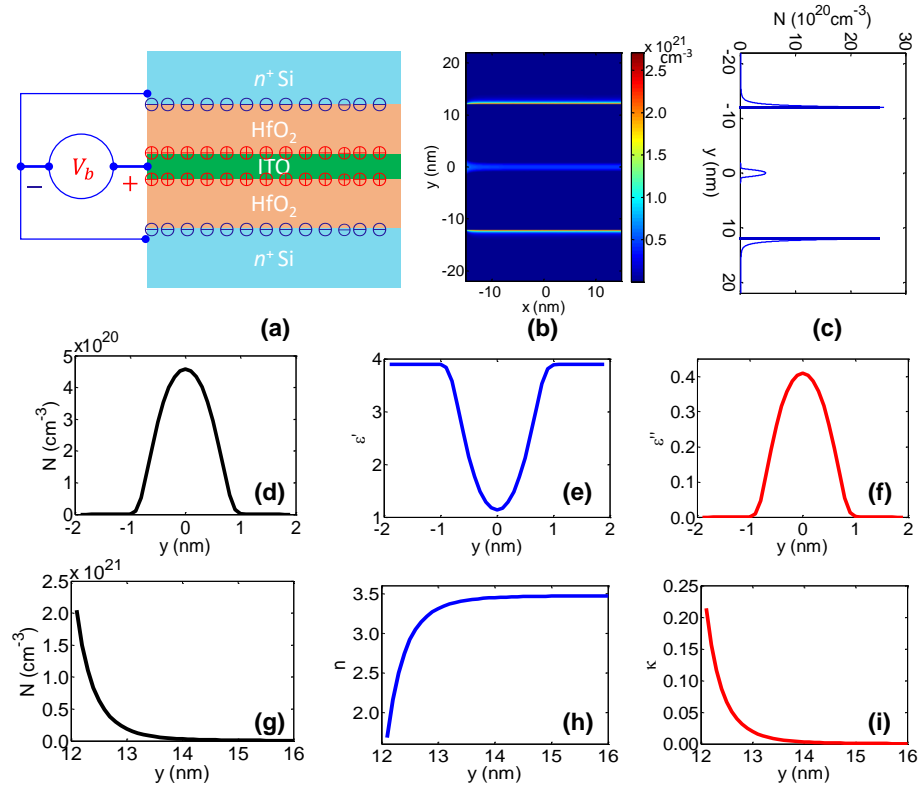


Figure 6-3. (a) Illustration of the Si-insulator-COx-insulator-Si structure working at the depletion mode. (b, c) FEM simulation of the residual electron distribution in the ITO film and accumulated electron distribution in Si. (d) The residual electron distribution in the ITO film. (e, f) The complex optical dielectric constant of ITO. (g) The accumulation electron distribution in the Si. (h, i) The complex refractive index of Si in the accumulation layer.

The accumulation electron distribution in Si is plotted in Fig. 6-3(g). The accumulated charge is distributed from above $2 \times 10^{21} \text{ cm}^{-3}$ at the surface decaying to $5 \times 10^{20} \text{ cm}^{-3}$ within 0.6 nm. The effect of the induced charge will result in index change, Δn , and absorption, α , which can be estimated according to Eqs. (1.10 & 1.11) when working wavelength is $\lambda_o = 1550 \text{ nm}$.

The corresponding complex refractive index of Si can be calculated according to

$$\begin{cases} n = n_o + \Delta n \\ \kappa = \frac{\alpha \lambda_o}{4\pi} \end{cases} \quad (6.1)$$

Figure 7-3(h, i) plots the complex refractive index, $n + j\kappa$, distribution of Si in the accumulation layer, where the refractive index of intrinsic Si $n_o = 3.476$ at $\lambda_o = 1550 \text{ nm}$ is assumed.

6.3 Performance analysis

To consider the field effect on light propagation, we first put the Au-sandwiched structure in a 3D plasmonic waveguide as shown in Fig. 6-4(a). The inset illustrates the coordinates used in this work. The modulators to be investigated are much more sensitive to TM polarization (with major E_y and H_x components). The TM polarization and working wavelength $\lambda_o = 1550 \text{ nm}$ are assumed throughout this work. As can be seen, the top and bottom Au layers are electrically connected to easily apply the bias. Any bias applied between the ITO and the bottom Au layer will be automatically applied between ITO and the top Au layer with the same value.

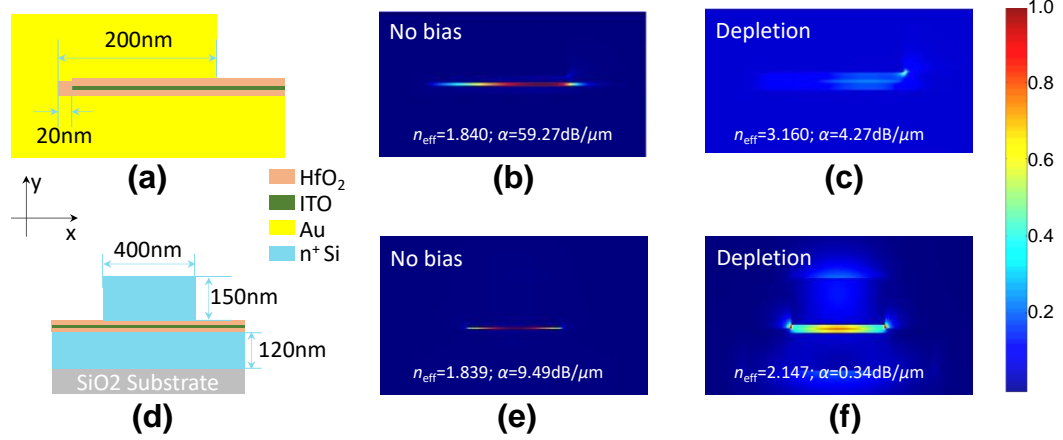


Figure 6-4. The electric field profiles ($|E(x, y)|$), effective indices, and propagation loss for different ITO-sandwiched waveguides in two cases: no bias and depletion. (a-c) In a plasmonic waveguide. (d-f) In a Si waveguide. The maximum field magnitude is normalized to be 1 in each plot. The refractive indices of Si, HfO₂, SiO₂, and Au are assumed to be 3.476, 2.070, 1.444, and 0.559+j9.81, respectively. The thickness of each HfO₂ layer is 10 nm, ITO thickness, 4 nm.

We assume without bias the optical dielectric constant of is $\epsilon_r(enz) = 0.0942 + j0.563$. Using a 3D mode solver based on the finite-difference time-domain (FDTD) method, we found the mode supported by the plasmonic waveguide. Figure 6-4(b) shows the mode profile ($|E(x, y)|$) when the ENZ ITO is sandwiched. As can be seen, very strong electric field is excited in the ENZ ITO film, which results in a very large attenuation $\alpha = 59.27$ dB/ μm . The effective index $n_{\text{eff}} = 1.840$ is considerably small because a large portion of power is concentrated in the low index ITO film. For the depletion case, we applied the complex dielectric constant of ITO as shown in Fig. 6-2(e, f) in the 3D mode solver. Figure 6-4(c) shows the corresponding mode profile, where the electric field and hence power distribution spread nearly the whole spacing between the two Au films. It is found that the attenuation reduces to $\alpha = 4.27$ dB/ μm and effective index increases to

$n_{\text{eff}} = 3.160$. In fact, most of the attenuation comes from the absorption by Au. The residual electrons in ITO only contribute ~ 0.5 dB/ μm attenuation. In the ITO film layer, a mesh size $dy = 0.1$ nm is applied in the y -direction when the 3D mode solver is used. Outside the ITO layer, $dx = 2$ nm, $dy = 0.5$ nm.

Similarly, we investigated the two operation modes when the ITO is sandwiched in a Si waveguide as shown in Fig. 6-4(d). Figure 6-4(e) shows the mode profile ($|E(x, y)|$) when the ENZ ITO is sandwiched. Figure 6-4(f) shows the mode profile ($|E(x, y)|$) when the depleted ITO is sandwiched. The complex dielectric constant of ITO shown in Fig. 6-3(e, f) and the refractive index of Si shown in Fig. 6-3(h, i) are applied in the depletion case. As can be seen, the waveguide attenuation reduces from 9.49 dB/ μm to 0.34 dB/ μm and effective index slightly increases from 1.839 to 2.147 when ITO is switched from ENZ to depletion state. In the ITO film and Si accumulation layers, a mesh size $dy = 0.1$ nm is applied in the y -direction when the 3D mode solver is used. Elsewhere, $dx = 4$ nm, $dy = 0.5$ nm.

In order to evaluate the insertion loss of the EA modulators, we did 3D FDTD simulation with the mesh size dx and dy as described in above text and $dz = 2$ nm. We first simulated the modulator based on the plasmonic waveguide platform as shown in Fig. 6-5(a). In the design, the modulator is embedded in a waveguide with the same configuration as itself except without the ITO layer. As a result, the input and output waveguides are two identical Au-HfO₂-Au waveguides, where the thickness of HfO₂ is 20 nm. The length of the EA modulator is 200 nm. Figures 6-5(b & c) show the power distribution in the waveguide in ENZ and depletion cases, respectively. Two detectors are placed 30 nm away

from the modulator to evaluate the input and output power flow in the z -direction. Simulation results demonstrate that the overall throughput is 12.7% for ENZ ITO, and 77.5% for depleted ITO. Note that the insertion loss is 1.11 dB (77.5%). The achievable extinction ratio is 7.86 dB.

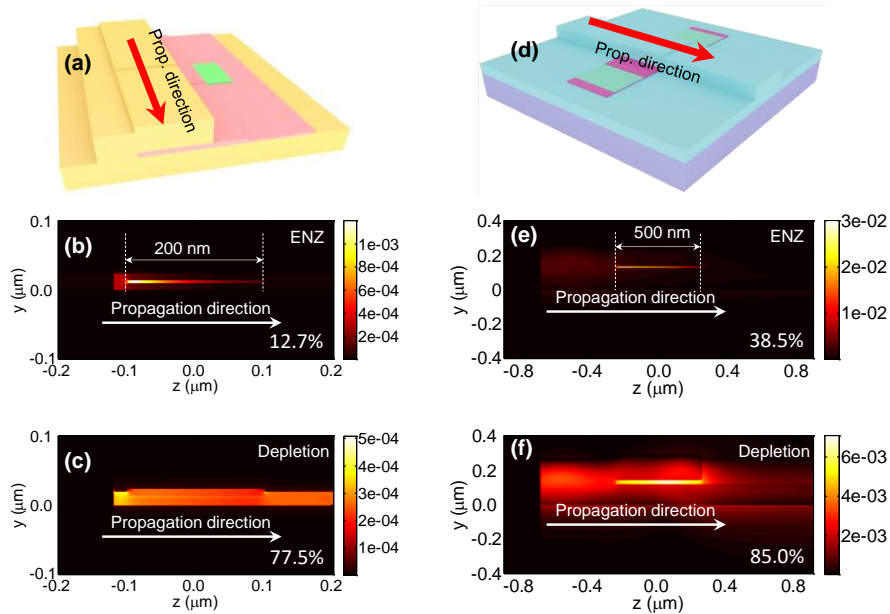


Figure 6-5. (a) The illustration of an EA modulator embedded in an Au-HfO₂-Au plasmonic waveguide. The cross-section dimensions of the modulator are shown in Fig. 3(a). (b, c) The 3D simulation of light propagation between the plasmonic waveguide and the EA modulator in ENZ and depletion cases, respectively. (d) The illustration of an EA modulator embedded on a rib Si waveguide. The cross-section dimensions of the modulator are shown in Fig. 3(d). (e, f) The 3D simulation of light propagation between the rib Si waveguide and the EA modulator in ENZ and depletion cases, respectively.

We also simulated the modulator based on the Si waveguide platform as shown in Fig. 6-5(d). The length of the EA modulator is 500 nm. In this case, the modulator is embedded in a Si waveguide with same overall dimensions as itself except without the ITO and HfO₂ layers. Figures 6-5(e & f) show the power distribution in the waveguide in ENZ and

depletion cases, respectively. Simulation results demonstrate that the overall throughput is 38.5% for ENZ ITO, and 85.0% for depleted ITO, which give rise to extinction ratio, 3.44 dB with insertion loss, 0.71 dB.

6.4 Discussion and conclusion

The optical bandwidth of the modulators can be over several THz due to the slow Drude dispersion [187]. The EA modulators can potentially work at an ultra-high speed, being mainly limited by the RC delay imposed by electric circuits. In spite of the involvement of double, thin high-k insulator layer, the parasitic capacitance of the EA modulators can still be very small owing to their nanoscale footprints. Thus, low energy consumption per bit is expected. The fabrication of 4-nm thick ITO may be challenging. There are two approaches to address this issue:

- (1) Multilayer 2D semiconductor with heavily doped carrier concentration. For example, 10 layers of graphene.
- (2) Material with even higher dielectric concentration. There were reports on perovskite-based dielectrics, BaTiO₃ with $\epsilon_r=165$ [210], and SrTiO₃ with $\epsilon_r=219$ [211] at room temperature.

There are three approaches to further improve the performance of the proposed EA modulators: (1) decreasing the ENZ film, (2) shrinking the insulator thickness, and (3) increasing the dielectric constant of the insulator.

To summarize, recent experiments show the potential applications of CO_x as tunable ENZ material. When sandwiched in a plasmonic or Si waveguide, a very thin ENZ film

can greatly enhance light absorption; whereas, the depletion of the carriers in the ENZ film can significantly reduce light absorption. The depletion of ultrathin ENZ film-sandwiched waveguides may enable EA modulation at the nanoscale. The successful development of this technique may lead to a significant breakthrough in on-chip optical interconnects.

7. ULTRA-COMPACT HIGH SPEED FIELD-EFFECT DIELECTRIC MODULATOR

In the previous chapters, based on the field effect (i.e. carrier accumulation and depletion) within active conductive oxide layer in the MIC and MICIM structures, we have experimentally demonstrated plasmonic EA modulators that have broadband EO response, ultra-compact footprint as well as potentially high operation speed. According to the numerical study of field-effect optical modulators based on ENZ-slot waveguide in Chapter. 3 & 6, we know that field-effect EA modulation can also be found in dielectric waveguide configurations. Compared with plasmonic modulator where light can propagate as surface plasmon polaritons (SPPs) at metal-dielectric surface, dielectric modulator would lose some compactness. However, it promises much easier integration with existing platforms based on CMOS technology. Besides, without metallic components, the optical losses will become much smaller. Thus, it is worthy of exploring an efficient and compact dielectric modulator.

7.1 Background

Since 2010 when the EO response of ITO inside an MIC structure was revealed [33], many works towards CO_x-based EO modulation have been proposed. However, most of the proposed modulators utilize plasmonic waveguide configurations. Few modulators integrated with dielectric materials have been reported [209, 212]. Zhao et al. reported their numerical study of a high-confinement Si slot-waveguide modulator (Fig. 7-1(a)), in which SiO₂ buffer layer and polysilicon cladding are used to confine EM fields within 10nm ITO

film [212]. They also investigated the integration of the slot-waveguide modulator with Si strip waveguides. In Ref. [83], Sorger et al. demonstrated an ITO-based nanophotonic modulator on SOI platform with a modulator length of 3λ (Fig. 7-1(b)), which can reach an extinction ratio of 1 dB/ μm over a wide bandwidth range. However, the broadband modulator is actually utilizing the field-effect in an MIC structure. The silicon substrate is mainly used as a waveguide for light interaction with the MIC modulator. Therefore, it is necessary to experimentally demonstrate the operation of a dielectric modulator to facilitate the development of COx-based EO modulators for future integrated photonic circuits.

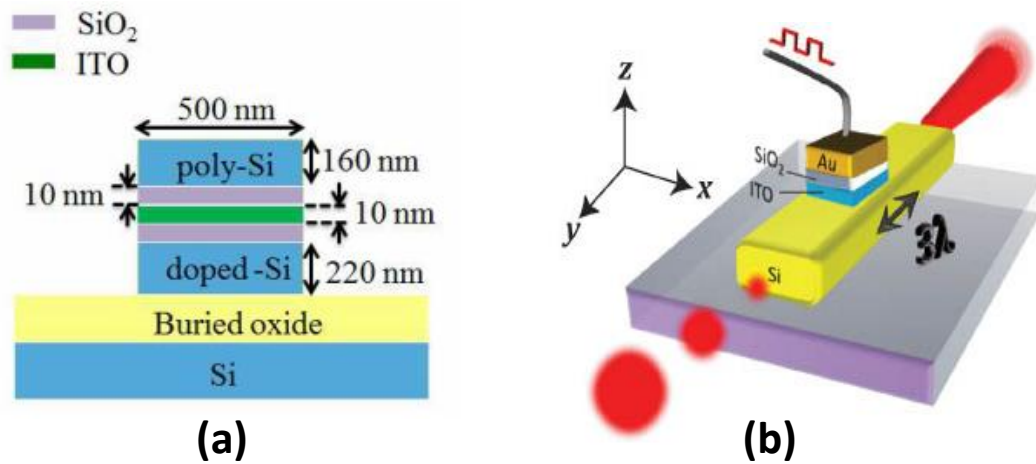


Figure 7-1. (a) The schematic of a high-confinement Si slot-waveguide modulator [212]. (b) An ITO-based nanophotonic modulator [83].

7.2 Design, modeling, and fabrication

The design of the COx-based dielectric modulator is shown in Fig. 7-2 (a). As can be seen, in this dielectric slot waveguide, TiO₂ will serve as the waveguide for guiding light to interact with ITO. ITO slot is embedded between TiO₂ waveguide and doped Si, and

again, high k material, HfO_2 is used as gate dielectric. External electric signals will be applied on doped Si and ITO, which stimulates the field effects in the active ITO layer on ITO- HfO_2 interface. Figure 7-2(b) illustrates the designed schematic for the device to be fabricated. The device will be fabricated on SOI substrate. In order to reduce optical losses and electrical resistance, only Si in the modulator region will be doped for applying electric signal. Besides, nickel silicide will be used to further reduce contact resistance on doped Si. Since the light coupling in the MICIM plasmonic modulator (Fig. 5-2(a)) through a lensed fiber and input/output slits is very poor, we utilize grating couplers for the dielectric modulator. Here, a TiO_2 waveguide with gratings on the two ends is used for light coupling and propagation, where the U-shaped is designed for convenient light coupling by using angled fiber arrays. Gold will only be used as contact pads in the device.

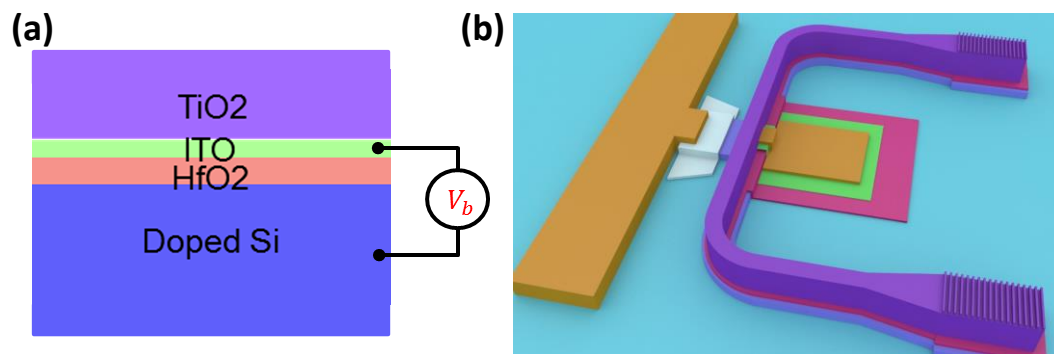


Figure 7-2. (a) The multi-layer stack of the dielectric modulator. (b) The 3D schematic of the modulator.

Preliminary modeling has been done for modulator based on dielectric ENZ-slot waveguide, showing greatly enhanced light absorption at ENZ state. Here, with the designed schematic, we model the whole device for both light coupling and modulation

performance. The center wavelength for device operation is set to be 1550 nm, where, according to FDTD solutions, the maximum light coupling efficiency can be achieved with the grating period of 1.4 μm and an incident angle of 28°.

From Fig. 7-3(a), we can see the schematic model of the device built in Lumerical FDTD solutions. The modulator is located at the center of the U-shaped waveguide. Over each grating coupler is an optical fiber for illuminating or receiving light. In the simulation, light transmission of the device under both original state ($\epsilon_{\text{ITO}} = 2.53 + j0.11$) and ENZ state ($\epsilon_{\text{ITO}} = 0.44 + j0.32$) are examined. For the 4- μm -long modulator, the output transmission has a peak value 25.5% for 1555 nm input light when ITO is at original state, and dramatically drops to less than 3% at ENZ state, as can be seen in Fig. 7-3(b). Therefore, it has been verified that the designed modulator has a moderate coupling efficiency. More importantly, significant light absorption can be expected if the device is working under ENZ condition.

Figure 7-3(c) illustrates the fabrication flow. Starting from 220 nm SOI wafer, the Si layer is first thinned to 120 nm, the designed thickness for Si. Wet oxide furnace growth is used to consume the undesired Si, and the grown thermal oxide then serves as the mask for doping Si layer in the modulator region by solid-source phosphorous diffusion. After stripping the oxide mask in the buffered oxide etch solution, undesired Si layer is removed by plasma etch. In order to optimize electrical contact on doped Si, a thin nickel film is deposited and then annealed by rapid thermal process (RTP) to form nickel silicide, which significantly decreases the resistance of electrical contact films. After that, similar to the plasmonic modulator, layer-by-layer deposition and liftoff processes are utilized to

fabricated the multi-layers of HfO₂ (ALD), ITO (sputter), TiO₂ (evaporation) as well as gold (evaporation). The SEM image of the fabricated device is shown in Fig. 7-3(c). The distance between two grating couplers is 127 μm, which matches the spacing of the fiber arrays. The modulator, located in the center of the U-shaped waveguide, is shown in the enlarged image. The modulator width is 1 μm, and the minimum designed modulator length is 4 μm. Therefore, the dielectric modulator has a very compact size of 4 μm².

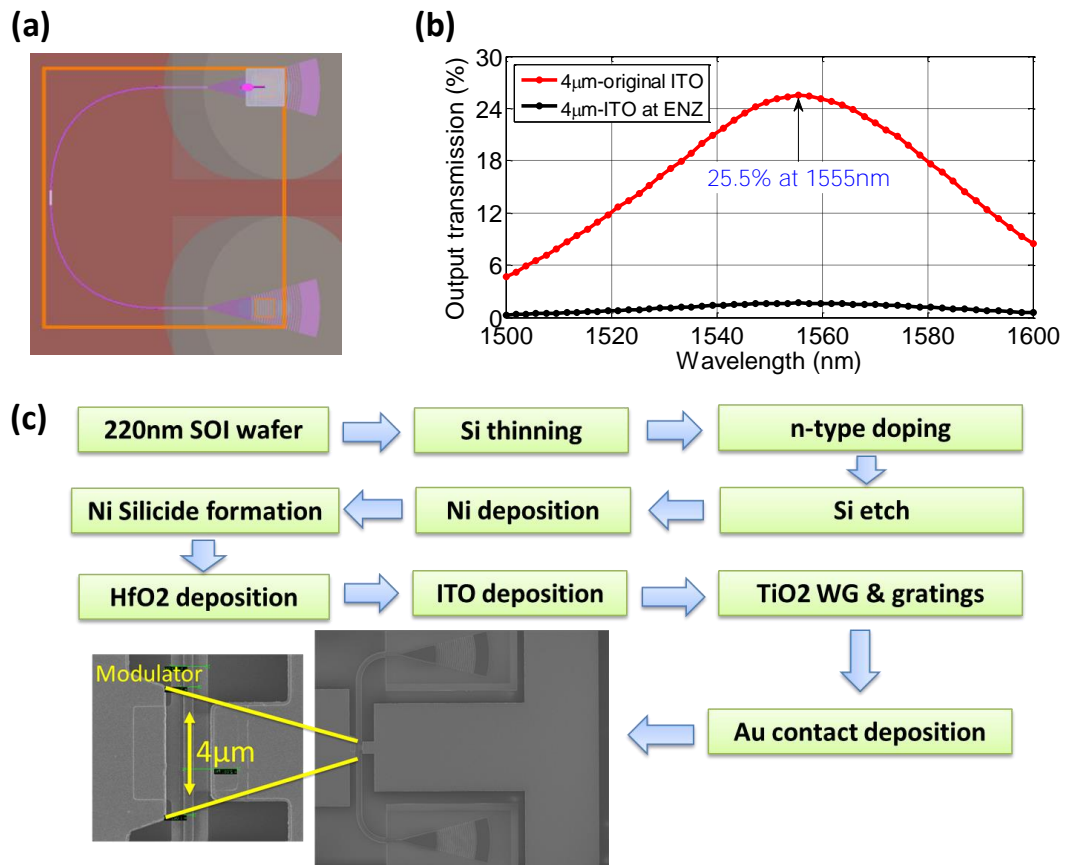


Figure 7-3. (a) The simulated device schematic in Lumerical FDTD solutions. (b) The output transmission of the modulator at original state and ENZ state. (c). Fabrication flow and SEM images of the device.

7.3 Light coupling and modulation measurement

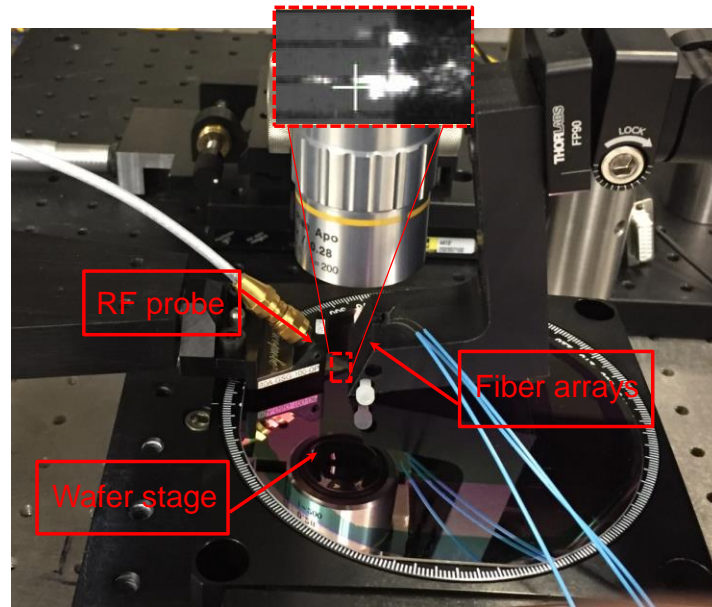


Figure 7-4. (a) Light coupling and modulation measurement setup.

The experimental setup for the light coupling and modulation measurement is depicted in Fig. 7-4. This is a whole-wafer test setup. A motorized wafer stage is used to hold as well as to precisely control the rotation of the 4-inch wafer. On the right side, four-channel angled fiber arrays are set above the devices for coupling light in and out. Note that as illustrated in the working principle (Chap. 3), the modulator can only work with TM-polarized light, so the input light from a tunable laser source (1260 nm to 1520 nm) will first go through polarization control before coupling into the device. The output light is fed into a photodiode which connects an oscilloscope or a spectrum analyzer to examine the light power and modulation response. On the left side is a GSG RF probe, which is paired with a function generator, and used for applying electrical signals on the contact pads of the devices. A microscope, installed with an NIR camera at the top through an adapter, is

placed over the device under test (DUT) for observation, alignment, and NIR imaging. From the inset of the figure, we can see an NIR camera picture showing light coupling in (bottom side) and out (top side) of the device.

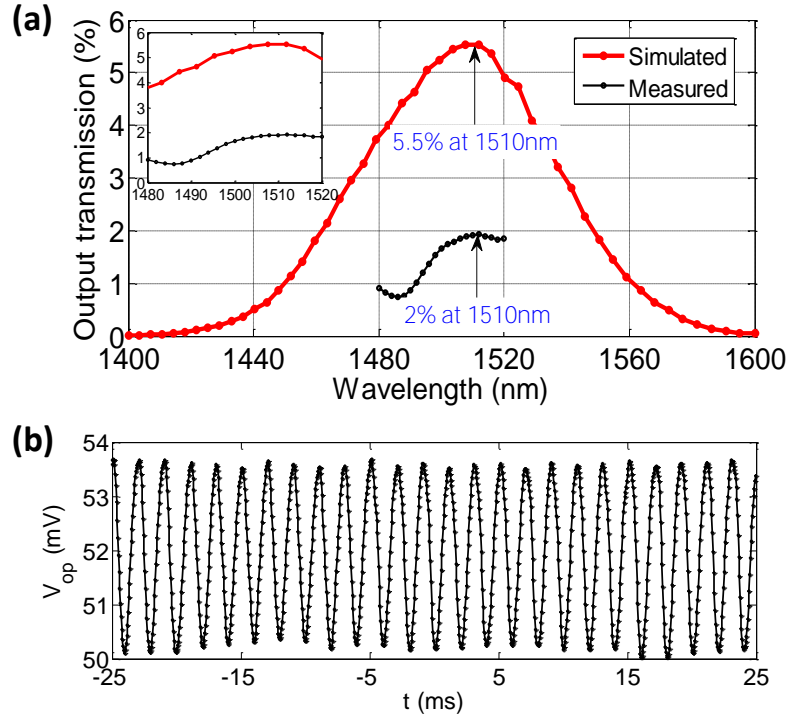


Figure 7-5. (a) Output transmission of the simulated device with updated parameters and the measured output transmission without external electric signal. (b) The output light power waveform of the modulator under a 500 Hz, 11V- V_{pp} electric signal.

Firstly, we investigate the coupling performance of the devices. Based on the measured parameters of the fabricated layers (film thickness, index, dimensional error), the FDTD simulation results are updated. As shown in Fig. 7-5(a), we obtain a peak 5.5% output transmission at the wavelength of 1510 nm. Due to the wavelength limitation in the laser source, we only plot measured coupling efficiency of the device in the range of 1480 nm

to 1520 nm, which shows a peak value of 2% at 1510 nm. From the inset, we can clearly see the simulation and test results match well except the magnitude of the efficiency, which, should be mainly caused by the fabrication and measurement imperfection. Note that the highly doped Si contributes to about 0.7% optical loss according to numerical simulation.

Then, with the setup set for maximum output transmission, an AC electric signal is applied on the DUT. With a DC-coupled photodiode (25 MHz bandwidth), the output light power is displayed on the oscilloscope. Figure 7-5(b) shows the output waveform of the DUT under a 500 Hz, 11V- V_{pp} sinusoidal electric signal, which verifies the EO modulation response. The measured extinction ratio is less than 1dB/ μm , which should be mainly due to fabrication imperfections.

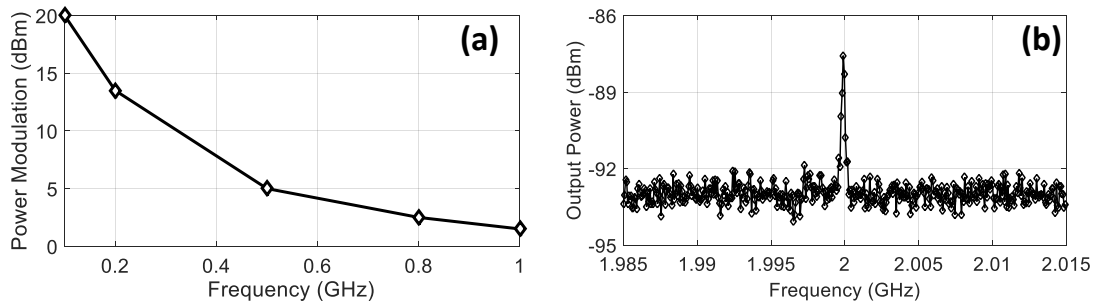


Figure 7-6. (a) Modulation depth versus frequency measured by a spectrum analyzer. (b) Spectrum analyzer measurement showing light intensity modulation at 2 GHz.

In order to investigate the operation speed of the dielectric modulator, an AC-coupled InGaAs photodiode with 10 GHz bandwidth is utilized. The output signal is then analyzed by a high speed (up to 13.2 GHz) spectrum analyzer, where an intensity peak can be

observed at certain modulating frequencies. Note that the measurements are taken under the optimum coupling condition ($\lambda = 1510$ nm). The amplitude of the peak represents the modulation depth. In Fig. 7-6(a), the modulation depth of the device under $11\text{V}-V_{pp}$ electric signal is plotted with respect to different modulating frequencies. Clearly, EA modulation at GHz has been successfully achieved. The modulation depth decays with increasing frequency, showing that the device has a RC circuit-limited operation speed. Specifically, we have achieved a modulation speed of up to 2 GHz, as shown in Fig. 7-6(b).

7.4 Circuit analysis

Due to the RC-limited operation speed exhibited in the dielectric modulator, an electric circuit model needs to be extracted to identify the limitation factors. Therefore, circuit analysis is conducted by measurement of reflection coefficient S_{11} of device circuit and curve fitting. A high speed (20 GHz) network analyzer is used for the measurement. The measured S_{11} data as a function of frequency is shown as black diamonds in Fig. 7-7. From the figure, the S_{11} value decreases to -2 dB at 3.2 GHz, which further verifies the RC-limited speed of the device. Note that the reflection coefficient bounces back after a certain frequency, indicating that there exists parasitic inductance in the device circuit. As a result, we treat the device as a simple RLC circuit shown in Fig. 7-7(a), where L is series inductance, C is gate dielectric capacitance, g is AC conductance, and R is series resistance of the substrate and metal contact. From the fitting curve, the circuit parameters are extracted as $L=108$ pH, $C=3.1$ pF, $R=6.2$ Ω , and $1/g=4.4$ k Ω . Therefore, the cutoff frequency can be estimated as $f_c=8.3$ GHz.

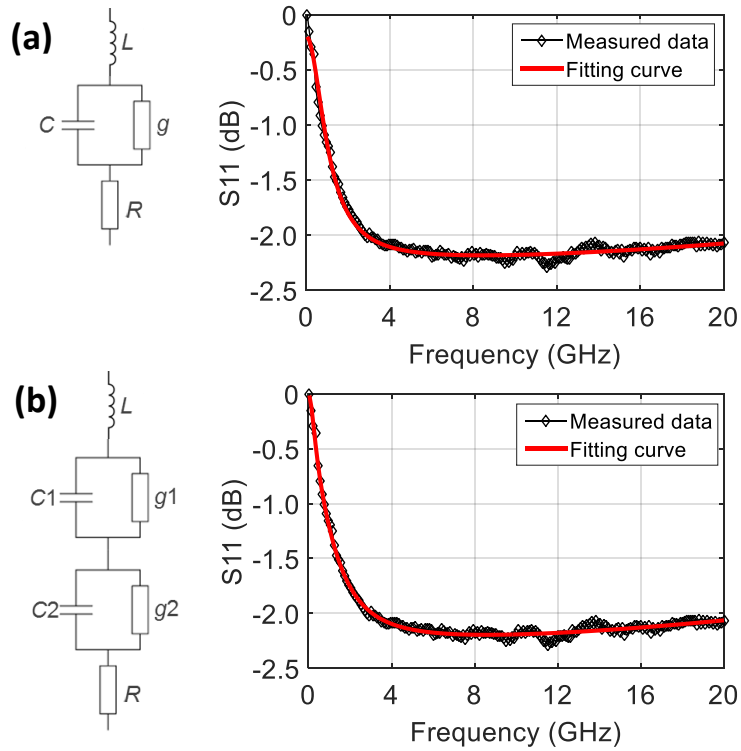


Figure 7-7. S_{11} measurement and curve fitting of (a) a simple RLC equivalent circuit model of the modulator and (b) a more complicated model.

As shown in Fig. 7-7(b), a more complicated circuit model, which takes the capacitance and conductance of the ITO layer into account, is also well fitted. Of course, the real circuit of the device should be much more complicated with many more components. We are still working on developing a realistic model to locate the key components that limit the device performance, and expect to achieve an operation speed of tens of GHz by optimizing the design and fabrication accuracy.

7.5 Conclusions

In conclusion, we have experimentally demonstrated a COx-based EA modulator integrated in a dielectric platform. The modulator has an ultra-compact footprint of $4 \mu\text{m}^2$.

Besides, it exhibits up to 2 GHz operation speed at telecommunication wavelengths, which is the first experimental illustration of GHz EO modulation based on CO_x materials. In this device, we have utilized the electrically-driven field effect in a doped semiconductor-insulator-CO_x structure, which is enhanced by high-k dielectric material. The involved fabrication processes are undemanding and CMOS-compatible. According to the circuit reflection analysis, the operation speed is mainly limited by circuit RC constant, which can be further optimized with better device design, improved material properties, and more accurate fabrication process. The modulation efficiency of this prototype dielectric modulator is also expected to be greatly enhanced with such optimization. The device provides a promising candidate for an ultra-compact and ultra-fast on-chip interconnect in future integrated photonic circuits.

8. CONCLUSIONS

In this dissertation, for the purpose of solving the bottleneck of lacking ultra-compact and ultra-fast EO modulators, two novel materials, graphene and conductive oxide, have been investigated, where enhanced light absorption by the two materials and its application in EO modulation has been studied and explored analytically, numerically and experimentally. The research topics covered in this dissertation concentrated on improving the performance of the devices by taking the advantages of the strong light-matter interaction in novel waveguiding platforms, such as introducing graphene-sandwiched structures for broadband enhanced light absorption, and utilizing ENZ effect and field effect for efficient and high-speed EA modulation in CO_x-based plasmonic/dielectric slot waveguides.

8.1 Enhanced light absorption by graphene

Chapter 3 explored the possibility of achieving greatly enhanced light absorption by graphene in a broad spectral range. Both monolayer and multi-layer graphene-based sandwiched structures have been examined. The fundamental study of the optical property of monolayer graphene has shown that greatly enhanced light absorption up to 42.7% could be achieved for TE polarized light from visible to NIR regime. Preliminary results of EO modulation by applying electrolyte gel in the graphene-based multilayer structure has also been demonstrated. **For multi-layer graphene, over 70% light absorption can be achieved for unpolarized light, and nearly 100% light absorption can be obtained at**

certain conditions. Such high absorption of the structure, together with many other exceptional properties of graphene, promise potential application in photovoltaics.

8.2 Field-effect optical modulation by conductive oxide

The work presented in Chapter 4, 5 and 7 focused on the investigation of COx as electrically tunable ENZ materials and its application in field-effect optical modulation. In Chapter 4, based on ENZ effect of COx in slot waveguide structures, greatly enhanced light absorption has been achieved, which promises nanoscale EA modulators with high efficiency and speed, low losses and easy fabrication. The significant optical property change of COx can also be utilized for laser beam steering.

Chapter 5 explored MIC EA modulators based on the theoretical study in Chapter 4. The investigation on the modulators has shown broadband EA modulation under DC biases. Light absorption of the MIC structure can be modulated by both carrier accumulation and depletion, and the observation leads to the conclusion of the modulation mechanism – field effect optical modulation. **The investigation of the tunable property of ITO verified its ENZ behavior in the MIC structure around telecom wavelengths.** The ENZ working region depends on ITO film properties, which can be tuned in the fabrication process.

Based on the observation and conclusion in Chapter 5, Chapter 7 theoretically studied the potential of carrier depletion of ENZ ITO in nanoscale EA modulators. The simulation results showed great promise, however, some problems remain to be solved in the experimental demonstration.

8.3 Ultra-compact and ultra-fast field effect EA modulators

Chapter 6 and 8 demonstrated the experimental verification and investigation of ultra-compact plasmonic and dielectric field effect EA modulators, respectively. In Chapter 6, by utilizing an MICIM structure, where the field effect is enhanced by the double capacitor gating, **the plasmonic modulator has an 800-nm long waveguide length, and can achieve an impressive extinction ratio of 3.04 dB/ μm .** The modulator can work up to 500 MHz according to the measurement, and is expected to achieve GHz operation with optimized design and test.

In Chapter 8, with the U-shaped waveguide and grating coupler design, **the doped Si-HfO₂-ITO dielectric modulator exhibited an operation speed of up to 2 GHz, which is the first experimental demonstration of GHz operation of CO_x-based EO modulators.** The speed is mainly limited by the RC constant of the device.

Both plasmonic and dielectric modulators based on CO_x show great promise for ultra-compact and ultra-fast EO modulators in future integrated photonic circuits. With optimization on device design, fabrication process and test setup, we expect efficient modulation at 10s of GHz within a nanoscale EA modulator.

8.4 Future work

The work presented in the dissertation is concentrated on the investigation of enhanced light absorption and its application in EA modulation. There is certainly a huge scope for further development on several aspects of the work. Below are some directions which could be followed up:

1). Graphene photodetector, which may be one of the potential applications of the significantly enhanced absorption by graphene presented in Chapter 2. The wavelength-independent absorption enables graphene to be used for a wide spectral range from ultraviolet to infrared. Actually, many graphene-based photodetectors have already been proposed with advantages of broadband photoresponse, high photoresponsivity as well as high operation speed [143,145,146]. Our research may provide simple and efficient structures for future photodetectors.

2). Graphene-based photovoltaics. The supreme properties of graphene make it capable of fulfilling multiple functions in photovoltaic devices: 1) transparent conductor window, 2) photoactive material, 3) channel for charge transport, and 4) catalyst. As transparent conducting electrodes, graphene can be used in organic, inorganic, as well as dye-sensitized solar cell devices. For example, with graphene electrodes obtained by different synthesis techniques, researchers have achieved power conversion efficiencies (PCEs) of 0.3% [213], 0.4% [214], 1.2% [215]. With multi-layer graphene, Jung et al have demonstrated a PCE of 2.68% [216]. By using graphene as the active material in photovoltaic devices, one can expect stronger light absorption and higher charge mobility with good stability. Researchers have reported over 1.5% PCE by utilizing graphene as acceptor in heterojunction organic solar cells [217]. Theoretically, up to 12% single-cell efficiency can be realized by graphene-based organic devices [218]. The optimization for better performance may rely on, but not limited to 1) increasing transparency while decreasing sheet resistance of graphene films, 2) effectively control of the work function, and 3) improvement of graphene miscibility to assure a good dispersion [219]. The enhanced

unpolarized light absorption over a broad solar spectrum realized by our proposed graphene-sandwiched structure may provide possibilities for improving PCE in future graphene-based photovoltaic devices. Of course, the utilization of the structure in the actual devices still needs investigation.

3). CO_x-based field effect EA modulators with high-k dielectrics. In Chapter 6 and 8, immense potential of both plasmonic and dielectric modulators have been shown. The strength of the field effect directly relates to the effective performance of the modulator. To further enhance the field effect, a new material with a comparable or even higher dielectric constant as well as CMOS-compatible is desirable. Recently reported perovskite-based dielectrics, BaTiO₃ with $\epsilon_r=165$ [210], and SrTiO₃ with $\epsilon_r=219$ [211] at room temperature, which can be grown by RF sputtering or ALD process, are viable alternatives for the gate dielectric. However, the increased capacitance induced by ultra-high dielectric constant of these materials may degrade the operation speed of the modulator devices, which should be considered in the future investigations.

Besides, other CO_x materials, such as AZO, GZO, and IGZO, can be investigated for EA modulation. GZO and AZO have shown similar ENZ effect as ITO in the telecom wavelength range, where the latter exhibit even smaller optical losses. IGZO has shown extraordinary performance in thin-film transistors (TFT) [220]. It is worthwhile to further explore its optical absorption and EO properties.

9. REFERENCES

1. S. O. Kasap, *Optoelectronics and photonics: principles and practices*, 2nd ed., Prentice Hall, 2013.
2. P. N. Prasad, *Nanophotonics*, John Wiley & Sons, Inc., 2004.
3. M. I. Stockman, “Nanoplasmonics: past, present, and glimpse into future,” *Opt. Expr.*, **19**, 22029–22106(2011).
4. G. T. Reed, G. Mashanovich, F. Y. Gardes, and D. J. Thomson, “Silicon optical modulators,” *Nat. Photon.* **4**, 518–526 (2010).
5. B. G. Lee, A. Biberman, J. Chan, and K. Bergman, “High-performance modulator and switches for silicon photonic networks-on-chip,” *IEEE J. Sel. Top. Quantum Electron.* **16**, 6–22 (2010).
6. A. Liu, R. Jones, L. Liao, D. Samara-Rubio, D. Rubin, O. Cohen, R. Nicolaescu, and M. Paniccia, “A high-speed silicon optical modulator based on a metal-oxide-semiconductor capacitor,” *Nature* **427**, 615–618 (2004).
7. Q. Xu, B. Schmidt, S. Pradhan, and M. Lipson, “Micrometre-scale silicon electro-optic modulator,” *Nature* **435**, 325–327 (2005)
8. R. S. Jacobsen, K. N. Andersen, R. I. Borel, J. Fage-Pedersen, L. H. Frandsen, O. Hansen, M. Kristensen, A. V. Lavrinenko, G. Moulin, H. Ou, C. Peucheret, B. Zsigri, and A. Bjarklev, “Strained silicon as a new electro-optic material,” *Nature* **441**, 199–202 (2006)
9. Q. Xu, S. Manipatruni, B. Schmidt, J. Shakya, and M. Lipson, “12.5 Gbit/s carrier-injection-based silicon microring silicon modulators,” *Opt. Express* **15**, 430–436 (2007)
10. L. Alloatti, D. Korn, R. Palmer, D. Hillerkuss, J. Li, A. Barklund, R. Dinu, J. Wieland, M. Fournier, J. Fedeli, H. Yu, W. Bogaerts, P. Dumon, R. Baets, C. Koos, W. Freude, and J. Leuthold, “42.7 Gbit/s electro-optic modulator in silicon technology,” *Opt. Express* **19**, 11841–11851 (2011).

11. A. Yariv and P. Yeh, *Photonics: Optical Electronics in Modern Communications*, 6th ed., Chap. 9, Oxford University, 2006.
12. E. L. Wooten, K. M. Kissa, A. Yan, E. J. Murphy, D. A. Lafaw, P. F. Hallemeier, D. Maack, D. V. Attanasio, D. J. Fritz, G. J. McBrien, and D. E. Bossi, “A review of lithium niobate modulators for fiber-optic communication systems,” *IEEE J. Sel. Top. Quantum Electron.* **6**, 69–82 (2000).
13. J. Teng, P. Dumon, W. Bogaerts, H. Zhang, X. Jian, X. Han, M. Zhao, G. Morthier, and R. Baets, “Athermal silicon-on-insulator ring resonators by overlaying a polymer cladding on narrowed waveguides,” *Opt. Express* **17**, 14627–14633 (2009).
14. B. Guha, B. B. C. Kyotoku, and M. Lipson, “CMOS-compatible athermal silicon microring resonators,” *Opt. Express* **18**, 3487–3493 (2010).
15. Y.-H. Kuo, Y. Lee, Y. Ge, S. Ren, J. E. Roth, T. I. Kamins, D. A. B. Miller, and J. S. Harris, “Strong quantum-confined Stark effect in germanium quantum-well structures on silicon,” *Nature* **437**, 1334–1336 (2005).
16. F. G. Della Corte, S. Rao, M. A. Nigro, F. Suriano, and C. Summonte, “Electro-optically induced absorption in α -Si:H/ α -SiCN waveguiding multistacks,” *Opt. Express* **16**, 7540–7550 (2008).
17. J. Liu, M. Baels, A. Pomerene, S. Bernardis, R. Sun, J. Cheng, L. C. Kimerling, and J. Michel, “Waveguide-integrated, ultralow-energy GeSi electro-absorption modulators,” *Nat. Photon.* **2**, 433–437 (2008).
18. H.-W. Chen, Y. H. Kuo, and J. E. Bowers, “25 Gb/s hybrid silicon switch using a capacitively loaded traveling wave electrode,” *Opt. Express* **18**, 1070–1075 (2010).
19. Y. Rong, Y. Ge, Y. Huo, M. Fiorentino, M. R. T. Tan, T. I. Kamins, T. J. Ochalski, G. Huyet, and J. S. Harris, “Quantum-confined Stark effect in Ge/SiGe quantum wells on Si,” *IEEE J. Sel. Top. Quantum Electron.* **16**, 85–92 (2010).
20. J. A. Dionne, K. Diest, L. A. Sweatlock, and H. A. Atwater, “PlasMOSor: A metal-oxide-Si field effect plasmonic modulator,” *Nano Lett.* **9**, 897–902 (2009).

21. K. S. Novoselov, A. K. Geim, S. V. Morozov, D. Jiang, Y. Zhang, S. V. Dubonos, I. V. Grigorieva, and A. A. Firsov, “Electric field effect in atomically thin carbon films,” *Science* **306**, 666–669 (2004).
22. K. S. Novoselov, A. K. Geim, S. V. Morozov, D. Jiang, M. I. Katsnelson, I. V. Grigorieva, S. V. Dubonos, and A. A. Firsov, “Two-dimensional gas of massless Dirac fermions in graphene,” *Nature* **438**, 197–200 (2005).
23. Y.-M. Lin, C. Dimitrakopoulos, K. A. Jenkins, D. B. Farmer, H.-Y. Chiu, A. Grill, and Ph. Avouris, “100-GHz transistors from wafer-scale epitaxial graphene,” *Science* **327**, 662 (2010).
24. X. Du, I. Skachko, A. Barker, and E. Y. Andrei, “Approaching ballistic transport in suspended graphene,” *Nat. Nanotechnol.* **3**, 491–495 (2008).
25. A. K. Geim and K. S. Novoselov, “The rise of graphene,” *Nat. Mater.* **6**, 183–191 (2007).
26. A. A. Balandin, S. Ghosh, W. Bao, I. Calizo, D. Teweldebrhan, F. Miao, and C. N. Lau, “Superior thermal conductivity of single-layer graphene,” *Nano Lett.* **8**, 902–907 (2008).
27. F. Bonaccorso, Z. Sun, T. Hasan, and A. C. Ferrari, “Graphene photonics and optoelectronics,” *Nat. Photon.* **4**, 611–622(2010).
28. R. R. Nair, P. Blake, A. N. Grigorenko, K. S. Novoselov, T. J. Booth, T. Stauber, N. M. R. Peres, and A. K. Geim, “Fine structure constant defines visual transparency of graphene,” *Science* **320**, 1308 (2008).
29. F. Xia, T. Mueller, Y.-M. Lin, A. Valdes-Garcia, and P. Avouris, “Ultrafast graphene photodetector,” *Nat. Nanotechnol.* **4**, 839–843 (2009).
30. F. Wang, Y. Zhang, C. Tian, C. Girit, A. Zettl, M. Crommie, and Y. R. Shen, “Gate-variable optical transitions in graphene,” *Science* **320**, 206–209 (2008).
31. D. R. Andersen, “Graphene-based long-wave infrared TM surface plasmon modulator,” *J. Opt. Soc. Am. B* **27**, 818–823 (2010).
32. M. Liu, X. Yin, E. Ulin-Avila, B. Geng, T. Zentgraf, L. Ju, F. Wang, and X. Zhang, “A graphene-based broadband optical modulator,” *Nature* **474**, 64–67 (2011).

33. E. Feigenbaum, K. Diest, and H. A. Atwater, "Unity-Order Index Change in Transparent Conducting Oxides at Visible Frequencies," *Nano Lett.*, **10**, 2111-2116(2010).
34. P. F. Robusto and R. Braunstein, "Optical Measurements of the Surface Plasmon of Indium-Tin Oxide," *Phys. Stat. Sol.* **119**, 115-168(1990).
35. C. Rhodes, S. Franzen, J. Maria, M. Losego, D. N. Leonard, B. Laughlin, G. Duscher, and S. Weibel, "Surface plasmon resonance in conducting metal oxides," *J. Appl. Phys.* **100**, 054905(2006).
36. F. Michelotti, L. Dominici, E. Descrovi, N. Danz, and F. Menchini, "Thickness dependence of surface plasmon polariton dispersion in transparent conducting oxide films at 1.55 μm ," *Opt. Lett.* **34**, 839-841(2009).
37. M. Fukuda, *Optical Semiconductor Devices*, John Wiley & Sons, Inc., 1999.
38. B. E. A. Saleh, M. C. Teich, *Fundamentals of Photonics*, second edition, John Wiley & Sons, Inc., 2007.
39. D. Miller, D. Chemla, T. Damen, T. Wood, C. Burrus JR., A. Gossard, and W. Wiegmann, "The quantum well self-electrooptic effect device: Optoelectronic Bistability and Oscillation, and self-linearized modulation," *IEEE J. Quantum Electron.*, **21**, 1462-1476(1985).
40. G. W. Wen, J. Y. Lin, H. X. Jiang, and Z. Chen, "Quantum-confined Stark effects in semiconductor quantum dots," *Phys. Rev. B* **52**, 5913(1995).
41. F. J. Blatt, *Physics of Electronic Conduction in Solids*, Mc Graw-Hill Book Company, 1968.
42. R. A. Soref and B. R. Bennett, "Electrooptical Effects in Silicon," *IEEE J. Quantum Electron.*, **23**, 123-129(1987).
43. K. Liu, C. Ye, S. Khan, and V. J. Sorger, "Review and perspective on ultrafast wavelength-size electro-optic modulators," *Las. Photon. Rev.* **9**, 172-194(2015).
44. Z. Y. Li, D. X. Xu, W. R. McKinnon, S. Janz, J. H. Schmid, P. Cheben, and J. Z. Yu, "Silicon waveguide modulator based on carrier depletion in periodically interleaved PN junctions," *Opt. Exp.* **17**, 15947-15958 (2009).

45. H. Xu, X. Xiao, X. Li, Y. Hu, Z. Li, T. Chu, Y. Yu, and J. Yu, "High speed silicon Mach-Zehnder modulator based on interleaved PN junctions," *Opt. Exp.* **20**, 15093–15099 (2012).
46. H. Yu, M. Pantouvaki, J. Van Campenhout, D. Korn, K. Komorowska, P. Dumon, Y. Li, P. Verheyen, P. Absil, L. Alloatti, D. Hillerkuss, J. Leuthold, R. Baets, and W. Bogaerts, "Performance tradeoff between lateral and interdigitated doping patterns for high speed carrier-depletion based silicon modulators," *Opt. Exp.* **20**, 12926–12938 (2012).
47. S. L. Chuang, *Physics of Optoelectronic Devices*, John Wiley & Sons, Inc., 1995
48. J. Kondo, A. Kondo, K. Aoki, M. Imaeda, T. Mori, Y. Mizuno, S. Takatsuji, Y. Kozuka, O. Mitomi and M. Minakata, "40-Gb/s X-cut LiNbO₃ optical modulator with two-step backslot structure," *J. of Lightwave Tech.*, **20**, 2110-2114(2002).
49. V. R. Almeida, C. A. Barrios, R. R. Panepucci and M. Lipson, "All-optical control of light on a silicon chip," *Nature*, **431**, 1081-1084(2004).
50. K. Kidoo Lee, "Transmission and routing of optical signals in on-chip waveguides for silicon microphotronics," PhD thesis, Massachusetts Institute of Technology, 2001.
51. G. T. Reed, G. Mashanovich, F. Y. Gardes, and D. J. Thomson, "Silicon optical modulators," *Nat. Photon.* **4**, 518-526(2010).
52. E. Timurdogan, C. M. Sorace-agaskar, J. Sun, E. S. Hosseini, A. Biberman, and M. R. Watts, "An ultralow power athermal silicon modulator," *Nat. Commun.* **5**, 1–11 (2014).
53. D. A. B. Miller, D. S. Chemla, T. C. Damen, A. C. Gossard, W. Wiegmann, T. H. Wood and C. A. Burrus, "Band-edge electroabsorption in quantum well structures: the quantum-confined Stark effect," *Phys. Rev. Lett.*, **53**, 2173-2176(1984).
54. B. R. Bennett and R. A. Soref, "Electrorefraction and Electroabsorption in InP, GaAs, GaSb, InAs and InSb," *IEEE Journal of Quantum Electronics*, **23**, 2159-2166(1987).

55. M. Salib, L. Liao, R. Jones, M. Morse, A. S. Liu, D. Samara-Rubio, D. Alduino, M. Paniccia, "Silicon Photonics," *Intel Technology Journal*, **8**, 143-160(2004).
56. R. Nagarajan, C. H. Joyner, R. P. Schneider, Jr., Jeffrey S. Bostak, T. Butrie, A. G. Dentai, V. G. Dominic, P. W. Evans, M. Kato, M. Kauffman, D. J. H. Lambert, S. K. Mathis, A. Mathur, R. H. Miles, M. L. Mitchell, M. J. Missey, S. Murthy, A. C. Nilsson, F. H. Peters, S. C. Pennypacker, J. L. Pleumeekers, R. A. Salvatore, R. K. S., R. B. Taylor, H. S. Tsai, M. F. Van Leeuwen, J. Webjorn, M. Ziari, D. Perkins, J. Singh, S. G. Grubb, M. S. Reffie, D. G. Mehuys, F. A. Kish and D. F. Welch, "Large-Scale Photonic Integrated Circuits," *IEEE Journal of Selected Topics in Quantum Electronics*, **11**, 50-64(2005)
57. J. Luo and A. K.-Y. Jen, "Highly efficient organic electrooptic materials and their hybrid systems for advanced photonic devices," *IEEE J. Selected Topics in Quantum Electron.* **19**, 3401012(2013).
58. V. E. Babicheva, A. Boltasseva, and A. V. Lavrinenko, "Transparent conducting oxides for electro-optical plasmonic modulators," *Nanophotonics*, **4**, 165-185(2015).
59. A. Melikyan, L. Alloatti, A. Muslija, D. Hillerkuss, P.C Schindler, J. Li, R. Palmer, D. Korn, S. Muehlbrandt, D. Van Thourhout, B. Chen, R. Dinu, M. Sommer, C. Koos, M. Kohl, W. Freude, and J. Leuthold, "High-speed plasmonic phase modulators," *Nature Photonics*, **8**, 229-233(2014).
60. C. Haffner, W. Heni, Y. Fedoryshyn, J. Niegemann, A. Melikyan, D. L. Elder, B. Baeuerle, Y. Salamin, A. Josten, U. Koch, C. Hoessbacher, F. Ducry, L. Juchli, A. Emboras, D. Hillerkuss, M. Kohl, L. R. Dalton, C. Hafner, and J. Leuthold, "All-plasmonic Mach-Zehnder modulator enabling optical high-speed communication at the microscale," *Nat. Photon.* **9**, 525-528(2015).
61. K. I. Bolotin, K. J. Sikes, Z. Jiang, M. Klima, G. Fudenberg, J. Hone, P. Kim, and H. L. Stormer, "Ultrahigh electron mobility in suspended graphene," *Sol. Sta. Commun.*, **146**, 351-355(2008).

62. T. Kampfrash, L. Perfetti, F. Schapper, C. Frischkorn, and M. Wolf, "Strongly coupled optical phonons in the ultrafast dynamics of the electronic energy and current relaxation in graphite," *Phys. Rev. Lett.* **95**, 187403(2005).
63. S. Y. Zhou, G.-H. Gweon, J. Graf, A. V. Fedorov, C. D. Spataru, R. D. Diehl, Y. Kopelevich, D.-H. Lee, S. G. Louie, and A. Lanzara, "First direct observation of Dirac fermions in graphite," *Nature Physics*, **2**, 595-599(2006).
64. K. F. Mak, M. Y. Sfeir, Y. Wu, C. H. Lui, J. A. Misewich, and T. F. Heinz, "Measurement of the optical conductivity of graphene," *Phys. Rev. Lett.* **101**, 196405(2008).
65. H. Li, Y. Anugrah, S. J. Koester, and M. Li, "Optical absorption in graphene integrated on silicon waveguides," *Appl. Phys. Lett.* **101**, 111110(2012).
66. K. S. Kim, Y. Zhao, H. Jang, S. Y. Lee, J. M. Kim, K. S. Kim, J.-H. Ahn, P. Kim, J.-Y. Choi, and B. H. Hong, "Large-scale pattern growth of graphene films for stretchable transparent electrodes," *Nature*, **457**, 706-710(2009).
67. S. Bae, H. Kim, Y. Lee, X. Xu, J.-S. Park, Y. Zheng, J. Balakrishnan, T. Lei, H. R. Kim, Y. Song, Y.-J. Kim, K. S. Kim, B. Özyilmaz, J. H. Ahn, B. H. Hong and S. Lijima, "Roll-to-roll production of 30-inch graphene films for transparent electrodes," *Nat. Nanotechnol.* **5**, 574-578(2010).
68. Z. Lu, and W. Zhao, "Nanoscale electro-optic modulators based on graphene-slot waveguides," *JOSAB*. **29**, 1490-1496(2012).
69. I. Hamberg and C. G. Granqvist, "Evaporated Sn-doped In₂O₃ films: Basic optical properties and applications to energy-efficient windows," *J. Appl. Phys.*, **60**, R123-R159(1986).
70. R. G. Gordon, "Criteria for Choosing Transparent Conductors," *MRS Bull.*, **25**, 52-57(2000).
71. T. J. Coutts, D. L. Young, and X. Li, "Characterization of Transparent Conducting Oxides," *MRS Bull.*, **25**, 58-65(2000).
72. J. Hotovy, J. Hupkes, W. Bottler, E. Marins, L. Spiess, T. Kups, V. Smirnov, I. Hotovy, and J. Kovac, "Sputtered ITO for application in thin-film silicon solar cells:

- relationship between structural and electric properties," *Appl. Surf. Sci.*, **269**, 81-87(2013).
73. P. R. West, S. Ishii, G. Naik, N. Emani, V.M. Shalaev, and A. Boltasseva, "Searching for better plasmonic materials," *Laser & Photonics Reviews* **4**, 795-808 (2010).
74. G. Naik, V.M. Shalaev, A. Boltasseva, "Alternative plasmonic materials: beyond gold and silver," *Advanced Materials* **25**, 3264–3294 (2013).
75. H. Kim, M. Osofsky, S. M. Prokes, O. J. Glembocki, and A. Pique, Optimization of Al-doped ZnO films for low loss plasmonic materials at telecommunication wavelengths, *Appl. Phys. Lett.* **102**, 171103 (2013).
76. P. F. Robusto and R. Braunstein, "Optical Measurements of the Surface Plasmon of Indium-Tin Oxide," *Phys. Stat. Sol.*, **119**, 115-168(1990).
77. C. Rhodes, S. Franzen, J. Maria, M. Losego, D. N. Leonard, B. Laughlin, G. Duscher, and S. Weibel, "Surface plasmon resonance in conducting metal oxides," *J. Appl. Phys.* **100**, 054905(2006).
78. F. Michelotti, L. Dominici, E. Descrovi, N. Danz, and F. Menchini, "Thickness dependence of surface plasmon polariton dispersion in transparent conducting oxide films at 1.55 μm ," *Opt. Lett.*, **34**, 839-841(2009).
79. Kevin Santiago, Rajeh Mundle, Chandan B. Samantaray, M. Bahoura, and A. K. Pradhan, "Nanopatterning of atomic layer deposited Al:ZnO films using electron beam lithography for waveguide applications in the NIR region," *Opt. Mater. Expr.* **2**, 1743-1750 (2012)
80. Guillermo Garcia et al, "Dynamically Modulating the Surface Plasmon Resonance of Doped Semiconductor Nanocrystals", *Nano Lett.*, **11**, 4415–4420 (2011).
81. G. V. Naik, J. Liu, A. V. Kildishev, V. M. Shalaev, A. Boltasseva, "Demonstration of Al:ZnO as a plasmonic component of near- infrared metamaterials," *Proceedings of the National Academy of Sciences* **109**, 8834-8838 (2012).

82. Y. Zhang, T. Wei, W. Dong, C. Huang, K. Zhang Y. Sun, X. Chen, and N. Dai, "Near-perfect infrared absorption from dielectric multilayer of plasmonic aluminum-doped zinc oxide." *Appl. Phys. Lett.* **102**, 213117 (2013).
83. V. J. Sorger, N. D. Lanzillotti-Kimura, R. M. Ma, and X. Zhang, "Ultra-compact silicon nanophotonic modulator with broadband response," *Nanophotonics*, **1**, 17-22(2012).
84. V.E. Babicheva, N. Kinsey, G.V. Naik, M. Ferrera, A.V. Lavrinenko, V.M. Shalaev, A. Boltasseva, "Towards CMOS-compatible nanophotonics: Ultra-compact modulators using alternative plasmonic materials," *Optics Express* **21**, 27326-27337 (2013)
85. W. Cai, J. S. White, and M. L. Brongersma, "Compact, high-speed and power-efficient electrooptic plasmonic modulators," *Nano. Lett.* **9**, 4403 (2009).
86. M. Koshino, and T. Ando, Electronic properties of monolayer and multilayer graphene, Chapter 6 in *Physics of Graphene, nanoscience and technology*, Springer 2014.
87. J. W. McClure, "Diamagnetism of Graphite," *Physical Review*, **104**, 666-671(1956).
88. G. W. Semenoff, "Condensed-matter simulation of a three-dimensional anomaly," *Physical Review Letter*, **53**, 2449(1984).
89. K. M. F. Shahil, A. A. Balandin, "Thermal properties of graphene and multilayer graphene: application in thermal interface materials," *Solid state communications*, **152**, 1331(2012).
90. X. Shen, Z. Wang, Y. Wu, X. Liu, Y. He, and J. K. Kim, "Multilayer graphene enables higher efficiency in improving thermal conductivities of graphene/epoxy composites," *Nano Lett.*, **16**, 3585(2016).
91. A. Krajewska, I. Pasternak, G. Sobon, J. Sotor, ..., and W. Strupinski, "Fabrication and application of multi-layer graphene stack on transparent polymer," *Appl. Phys. Lett.* **110**, 041907(2017).
92. E. McCann, M. Koshino, "Landau level degeneracy and quantum Hall effect in graphite bilayer," *Rep. Prog. Phys.* **76**, 056503 (2013).

93. B. Partoens, F.M. Peeters, “Normal and Dirac fermions in graphene multilayers: Tight-binding description of the electronic structure,” *Phys. Rev. B* **75**, 193402 (2007).
94. Y. Yu, Z. Li, W. Wang, X. Guo, J. Jiang, H. Nan, and Z. Ni, “Investigation of multilayer domains in large-scale CVD monolayer graphene by optical imaging,” *Journal of Semiconductors*, **38**, 033003(2017).
95. S. Latil and L. Henrard, “Charge carriers in few-layer graphene films,” *Phys. Rev. Lett.* **97**, 036803 (2006).
96. J. Hass, F. Varchon, J. E. Millaín-Otoya, M. Sprinkle, N. Sharma, W. A. de Heer, C. Berger, P. N. First, L. Magaud, and E. H. Conrad, “Why Multilayer Graphene on 4H-SiC(000 $\bar{1}$) Behaves Like a Single Sheet of Graphene,” *Phys. Rev. Lett.*, **100**, 125504(2008).
97. D. R. Kammler, T. O. Mason, D. L. Young, K. R. Poepelmeier, and D. L. Williamson, “Comparison of thin film and bulk forms of the transparent conducting oxide solution $Cd_{1+x}In_{2-2x}Sn_xO_4$,” *J. of Appl. Phys.* **90**, 5979(2001).
98. S. Zhu, G. Q. Lo, and D. L. Kwong, "Design of an ultra-compact electro-absorption modulator comprised of a deposited TiN/HfO₂/ITO/Cu stack for CMOS backend integration," *Opt. Express* **22**, 17930-17947 (2014).
99. J. Gwamuri, A. Vora, R. Khanal, A. Phillips, M. Heben, D. Guney, P. Bergtrom, A. Kulkarni, and J. Pearce, “Limitations of ultra-thin transparent conducting oxides for integration into plasmonic-enhanced thin-film solar photovoltaic devices,” *Mater. Renew Sustain Energy*, **4**:12 (2015).
100. A. K. Geim, “Graphene: status and prospects,” *Science*, **324**, 1530–1534(2009).
101. J. Hass, W. A. De Heer, and E. H. Conrad, “The growth and morphology of epitaxial multilayer graphene,” *Journal of Physics Condensed Matter*, **20**, 323202(2008).
102. K. V. Emtsev, A. Bostwick, K. Horn et al., “Towards wafer-size graphene layers by atmospheric pressure graphitization of silicon carbide,” *Nature Materials*, **8**, 203-207(2009).

103. Q. Yu, J. Lian, S. Siriponglert, H. Li, Y. P. Chen, and S.-S. Pei, "Graphene segregated on Ni surfaces and transferred to insulators," *Applied Physics Letters*, **93**, 113103(2008).
104. X. Li, W. Cai, J. An et al., "Large-area synthesis of high-quality and uniform graphene films on copper foils," *Science*, **324**, 5932, 1312–1314(2009).
105. X. Li, C. W. Magnuson, A. Venugopal et al., "Graphene films with large domain size by a two-step chemical vapor deposition process," *Nano Letters*, **10**, 4328–4334(2010).
106. S. Lee, K. Lee, and Z. Zhong, "Wafer scale homogeneous bilayer graphene films by chemical vapor deposition," *Nano Letters*, **10**, 4702–4707(2010).
107. N. Zhan, M. Olmedo, G. Wang, and J. Liu, "Layer-by-layer synthesis of large-area graphene films by thermal cracker enhanced gas source molecular beam epitaxy," *Carbon*, **49**, 2046–2052(2011).
108. W. S. Hummers and R. E. Offeman, "Preparation of graphitic oxide," *Journal of the American Chemical Society*, **80**, 1339(1958).
109. D. C. Marcano, D. V. Kosynkin, J. M. Berlin et al., "Improved synthesis of graphene oxide," *ACS Nano*, **4**, 4806–4814(2010).
110. X. Li, Y. Zhu, W. Cai, M. Borysiak, B. Han, D. Chen, R. D. Piner, L. Colombo, and R. S. Ruoff, "Transfer of Large-area graphene films for high-performance transparent conductive electrodes," *Nano. Lett.* **9**, 4359-4363(2009).
111. X. Liang, B. A. Sperling, I. Calizo, G. Cheng, et al, "Toward clean and crackless transfer of graphene," *Nano. Lett.* **5**, 9144-9153(2011).
112. V. Yu, Optics and chemical vapour deposition of graphene monolayers on various substrates, Ph.D. thesis, McGill University, 2010.
113. V. Yu and M. Hilke, "Large contrast enhancement of graphene monolayers by angle detection," *Applied Physics Letters*, **95**, 151904(2009).
114. Y. Y. Wang, Z. H. Ni, T. Yu et al., "Raman studies of monolayer graphene: the substrate effect," *Journal of Physical Chemistry C*, **112**, 10637–10640(2008).

115. P. Blake, E. W. Hill, A. H. Castro Neto et al., "Making graphene visible," *Applied Physics Letters*, **91**, 063124(2007).
116. H. Kim, M. Osofsky, S. M. Prokes, O. J. Glembocki, and A. Pique, "Optimization of Al-doped ZnO films for low loss plasmonic materials at telecommunication wavelengths," *Appl. Phys. Lett.* **102**, 171103 (2013).
117. G. V. Naik, J. Kim, and A. Boltasseva, "Oxides and nitrides as alternative plasmonic materials in the optical range" *Opt. Mater. Express*, **1**, 1090(2011).
118. J. M. Zhou, "Indium Tin Oxide (ITO) Deposition, Patterning, and Schottky Contact Fabrication," M. S. Thesis, 2005.
119. F. C. Lai, L. M. Lin, R. Q. Gai, Y. Z. Lin, and Z. G. Huang, "Determination of optical constants and thickness of In₂O₃: Sn films from transmittance data," *Thin Solid Films* **515**, 7387-7392(2007).
120. http://www.cnfusers.cornell.edu/cnf5_tool.taf?_function=detail&eq_id=156>itl e=THIN%20FILM%20DEPOSITION&area=THIN%20FILM%20DEPOSITION &cacName=PVD75%20Sputter%20Deposition&labUser=1& UserReference=8C 7122EA41988EBF56CB7462
121. P. Yeh, A. Yariv, and C. S. Hong, "Electromagnetic propagation in periodic stratified media. I. General theory," *J. Opt. Soc. Am.*, **67**, 423-438(1977).
122. K. S. Yee, "Numerical solution of initial boundary value problems involving Maxwell's equations," *IEEE Trans. Antennas Propag.* **14**, 302-307(1966).
123. A. Taflove and S. C. Hagness, *Computational Electromagnetics: The Finite-Difference Time-Domain Method*, Artech House, Norwood, 2005.
124. https://en.wikipedia.org/wiki/Finite-difference_time-domain_method
125. Y. Hao and R. Mittra, *FDTD Modeling of Metamaterials*. Artech House, 2009
126. W. Zhao, K. Shi, and Z. Lu, "Greatly enhanced ultrabroadband light absorption by monolayer graphene," *Opt. Lett.* **38**, 4342-4345(2013)
127. K. Shi, R. R. Haque, L.-F. Mao, and Z. Lu, "Graphene-sandwiched silicon structure for greatly enhanced unpolarized light absorption," *Opt. Commun.* **339**, 47-52(2015).

128. C. Lee, X. D. Wei, J. W. Kysar, and J. Hone, "Measurement of the elastic properties and intrinsic strength of monolayer graphene," *Science* **321**, 385-388(2008).
129. A. S. Mayorov, R. V. Gorbachev, S. V. Morozov, L. Britnell, R. Jalil, L. A. Pnomarenko, P. Blake, K. S. Novoselov, K. Watanabe, T. Taniguchi, and A. K. Geim, "Micrometer-Scale Ballistic Transport in Encapsulated Graphene at Room Temperature," *Nano Lett.* **11**, 2396-2399(2011).
130. K. I. Bolotin, K. J. Sikes, Z. Jiang, M. Klima, G. Fudenberg, J. Hone, P. Kim, H. L. Stormer, "Ultrahigh electron mobility in suspended graphene," *Solid State Commun.* **146**, 351-355(2008).
131. M. Y. Han, B. Özyilmaz, Y. B. Zhang, and P. Kim, "Energy band-gap engineering of graphene nanoribbons," *Phys. Rev. Lett.* **98**, 206805-206808(2007).
132. Z. Chen, Y. M. Lin, M. J. Rooks, and P. Avouris, "Graphene nano-ribbon electronics," *Physical E* **40**, 228-232(2007).
133. X. L. Li, X. R. Wang, L. Zhang, S. W. Lee, and H. J. Dai, "Chemically Derived, Ultrasoft Graphene Nanoribbon Semiconductors," *Science* **319**, 1229-1232(2008).
134. F. N. Xia, D. B. Farmer, Y. M. Lin, and P. Avouris, "Graphene Field-Effect Transistors with High On/Off Current Ratio and Large Transport Band Gap at Room Temperature," *Nano Lett.* **10**, 715-718(2010).
135. M. Kim, N. S. Safron, E. Han, M. S. Arnold, and P. Gopalan, "Fabrication and Characterization of Large-Area, Semiconducting Nano perforated Graphene Materials," *Nano Lett.* **10**, 1125-1131(2010).
136. X. G. Liang, Y. S. Jung, S. W. Wu, A. Ismach, D. L. Olynick, S. Cabrini, and J. Bokor, "Formation of bandgap and subbands in graphene nanomeshes with sub-10 nm ribbon width fabricated via nanoimprint lithography," *Nano Lett.* **10**, 2454-2460(2010).
137. J. W. Bai, X. Zhong, S. Jiang, Y. Huang, and X. F. Duan, "Graphene nanomesh," *Nature Nanotechnol.* **5**, 190-194(2010).

138. T. Ando, Y. S. Zheng, and H. Suzuura, "Dynamical Conductivity and Zero-Mode Anomaly in Honeycomb Lattices," *J. Phys. Soc. Jpn.* **71**, 1318-1324(2002).
139. Z. Fang, Z. Liu, Y. Wang, P. M. Ajayan, P. Nordlander, N. J. Halas, "A graphene-antenna sandwich photodetector," *Nano Lett.*, **12**, 3808(2012).
140. M. Furchi, A. Urich, A. Pospischil, G. Lilley, K. Unterrainer, H. Detz, P. Klang, A. M. Andrews, W. Schrenk, G. Strasser, and T. Mueller, "Microcavity-Integrated Graphene Photodetector," *Nano Lett.* **12**, 2773-2777(2012).
141. V. P. Gusynin, and S. G. Sharapov, "Transport of Dirac quasiparticles in graphene: Hall and optical conductivities," *Phys. Rev. B* **73**, 245411(2006).
142. S. Ryu, C. Mudry, A. Furusaki, and A. W. W. Ludwig, "Landauer conductance and twisted boundary conditions for Dirac fermions in two space dimensions," *Phys. Rev. B* **75**, 205344(2007).
143. T. Mueller, F. N. Xia, and P. Avouris, "Graphene photodetectors for high-speed optical communications," *Nat. Photonics* **4**, 297-301(2010).
144. T. J. Echtermeyer, L. Britnell, P. K. Jasnós, A. Lombardo, R. V. Gorbachev, A. N. Grigorenko, A. K. Geim, A. C. Ferrari, and K. S. Novoselov, "Strong plasmonic enhancement of photovoltage in graphene," *Nan. Commun.* **2**, 458(2011).
145. Y. Liu, R. Cheng, L. Liao, H. L. Zhou, J. W. Bai, G. Liu, L. X. Liu, Y. Huang, and X. F. Duan, "Plasmon resonance enhanced multicolour photodetection by graphene," *Nat. Commun.* **2**, 579(2011).
146. Y. Zhang, T. Liu, B. Meng, X. Li, G. Liang, X. Hu and Q. J. Wang, "Broadband high photoresponse from pure monolayer graphene photodetector," *Nat. Commun.* **4**, 2830 (2013).
147. X. Gan, K. F. Mak, Y. Gao, Y. You, F. Hatami, J. Hone, T. F. Heinz, and D. Englund, "Strong enhancement of light-matter interaction in graphene coupled to a photonic crystal nanocavity," *Nano Lett.* **12**, 5626-5631(2012).
148. J. M. Dawlaty, S. Shivaraman, J. Strait, P. George, M. Chandrashekhara, F. Rana, M. G. Spencer, D. Veksler, and Y. Chen, "Measurement of the optical absorption

- spectra of epitaxial graphene from terahertz to visible,” *Appl. Phys. Lett.* **93**, 131905 (2008).
149. C. H. Gan, “Analysis of surface plasmon excitation at terahertz frequencies with highly doped graphene sheets via attenuated total reflection,” *Appl. Phys. Lett.* **101**, 111609 (2012).
150. Q. Ye, J. Wang, Z. Liu, Z. Deng, X. T. Kong, F. Xing, X. Chen, W. Zhou, C. Zhang, and J.-G. Tian, “Polarization-dependent optical absorption of graphene under total internal reflection,” *Appl. Phys. Lett.* **102**, 021912 (2012)
151. G. Pirruccio, L. M. Moreno, G. Lozano, and J. G. Rivas, “Coherent and Broadband Enhanced Optical Absorption in Graphene,” *ACS Nano* **7**, 4810 (2013)
152. E. Kretschmann, and H. Raether, “Radiative Decay of Non Radiative Surface Plasmons Excited by Light,” *Z. Naturforsch* **23**, 2135-2136(1968)
153. <http://grapheneplatform.com/>
154. A. C. Ferrari, J. C. Meyer, V. Scardaci, C. Casiraghi, M. Lazzeri, F. Mauri, S. Piscanec, D. Jiang, K. S. Novoselov, S. Roth, and A. K. Geim, “Raman Spectrum of Graphene and Graphene layers,” *Phys. Rev. Lett.* **97**, 187401(2006).
155. K. Shi, W. Zhao, B. Zhao, and Z. Lu, “Novel approaches to enhance graphene absorption and electro-optic property,” *Proc. SPIE*, 89801C(2014)
156. D. Nilsson, N. Robinson, M. Berggren, and R. Forchheimer, “Electrochemical Logic Circuits,” *Adv. Mater.* **17**, 353-358(2005)
157. C. Lu, Q. Fu, S. Huang, and J. Liu, “Polymer Electrolyte-Gated Carbon Nanotube Field-Effect Transistor,” *Nano Lett.* **4**, 623-627(2004).
158. X. Gan, R. Shiue, Y. Gao, K. Mak, X. Yao, L. Li, A. Szep, D. Walker, J. Hone, T. F. Heinz, and D. Englund, “High-Contrast Electrooptic Modulation of a Photonic Crystal Nanocavity by Electrical Gating of Graphene,” *Nano Lett.* **13**, 691-696(2013).
159. L. S. Nefedov, C. A. Valaginnopoulos, and L. A. Melnikov, “Perfect absorption in graphene multilayers,” *Journal of Optics*, **15**, 114003(2013).

160. L. A. Falkovsky, and S. S. Pershoguba, "Optical far-infrared properties of a graphene monolayer and multilayer," *Phys. Rev. B*, **76**, 153410(2007).
161. A. B. Kuzmenko, E. van Heumen, F. Carbone, and D. van der Marel, "Universal Optical Conductance of Graphite," *Phys. Rev. Lett.*, **100**, 117401(2008).
162. G. W. Hanson, "Dyadic Green's functions and guided surface waves for a surface conductivity model of graphene," *J. Appl. Phys.*, **103**, 064302(2008).
163. C. Berger, Z. Song, X. Li, X. Wu, N. Brown, C. Naud, D. Mayou, T. Li, J. Hass, A. L. Marchenkov, E. H. Conrad, P. N. First, and W. A. de Heer, "Electronic Confinement and Coherence in Patterned Epitaxial Graphene," *Science*, **312**, 1191(2006).
164. M. L. Sadowski, G. Martinez, and M. Potemski, "Landau Level Spectroscopy of Ultrathin Graphite Layers," *Phys. Rev. Lett.*, **97**, 266405(2006).
165. X. Wang, L. Zhi, N. Tsao, Ž. Tomović, J. Li, and K. Müllen, "Transparent Carbon Films as Electrodes in Organic Solar Cells," *Angew. Chem.* **47**, 2990-2992(2008).
166. L. G. De Arco, Y. Zhang, C. W. Schlenker, K. Ryu, M. E. Thompson, and C. Zhou, "Continuous, Highly Flexible, and Transparent Graphene Film by Chemical Vapor Deposition for Organic Photovoltaics," *ACS nano*, **4**, 2865-2873(2010).
167. K. J. Tielrooij, J. C. W. Song, S. A. Jensen, A. Centeno, A. Pesquera, A. Z. Elorza, M. Bonn, L.S. Levitov, and F. H. L. Koppens, "Photoexcitation cascade and multiple hot-carrier generation in graphene," *Nat. Phys.*, **9**, 248-252(2013).
168. T. Winzer, A. Knorr, and E. Malic, "Carrier multiplication in graphene," *Nano Lett.*, **10**, 4839-4843(2010).
169. V. I. Klimov, and D. W. McBranch, "Femtosecond 1P-to-1S Electron Relaxation in Strongly Confined Semiconductor Nanocrystals," *Phys. Rev. Lett.* **80**, 402(1998).
170. M. Silveirinha, and N. Engheta, "Tunneling of Electromagnetic Energy through Subwavelength Channels and Bends using ϵ -Near-Zero Materials," *Phys. Rev. Lett.*, **97**, 157403(2006).

171. R. Liu, Q. Cheng, T. Hand, J. J. Mock, T. J. Cui, S. A. Cummer, and D. R. Smith, "Experimental Demonstration of Electromagnetic Tunneling Through an Epsilon-Near-Zero Metamaterial at Microwave Frequencies," *Phys. Rev. Lett.*, **100**, 023903(2008).
172. R. W. Ziolkowski, "Propagation in and scattering from a matched metamaterial having a zero index of refraction," *Phys. Rev. E*, **70**, 046608(2004).
173. M. Silveirinha, and N. Engheta, "Design of matched zero-index metamaterials using nonmagnetic inclusions in epsilon-near-zero media," *Phys. Rev. B*, **75**, 075119(2007).
174. A. Alù, M. Silveirinha, A. Salandrino, and N. Engheta, "Epsilon-Near-Zero (ENZ) Metamaterials and Electromagnetic Sources: Tailoring the Radiation Phase Pattern," *Phys. Rev. B*, **75**, 155410(2007).
175. S. Enoch, G. Tayeb, P. Sabouroux, N. Guerin, and P. Vincent, "A Metamaterial for Directive Emission," *Phys. Rev. Lett.*, **89**, 213902(2002).
176. P. Drude, "Zur Elektronentheorie der metalle," *Annalen der Physik* **306**, 566(1900).
177. P. Drude, "Zur Elektronentheorie der metalle; II. Teil. Galvanomagnetische und thermomagnetische Effecte," *Annalen der Physik* **308**, 369(1900).
178. M. Fox, "Free electrons," in *Optical Properties of Solids*, Oxford University Press, pp. 154-157, 2001.
179. R. Yang, Z. Lu, "Subwavelength plasmonic waveguides and plasmonic materials," *Internat. J. Opt.*, **2012**, 258013(2012).
180. L. V. Alekseyev, E. E. Narimanov, T. Tumkur, H. Li, Yu. A. Barnakov and M. A. Noginov, "Uniaxial epsilon-near-zero metamaterial for angular filtering and polarization control," *Appl. Phys. Lett.*, **97**, 131107(2010).
181. V. Mocella, P. Dardano, I. Rendina and S. Cabrini, "An extraordinary directive radiation based on optical antimatter at near infrared," *Opt. Express*, **18**, 25068-25074(2011).
182. A. Ciattoni, R. Marinelli, C. Rizza and E. Palange, " ϵ -Near-zero materials in the near-infrared," *Appl. Phys. B* **110**, 23-26(2012).

183. K. Shi, and Z. Lu, "Optical modulators and beam steering based on electrically tunable plasmonic material," *J. Nanophoton.* **9**, 093793(2015).
184. V. R. Almeida, Q. Xu, C. A. Barrios and M. Lipson, "Guiding and Confining Light in Void Nanostructure," *Opt. Lett.*, **29**, 1209-1211(2004).
185. Q. Xu, V. R. Almeida, and M. Lipson, "Experimental demonstration of guiding and confining light in nanometer-size low-refractive-index material," *Opt. Lett.*, **29**, 1626-1628(2004).
186. K. Shi, W. Zhao, and Z. Lu, "Epsilon-near-zero-slot waveguides and their applications in ultrafast laser beam steering," *Proc. SPIE*, 89800L(2014).
187. Z. Lu, W. Zhao and K. Shi, "Ultracompact electro-absorption modulators based on tunable epsilon-near-zero-slot waveguides," *IEEE J. PHOT.*, **4**, 735-740(2012).
188. H. D. Tholl, "Novel Laser Beam Steering Techniques," *Proc. SPIE*, 639708(2006).
189. J. Bourderionnet, M. Rungenhagen, D. Dolfi and H. D. Tholl, "Continuous laser beam steering with micro-optical arrays-Experimental results," *Proc. SPIE*, 71130Z(2008).
190. J. Kim, C. Oh, M. J. Escuti, L. Hosting, and S. Serati, "Wide-angle, nonmechanical beam steering using thin liquid crystal polarization gratings," *Proc. SPIE*, 709302(2008).
191. K. Shi, R. R. Haque, B. Zhao, R. Zhao, and Z. Lu, "Broadband electro-optical modulator based on transparent conducting oxide," *Opt. Lett.* **39**, 4978-4981(2014).
192. K. Shi, and Z. Lu, "Field-effect optical modulation based on epsilon-near-zero conductive oxide," *Opt. Commun.* **370**, 22-28 (2016).
193. Z. Lu, P. Yin, and K. Shi, "Nanoscale field effect optical modulators based on depletion of epsilon-near-zero films," arXiv: 1512.08232(2015).
194. A. Melikyan, N. Lindenmann, S. Walheim, P. M. Leufke, S. Ulrich, J. Ye, P. Vincze, H. Hahn, T. Schimmel, C. Koos, W. Freude, and J. Leuthold, "Surface plasmon polariton absorption modulator," *Opt. Express* **19**, 8855–8869 (2011).

195. V. E. Babicheva and A. V. Lavrinenko, "Plasmonic modulator optimized by patterning of active layer and tuning permittivity," *Opt. Commun.* **285**, 5500–5507 (2012).
196. A. V. Krasavin and A. V. Zayats, "Photonic signal processing on electronic scales: Electro-optical field-effect nanoplasmonic modulator," *Phys. Rev. Lett.* **109**, 053901 (2012).
197. A. P. Vasudev, J. Kang, J. Park, X. Liu, and M. L. Brongersma, "Electro-optical modulation of a silicon waveguide with an "epsilon-near-zero" material," *Opt. Express* **21**, 123–129 (2013).
198. C. Huang, R. J. Lamond, S. K. Pickus, Z. R. Li, and V. J. Sorger, "A sub- λ -size modulator beyond the efficiency-loss limit," *IEEE Photonics J.* **5**, 2202411 (2013).
199. H. W. Lee, G. Papadakis, S. P. Burgos, K. Chandler, A. Kriesch, R. Pala, U. Peschel, and H. A. Atwater, "Nanoscale Conducting Oxide PlasMOStor," *Nano Lett.* **14**, 6463–6468 (2014).
200. Z. Lu, K. Shi, and P. Yin, "Photonic MOS Based on Optical Property Inversion," *MRS Advances*, Available on CJO 2015 doi:10.1557/adv.2015.5.
201. C. Hoessbacher, Y. Fedoryshyn, A. Emboras, A. Melikyan, M. Kohl, D. Hillerkuss, C. Hafner, and J. Leuthold, "The plasmonic memristor: a latching optical switch," *Optica*, **1**, 198-202(2014).
202. J. S. Schildkraut, "Long-range surface plasmon electrooptic modulator," *Appl. Opt.* **27**, 4587–4590 (1988).
203. T. Nikolajsen, K. Leosson, and S. I. Bozhevolnyi, "Surface plasmon polariton based modulators and switches operating at telecom wavelengths," *Appl. Phys. Lett.* **85**, 5833 (2004).
204. W. Cai, J. S. White, and M. L. Brongersma, "Compact, high-speed and power-efficient electrooptic plasmonic modulators," *Nano Lett.* **9**, 4403–4411 (2009).
205. S. Randhawa, S. Lachèze, J. Renger, A. Bouhelier, R. E. de Lamaestre, A. Dereux, and R. Quidant, "Performance of electro-optical plasmonic ring resonators at telecom wavelengths," *Opt. Express* **20**, 2354–2362(2012).

206. A. V. Krasavin and A. V. Zayats, "Photonic signal processing on electronic scales: Electro-optical field-effect nanoplasmonic modulator," *Phys. Rev. Lett.* **109**, 053901 (2012).
207. R. Hunsperger, *Integrated Optics: Theory and Technology*, Chapter 9, Springer Science & Business Media, 2009.
208. M. Liu, X. Yin, and X. Zhang, "Double-layer graphene optical modulator," *Nano Lett.* **12**, 1482–1485 (2012).
209. J. Baek, J.-B. You, and K. Yu, "Free-carrier electro-refraction modulation based on a silicon slot waveguide with ITO," *Opt. Express* **23**, 15863–15876 (2015).
210. M. Vehkamäki, T. Hatanpää, T. Hanninen, M. Ritala and M. Leskela, "Growth of SrTiO₃ and BaTiO₃ Thin Films by Atomic Layer Deposition," *Electrochemical and Solid State Lett.* **2**, 504-506 (1999).
211. C.-J. Peng, H. Hu, and S. B. Krupanidhi, "Electrical properties of strontium titanate thin films by multi-ion-beam reactive sputtering technique," *Appl. Phys. Lett.* **63**, 1038 (1993).
212. H. Zhao, Y. Wang, A. Capretti, L. D. Negro, and J. Klamkin, "Broadband electroabsorption modulators design based on epsilon-near-zero Indium Tin Oxide," *IEEE J. Sel. Topics Quantum Electron.* **20**, 192(2015).
213. X. Wang, L. Zhi, N. Tsao, Z. Tomovic, J. Li, and K. Mullen, "Transparent carbon films as electrodes in organic solar cells," *Angew. Chem.* **47**, 2990–2992 (2008).
214. J. Wu, H. A. Becerril, Z. Bao, Z. Liu, Y. Chen, and P. Peumans, "Organic solar cells with solution-processed graphene transparent electrodes," *Appl. Phys. Lett.* **92**, 263302 (2008).
215. L. G. D. Arco, Y. Zhang, C. W. Schlenker, K. Ryu, M. E. Thompson, and C. Zhou, "Continuous, highly flexible, and transparent graphene films by chemical vapor deposition for organic photovoltaics," *ACS Nano* **4**, 2865–2873 (2010).
216. Y. U. Jung, S. Na, H. Kim, and S. Jun Kang, "Organic photovoltaic devices with low resistance multilayer graphene transparent electrodes," *Journal of Vacuum Science & Technology A: Vacuum, Surfaces, and Films*, **30**, 050604(2012).

217. J. Wang, Y. Wang, D. He et al., "Polymer bulk heterojunction photovoltaic devices based on complex donors and solution processable functionalized graphene oxide," *Solar Energy Materials and Solar Cells*, **96**, 58–65(2012).
218. V. Yong and J. M. Tour, "Theoretical efficiency of nanostructured graphene-based photovoltaics," *Small*, **6**, 313–318(2010).
219. A. M. Ramirez, E. J. L. Naranjo, W. Soboyejo, Y. M. Vong, and B. Vilquin, "A review on the efficiency of graphene-based BHJ organic solar cells," *J. Nanomaterials*, **2015**, 406597(2015).
220. N. Walsh, "Passivation of amorphous Indium-Gallium-Zinc Oxide (IGZO) thin-film transistors," (2014). Thesis, Rochester Institute of Technology.